

Prognostication of disorders of consciousness using brain functional networks and clinical features

Ming Song^{1,2*}, Yi Yang^{3*}, Jianghong He³, Zhengyi Yang^{1,2}, Shan Yu^{1,2}, Qiuyou Xie⁴, Xiaoyu Xia³, Yuanyuan Dang³, Qiang Zhang³, Xinhuai Wu⁵, Yue Cui^{1,2}, Bing Hou^{1,2}, Ronghao Yu⁴, Ruxiang Xu³, Tianzi Jiang^{1,2,6,7,8}

¹National Laboratory of Pattern Recognition, Institute of Automation, The Chinese Academy of Sciences, Beijing 100190, China

²Brainnetome Center, Institute of Automation, The Chinese Academy of Sciences, Beijing 100190, China

³Department of Neurosurgery, PLA Army General Hospital, Beijing 100700, China

⁴Centre for Hyperbaric Oxygen and Neurorehabilitation, Guangzhou General Hospital of Guangzhou Military Command, Guangzhou 510010, China

⁵Department of Radiology, PLA Army General Hospital, Beijing 100700, China

⁶CAS Center for Excellence in Brain Science and Intelligence Technology, Chinese Academy of Sciences, Beijing 100190, China

⁷Key Laboratory for Neuroinformation of the Ministry of Education, School of Life Science and Technology, University of Electronic Science and Technology of China, Chengdu 625014, China

⁸The Queensland Brain Institute, University of Queensland, Brisbane, QLD 4072, Australia

*These authors contributed equally to this work.

To whom correspondence should be addressed:

Tianzi Jiang

National Laboratory of Pattern Recognition

Institute of Automation

Chinese Academy of Sciences

Beijing 100190, China

Phone: +86 10 8254 4778

Fax: +86 10 8254 4778

Email: jiangtz@nlpr.ia.ac.cn

And

Ruxiang Xu

Department of Neurosurgery

PLA Army General Hospital

Beijing 100700, China

Phone: +86 10 6403 0762

Fax: +86 10 6403 0762

E-mail: zjxuruxiang@163.com

Running title:

Multivariable prognostic model for DOC

Abstract

Disorders of consciousness are a heterogeneous mixture of different diseases or injuries. Although some indicators and models have been proposed for prognostication, any single method when used alone carries a high risk of false prediction. This study aimed to investigate whether a multivariable paradigm that combined resting state functional magnetic resonance imaging and clinical characteristics could predict the outcome at an individual level and identify the patient who would later recover consciousness. Three datasets comprising a total of 112 patients with disorders of consciousness from two medical centers in China were involved in the study. Of the three datasets, one was used as the training dataset to establish a prediction model, and the other two were used only for validation. Combining the features extracted from the resting state functional magnetic resonance imaging and three clinical characteristics, i.e. etiology, incidence age and duration of unconsciousness, we built a regression model to predict the prognosis of the patients at the individual level. Each patient was then classified based on whether or not they were expected to recover consciousness. The classification accuracy was assessed by comparing these results with the actual outcome during at least 12 months follow-up. For the training dataset, the classification accuracy was up to 92% (sensitivity: 85%; specificity: 94%). For the two testing datasets, the classification accuracy was up to 88% (sensitivity: 83%; specificity: 92%) and 88% (sensitivity: 100%; specificity: 83%), respectively. Notably, in the testing dataset, our method could accurately identify the patients who were initially diagnosed as being in a vegetative

state/unresponsive wakefulness syndrome but subsequently recovered consciousness. Furthermore, by analyzing the weights of the predictors in the regression model, we found that the presented model could not only verify the value of these brain imaging and clinical features in prognostication, but also provide a window to assess the relative significance of various predictors, including brain networks, functional connectivities and clinical characteristics. These advantages could help to predict the outcome of patients with disorders of consciousness and provide new insights into brain function patterns of unconsciousness.

Keywords: disorders of consciousness; prognosis; resting state fMRI; functional connectivity; brain network

Abbreviations: CRS-R = Coma Recovery Scale-Revised; DOC = disorders of consciousness; GOS = Glasgow Outcome Scale; MCS = minimally conscious state; PLSR = partial least square regression; UWS = unresponsive wakefulness syndrome; VS = vegetative state

Introduction

Severe brain injury can lead to disorders of consciousness (DOC). Prognostication is a fundamental concern for DOC patients, as medical treatment and rehabilitation therapy depend on this information (Bernat, 2006). To date, the prognostication for a DOC patient is based on physician observation of the patient's behavior over a sufficient period of time to discover whether there is any evidence of awareness. On the one hand, a patient's motor impairment, sensory deficit, cognitive damage, fluctuation of vigilance and medical complications could give rise to misjudgments; on the other hand, for the assessor, a lack of knowledge regarding DOC, poor training and non-use of adequate behavioral scales are additional elements that contribute to a high possibility of mistakes. Consequently, careful and repeated behavioral assessments are considered to be particularly important for a precise diagnostic and prognostic judgment (Wannez *et al.*, 2017). However, behavioral assessments are inevitably subjective and vulnerable to a variety of personal interferences (Giacino *et al.*, 2009). Physicians and scientists have therefore been seeking accurate and objective markers for diagnosis and prognosis (Demertzi *et al.*, 2017; Noirhomme *et al.*, 2017).

Several pioneering studies suggested that the etiology, incidence age and duration of DOC were important indicators for prognosis (The Multi-Society Task Force on PVS, 1994). Specifically, patients with non-traumatic brain injury were expected to have a worse functional recovery than traumatic brain injury patients, and young patients were considered more likely to have a favorable outcome than older ones. During the past decades, some pilot prognostic models have also been explored based

on features of neurological examination (Zandbergen *et al.*, 1998; Booth *et al.*, 2004; Dolce *et al.*, 2008), abnormalities detected with EEG and evoked potentials (Steppacher *et al.*, 2013; Kang *et al.*, 2014; Hofmeijer and van Putten, 2016; Chennu *et al.*, 2017), anatomical and functional changes identified with brain CT, PET and MRI (Maas *et al.*, 2007; Sidaros *et al.*, 2008; Galanaud *et al.*, 2012; Luyt *et al.*, 2012; Stender *et al.*, 2014; Wu *et al.*, 2015), and physiological and biochemical disturbances at both the brain and body levels (Kaneko *et al.*, 2009; Rundgren *et al.*, 2009). However, despite many efforts, identifying efficient biomarkers for the early prediction of outcome is still challenging and requires more researches. One of the reasons for this is that the DOC could have many different causes and be associated with several neuropathological processes and different severities, such that any method when used alone carries the risk of false prediction (Bernat, 2016; Rossetti *et al.*, 2016).

Recently, resting state functional MRI (fMRI) has been widely used to investigate the brain functions of DOC patients. Research suggests that these patients demonstrate multiple changes in brain functional networks, including the default mode (Vanhaudenhuyse *et al.*, 2010; Silva *et al.*, 2015), executive control (Demertzi *et al.*, 2014b; Wu *et al.*, 2015), salience (Qin *et al.*, 2015; Fischer *et al.*, 2016), sensorimotor (Yao *et al.*, 2015), auditory (Demertzi *et al.*, 2015), visual (Demertzi *et al.*, 2014a) and subcortical networks (He *et al.*, 2015). The within-network and between-network functional connectivity appeared to be useful indicators of functional brain damage and the likelihood of consciousness recovery (Silva *et al.*, 2015; Di Perri *et al.*, 2016).

Taken together, these studies suggested that the brain networks and functional connectivity detected with resting state fMRI could be valuable biomarkers to trace the level of consciousness and predict the possibility of recovery.

With advances in medicine, prognostication of a DOC patient has moved towards a multivariable paradigm that combines clinical examination with the application of novel technologies (Gosseries *et al.*, 2014). Multivariable assessment has the potential to improve prediction accuracy. More importantly, it can provide reassurances about the importance of each predictor for prognostication by offering concordant evidence (Stevens and Sutter, 2013; Rossetti *et al.*, 2016). More than twenty years ago, the Multi-Society Task Force on PVS suggested that the etiology, incidence age and duration of DOC could help to predict the outcome (The Multi-Society Task Force on PVS, 1994), and numerous studies have subsequently validated the clinical utility of these features (Jennett, 2005; Bruno *et al.*, 2012; Estraneo *et al.*, 2013; Celesia, 2016). Therefore, it is possible that a multivariable model that combines these clinical characteristics and resting state fMRI could improve prognostic predictions at an individual level and lead to the early identification of patients who could recover consciousness.

The present work had two major objectives. The first aim was to develop an approach to predict the prognosis of an individual DOC patient using clinical characteristics and resting state fMRI. The second aim, building on the first, was to further explore different prognostic effects of these clinical and brain imaging features.

Materials and methods

The study paradigm is illustrated in Fig. 1. Resting state fMRI and clinical data from DOC patients were collected at the so-called $T0$ time point when the patients' vital signs and conscious level had stabilized and the diagnosis was made. Outcomes were assessed at least 12 months after this $T0$ time point; this is referred to as the $T1$ time point. The principal scales included the Coma Recovery Scale Revised (CRS-R) and the Glasgow Outcome Scale (GOS). Instead of predicting diagnosis, this study used the outcome as a target for regression and classification. Using the resting state fMRI and clinical data at the $T0$ time point, a regression model was first developed to fit each patient's CRS-R score at the $T1$ time point, after which the optimal cut-off value for classifying individual patients based on consciousness recovery was calculated. In this way, we set up the prognostic regression and classification model. The two testing datasets were then used to validate the model.

Subjects

This study involved three datasets. The datasets referred to as "Beijing 750" and "Beijing HDxt" were both collected in the PLA Army General Hospital in Beijing, and the same medical group diagnosed and managed the patients. However, the MRI scanners and imaging acquiring protocols were different; the "Beijing HDxt" cohort was scanned with a GE signa HDxt 3.0T scanner between May 2012 and December 2013, whereas the "Beijing 750" cohort was scanned with a GE Discovery MR750 3.0T scanner between January 2014 and May 2016. The dataset referred to as "Guangzhou HDxt" was collected from the Guangzhou General Hospital of

Guangzhou Military Command in Guangzhou, and the MRI data was obtained with a GE signa HDxt 3.0T scanner between April 2011 and December 2014. The inclusion criteria was that the patients should be at least 1 month after the acute brain insult so that they met the DOC diagnosis. Patients were excluded when there was an unstable level of consciousness (continuous improvement or decline within the two weeks before the T0 time point), uncertain clinical diagnosis (ambiguity or disagreement between examiners), contraindication for MRI or large focal brain damage (>30% of total brain volume). Normal controls were free of psychiatric or neurological history.

As the dataset "Beijing 750" involved more patients than the other two datasets, it was used as the training dataset for model development and internal validation, whereas the "Beijing HDxt" and "Guangzhou HDxt" datasets were only used for external validation. The study was approved by the Ethics Committee of the PLA Army General Hospital and the Ethics Committee of the Guangzhou General Hospital of Guangzhou Military Command. Informed consent to participate in the study was obtained from the legal surrogates of the patients and from the normal controls.

Clinical measurements

Diagnosis and consciousness assessments

The diagnosis was made by experienced physicians according to the CRS-R scale (The Multi-Society Task Force on PVS, 1994; Bernat, 2006; Magrassi *et al.*, 2016). The patients underwent the evaluations at least twice weekly within the two weeks before the T0 time point. The highest CRS-R score was considered as the diagnosis. The CRS-R includes six subscales that address auditory, visual, motor, oromotor,

communication, and arousal functions, which are summed to yield a total score ranging from 0 to 23.

Outcome assessments

All patients were followed up at least 12 months after the *T0* time point, according to the protocols for DOC described in a number of previous studies (Galanaud et al., 2012; Luyt et al., 2012; Stender et al., 2014; Pignat et al., 2016). Basically, follow-up interviews were performed in four ways, including outpatient visit, assessments by local physicians, home visit, and telephone/video review. Whenever possible signs of responsiveness were detected or reported, the patient was evaluated either at the unit or at home by the hospital staff. In cases where no change was signaled, patients were examined twice by one hospital physician via telephone/video reviews at the end of the follow-up process. The patients who died during the follow-up process were excluded. The principal outcome measure was the GOS, which provides a measurement of outcome ranging from 1 to 5 (1, dead; 2, vegetative state/minimally conscious state; 3, able to follow commands/unable to live independently; 4, able to live independently/unable to return to work or school; 5, good recovery/able to return to work or school).

The GOS score was available for each patient in the three datasets. Because this study aimed to predict recovery of consciousness, the outcomes were ultimately stratified into two groups, “consciousness non-recovery” ($GOS \leq 2$) or “consciousness recovery” ($GOS > 2$). The training dataset "Beijing 750" and the testing dataset "Beijing Hdxt" also included the CRS-R scores at the *T1* time point for each patient.

The testing dataset "Guangzhou Hdxt" did not assess the CRS-R scores at the *T1* time point.

MRI acquisition

All of the participants in the three datasets were scanned with resting state fMRI and T1-weighted 3D high-resolution imaging. During the MRI scanning, the participants did not take any sedative or anesthetic drugs. The resting state fMRI scan was obtained using a T2*-weighted gradient echo sequence, and a high-resolution T1-weighted anatomical scan was obtained to check whether the patients had large brain distortion or focal brain damage. For the training dataset "Beijing 750", the resting state fMRI acquisition parameters included TR/TE=2000/30ms, flip angle=90°, axial 39 slices, thickness=4mm, no gap, FOV=240×240mm, matrix=64×64, and 210 volumes (i.e., 7 minutes). For the testing dataset "Beijing HDxt", the resting state fMRI acquisition parameters were as follows: axial 33 slices, TR/TE=2000/30ms, flip angle=90°, thickness=4mm, no gap, FOV=220×220mm, matrix=64×64, and 240 volumes (i.e., 8 minutes). For the testing dataset "Guangzhou HDxt", the resting state fMRI acquisition parameters included axial 35 slices, TR/TE=2000/30ms, flip angle=90°, thickness=4mm, no gap, FOV=240×240mm, matrix=64×64, and 240 volumes (i.e., 8 minutes).

Data analysis

The data analysis pipeline is illustrated in Fig. 2.

Imaging preprocessing

Preprocessing and connectivity calculation were performed in the same way for the training dataset and the two testing datasets. All resting state fMRI scans were preprocessed using SPM8 (<http://www.fil.ion.ucl.ac.uk/spm>) and in-house Matlab codes. Specifically, the first five volumes of each subject were discarded. The remaining resting state fMRI volumes were corrected for slice timing differences and realigned to the first volume to correct for inter-scan movements. Subsequently, the functional images were spatially smoothed with a Gaussian kernel of $6 \times 6 \times 6$ mm full-width at half maximum. Linear regression was then used to remove the influence of head motion, whole brain signals and linear trends. The variables regressed out included 12 motion parameters (roll, pitch, yaw, translation in three dimensions and their first derivatives), the average series of the signals within the brain, and the regressors for linear trends.

Motion artifact is increasingly recognized as an important potential confound in resting state fMRI studies. Any particular motion may produce a wide variety of signal changes in the fMRI data, and thus introduce complicated shifts in functional connectivity analysis. This problem was particularly serious for the DOC patients, as they were unlikely to follow the experimental instructions and control their head motion. To balance the demands of noise reduction and data preservation, we censored volumes that preceded or followed any movement (framewise displacement, FD) greater than 1.5 mm. The FD is a summarization of the absolute values of the derivatives of the translational and rotational realignment estimates (after converting

the rotational estimates to displacement at 50 mm radius) (Power *et al.*, 2015). The head motion measures were achieved in the preprocessing step of realignment using SPM. To obtain reliable Pearson's correlations for functional connectivity, the patients with less than 50 volumes worth of remaining data were excluded. More information about the analysis and validation of controls for motion-related artifacts are provided in supplementary material 4.

Finally, to reduce low-frequency drift and high-frequency noise, band-pass filtering (0.01-0.08 Hz) was performed only on volumes that survived motion censoring.

Definition of networks and regions of interest

As noted in the introduction, multiple networks were disrupted in the DOC patients. Among these impaired networks, six brain networks, including the default mode, executive control, salience, sensorimotor, auditory, and visual networks, show system-level damages and significant correlations with behavioral assessments (Demertzi *et al.*, 2014b; Demertzi *et al.*, 2015). We therefore defined a total of 22 regions of interest (ROIs) to probe these six brain networks. The names and Montreal Neurological Institute (MNI) coordinates of these ROIs are listed in supplementary material 2.

The connection templates of the six brain networks were firstly investigated within the normal control group. In addition to the above-mentioned preprocessing stages, the resting state fMRIs of the normal controls in the training dataset were transformed into MNI standard space. For each of the six networks, time series from

the voxels contained in the various ROIs were extracted and averaged together. The averaged time series were then used to estimate whole-brain correlation r maps that were subsequently converted to normally distributed Fisher's z -transformed correlation maps. Group functional connectivity maps for each of the six networks were then created with a one-sample t test. Notably, the T map included both positive and negative values. We used the six T maps as the brain connection templates of the corresponding brain networks (see supplementary material 3 for details).

The conventional fMRI preprocess normalizes individual fMRI images into a standard space defined by a specific template image. Our goal was to extend this conventional approach to generate a functional connectivity image for each patient in his/her own imaging space. During the preprocessing of each patient's fMRI scans, the 22 ROIs and six brain connection templates were therefore spatially warped to individual fMRI space and resampled to the voxel size of the individual fMRI image. We also developed tools to visually check the registration for each subject, some examples of which are provided in supplementary material 5.

Calculation of imaging features

We designed two types of imaging features from the resting state fMRI, one being functional connectivity between each pair of 22 ROIs, and the other being the spatial resemblance between the functional connection patterns of each ROI and the brain connection templates across the whole brain. The functional connectivity was based on the Pearson's correlation coefficients, while the spatial resemblance was conceptually similar to the template-matching procedure (Greicius *et al.*, 2004; Seeley

et al., 2007; Vanhaudenhuyse *et al.*, 2010). In fact, the idea of template matching is that the more spatial consistency that exists between the template of a brain network and a specific connectivity map (for example, a component in an independent component analysis), the stronger the possibility that the connectivity map belongs to this brain network. Here, for a specific ROI of an individual DOC patient, we computed the whole brain functional connectivity map of this ROI using the Pearson's correlation coefficients that were subsequently converted to normally distributed Fisher's z transformed correlation maps. We then calculated the spatial resemblance between the functional connectivity map and the corresponding brain connection template wrapped to individual fMRI space. We defined the spatial resemblance as the connection feature of the ROI. Our assumption was that the more spatially consistent the connectivity map of the ROI in a DOC patient and the brain connection template, the more intact the corresponding brain function of the ROI in this individual.

Thus, for each participant in this study, there were 231 ($22 \times 21/2$) functional connectivity features and 22 brain area connection features.

Imaging feature selection

Feature selection techniques have been widely adopted in brain analysis studies, in order to produce a small number of features for efficient classification or regression, and to reduce overfitting and increase the generalization performance of the model (Fan *et al.*, 2007; Dosenbach *et al.*, 2010; Drysdale *et al.*, 2016). Feature ranking and feature subset selection are two typical feature selection methods (Guyon and Elisseeff, 2003). Feature subset selection methods are generally time consuming, and

even inapplicable when the number of features is extremely large, whereas ranking-based feature selection methods are subject to local optima. Therefore, these two feature selection methods are usually used jointly. Here, we first used a correlation-based feature selection to select an initial set of features, and then adopted a feature subset selection method for further selection.

As a univariate method, correlation-based feature selection is simple to run and understand, and measures the linear correlation between each feature and the response variable. Here, the image features (i.e., functional connectivity features and brain area connection features) which significantly correlated to the CRS-R scores at the *T1* time point across the DOC patients in the training dataset were retained for further analysis.

The competitive adaptive reweighted sampling coupled with partial least squares regression (CARS-PLSR, <http://libpls.net/>) was then used for further feature subset selection (Li *et al.*, 2009; Li *et al.*, 2014). Briefly, CARS-PLSR is a sampling-based feature selection method that picks out the key informative variables by optimizing the model's performance. As it provides the influence of each variable without considering the influence of the rest of the variables, CARS-PLSR is efficient and fast for feature selection (Mehmood *et al.*, 2012), and has therefore been used to explore possible biomarkers in medicine (Tan *et al.*, 2010) and for wavelength selection in chemistry (Fan *et al.*, 2011). Using the CARS-PLSR, we selected a subset of key informative imaging features.

Notably, both the correlation-based and CARS-PLSR feature selection methods

filtered the features from the original feature set without any transformations. This made the prognostic regression model easier to interpret, as the imaging predictors were associated with either brain regions or functional connectivity.

Modeling and internal validation

The PLSR is well able to handle multicollinearity among the predictors (Wold et al., 2001; Krishnan et al., 2011). It was therefore used to generate the prognostic regression model. Given that clinical characteristics, including the etiology, incidence age and duration of DOC, have been verified as useful prognostic indicators, we designed the selected imaging features and the three clinical characteristics at the *T0* time point together as independent co-variates and the CRS-R scores at the *T1* time point as the dependent variable. Among the three clinical characteristics, the incidence age and duration of DOC were quantitative variables, whereas the etiology was a qualitative variable. In accordance with a previous study (Estraneo *et al.*, 2010), we categorized the etiology into three types, including traumatic brain injury, stroke and anoxic brain injury. Thus, the two dummy variables for etiology were designed and included in the model. Prior to model training, all involved predictors were normalized. The prognostic regression model therefore took the imaging and clinical features as input and returned a predicted score as output. To evaluate the regression model, the coefficient of determination R^2 between the predicted scores and the CRS-R scores at the *T1* time point was calculated, and the Bland-Altman plot was used to measure the agreement between them.

The prognostic regression model was also internally validated using bootstrap

(Steyerberg, 2008). Specifically, 1,000 bootstrap samples were drawn with replacement from the original training dataset such that each bootstrap sample had a number of observations equal to that of the training dataset. In each bootstrap sample, CARS-PLSR was used to reselect the feature subset, and the PLSR was used to regenerate a prognostic model. Next, the coefficient of determination R^2 on the bootstrap sample and the original training sample was calculated, and an estimation of the optimism was obtained. Finally, the optimism-corrected coefficient of determination R^2 was calculated.

Next, receiver operating characteristic (ROC) curves were plotted for the predicted scores. Here, the optimal cut-off value for classifying an individual patient as having recovered consciousness or not was the point with the maximal sum of true positive and false negative rates on the ROC curve. Individual patients were classified as exhibiting recovery of consciousness if their predicted scores were higher than or equal to the cut-off value.

External validation of model

External validation is essential to support the general applicability of a prediction model. We ensured external validity by testing the model in two testing datasets, neither of which included samples that were considered during the development procedure of the model. First, using the produced prognostic regression model, we calculated one predicted score for each patient in the two testing datasets. As the "Beijing HDxt" dataset assessed the patients' CRS-R scores at the *T1* time point, we calculated the coefficient of determination R^2 between the predicted scores and the

patients' CRS-R scores at this time point. The Bland-Altman plot was also determined. Finally, the patients in the two testing datasets were assessed as achieving consciousness recovery or not based on the cut-off threshold obtained using the training dataset. The performance of the classification, including the accuracy, sensitivity and specificity, was determined.

RESULTS

Subjects

One hundred and sixty DOC patients were initially enrolled in this study. Eleven patients were excluded due to large local brain lesions or movement artifacts. Nine patients died during the period of the follow-up, 16 patients were lost to follow-up, and no definite outcome information was collected for 12 patients at the endpoint of the follow-up. Thus, according to the inclusion and exclusion criteria and the follow-up results, the training dataset "Beijing 750" included 46 vegetative state/unresponsive wakefulness syndrome (VS/UWS) patients and 17 minimally conscious state (MCS) patients. The testing dataset "Beijing HDxt" contained 20 VS/UWS patients and five MCS patients, and the other testing dataset "Guangzhou HDxt" contained 16 VS/UWS patients and eight MCS patients. The average (maximum, minimum) number of behavioral CRS-R assessments for a patient before MRI scanning was 4.4 (7,4) in the "Beijing 750" dataset and 4.6 (7,4) in the "Beijing HDxt" dataset, respectively.

The demographic and clinical characteristics of the patients are summarized in Table 1, with additional details provided in supplementary material 1. The "Beijing

750" dataset also included 30 normal controls, and the "Beijing HDxt" dataset included 10 normal controls.

Imaging feature selection

Correlation-based feature selection.

Using the training dataset, we found that some imaging features significantly correlated to the CRS-R scores at the *T1* time point. For example, the connection features of some brain areas, including the anterior medial prefrontal cortex (aMPFC), posterior cingulate cortex/precuneus (PCC) and right lateral parietal cortex in the default mode network, and the dorsal medial prefrontal cortex (DMPFC) and left lateral superior parietal cortex in the executive control network, displayed significant correlations to the CRS-R *T1* scores across the DOC patients. We also found numerous examples of significant correlation between functional connectivity and the CRS-R score at the *T1* time point, with these functional connectivities being distributed both within and between brain networks. More information about the correlations between the imaging features and the CRS-R scores at the *T1* time point are provided in supplementary material 6.

CARS-PLSR feature selection.

Fig. 3 shows the final imaging features selected with CARS-PLSR. Specifically, the brain area connection features included the aMPFC and PCC in the default mode network, and the DMPFC in the executive control network. The functional connectivity features included the connectivity between the aMPFC in the default mode network and the DMPFC in the executive control network, as well as between

the middle cingulate cortex in the auditory network and the right lateral primary visual cortex in the visual network. More information about the feature selection by bootstrap is provided in supplementary material 7.

Prognostic model and internal validation

The prognostic model is presented in Fig. 4. Based on the regression formula, we noted some interesting findings. First, there were both positive and negative weights. In particular, the weights were all positive for the three brain area connection features. On the other hand, the functional connectivity between the aMPFC in the default mode network and the DMPFC in the executive control network was negative, and it had the maximum absolute weight. Second, the pie chart showed that the sum of the weights of the clinical features accounted for only about 30% of the total regression model. Third, the age and the anoxic etiology had negative weights, and the age predictor had the maximum absolute weight among the clinical features.

Fig. 5A presents the predicted score for each patient in the training dataset. As shown in Fig. 5B, there was good agreement between the CRS-R scores at the *T1* time point and the predicted scores. The apparent coefficient of determination R^2 was equal to 0.65 (permutation test, $p=0.001$), and the Bland-Altman plot verified the consistency between the predicted and achieved scores (one sample T test, $p=1.0$). The prognostic regression model was internally validated using bootstrap. The optimism-corrected coefficient of determination R^2 was equal to 0.28. Fig. 5C illustrates the number and proportion of DOC patients in each band of predicted scores. We found that the proportion of the patients with a “consciousness recovery”

outcome in the patient cohorts rose in conjunction with an increase in the predicted score. The higher the predicted score, the higher the proportion of patients who exhibited a favorable outcome. Fig. 5D shows the area under the ROC curve (AUC=0.96, 95% CI=0.89-0.99). Based on the ROC curve for the training dataset, the threshold 13.9 was selected as the cut-off point to classify the recovery of individual patients. In other words, if the predicted score for one patient was equal to or larger than 13.9, the classification model predicted the label "consciousness recovery" for this patient, otherwise as "consciousness non-recovery". The classification accuracy was assessed by comparing the predicted and actual outcomes, i.e. "consciousness recovery" (GOS>2) versus "consciousness non-recovery" (GOS≤2). Using this method, the classification accuracy in the training dataset was up to 92%. Specifically, the sensitivity was 85%, the specificity was 94%, the positive predictive value (PPV) was 79%, the negative predictive value (NPV) was 96%, and the F₁ score was 0.81.

Model external validation

The performance of the prediction model on the two testing datasets is illustrated in Fig. 6. As we assessed the CRS-R scores at the *T1* time point for the patients in the "Beijing HDxt" dataset, we calculated the coefficient of determination R^2 between these scores and the predicted scores. The R^2 was equal to 0.35 (permutation test, $p=0.005$), with the Bland-Altman plot also verifying the consistency between the predicted and actual scores (one sample T test, $p=0.89$). Using the predicted score 13.9 as the threshold, we then tested the classification accuracy on the two testing datasets. We found that, for the "Beijing HDxt" dataset, the prediction accuracy was

up to 88% (sensitivity: 83%, specificity: 92%, PPV: 92%, NPV:86%, F_1 score:0.87), while for the "Guangzhou HDxt" dataset it was also up to 88% (sensitivity: 100%, specificity:83%, PPV:67%, NPV:100%, F_1 score:0.80). More interestingly, for the testing dataset "Beijing HDxt", eight DOC patients who were initially diagnosed as VS/UWS subsequently recovered consciousness. Using the proposed model, we could successfully identify seven of these and there was only one false positive case. That is, for the VS/UWS patients, the model achieved 90.0% accuracy (sensitivity: 87.5%, specificity: 91.7%, PPV:87.5%, NPV:91.7%, F_1 score:0.875).

To test robustness, we evaluated whether the present prognostic regression model generalized to normal control subjects scanned in the "Beijing 750" training dataset (n=30) and the "Beijing HDxt" testing dataset (n=10). We found that both the normal controls and the "consciousness recovery" patients had significantly higher predicted imaging subscores than the "consciousness non-recovery" patients ($p<0.05$, multiple comparison corrected). Additional information is provided in supplementary material 8.

DISCUSSION

In this paper, we describe the development of a prognostic model that combines resting state fMRI with three clinical characteristics to predict one year outcomes at the single-subject level. The model discriminated between patients who would later recover consciousness and those who would not with an accuracy of around 90% on three datasets from two centers. It was also able to identify the prognostic importance of different predictors, including brain functions and clinical characteristics. We

therefore suggest that this novel multivariable prognostic model is accurate, robust, and interpretable.

Brain functions by the interactions between neurons within different neural circuits and brain regions. Brain functional imaging can detect the local activity of different brain regions and explore the interactions between them, and has demonstrated potential for informing diagnosis and prognosis in DOC. On the one hand, many studies have focused on one modality of brain functional imaging, including PET (Phillips et al., 2011), SPECT (Nayak and Mahapatra, 2011), task fMRI (Owen et al., 2006; Coyle et al., 2015), and resting state fMRI (Demertzi et al., 2015; Qin et al., 2015; Wu et al., 2015; Roquet et al., 2016). On the other hand, some cross-modality studies have compared the diagnostic precision when one imaging modality is used alone, for example, comparing PET imaging with task fMRI (Stender et al., 2014), or comparing PET, EEG and resting state fMRI (Golkowski et al., 2017). In our study, by combining brain functional networks detected from resting state fMRI with three clinical characteristics, we built a computational model that allowed us to make predictions regarding the prognosis of DOC patients at an individual level. We compared the models separately using only the imaging features or only the clinical characteristics (see supplementary material 9), and found that the combination of these predictors achieved an accuracy increase of about 10% and greater sensitivity and specificity. This validated the need for the use of accumulative evidence stemming from multiple assessments, each of which has different sensitivity and specificity in detecting the capacity for recovery of consciousness (Demertzi et al.,

2017). Validations in additional and unseen datasets were also undertaken to evaluate the feasibility of the predictive model. Our results showed that the average accuracy across the two testing datasets was about 88%, which suggested good robustness and the generalizability of our model.

According to the surviving consciousness level, DOC patients can be classified into distinct diagnostic entities, including VS/UWS and MCS. As MCS is often viewed as a state with a potentially more favorable outcome (Luaute *et al.*, 2010), a misdiagnosis of VS/UWS could heavily bias the judgment of the prognosis, the medical treatment options and even the associated ethical decisions. Unfortunately, more than 40% of DOC patients are misdiagnosed as VS/UWS when assessed using nonstandardized scales (Schnakers *et al.*, 2009). In fact, there have been cases of recovery from VS/UWS even after many years (Owen *et al.*, 2006; Estraneo *et al.*, 2010; Monti *et al.*, 2010). Instead of predicting diagnosis, this study used one year outcome as a target for regression and classification. Our method successfully identified seven out of the eight VS/UWS patients in the testing dataset who were initially diagnosed as VS/UWS but subsequently achieved a promising outcome.

Through analyzing the weights in the regression model, we were able to investigate the prognostic effects of these predictors. Firstly, we found that, for etiology, the regressor of trauma was positive, whereas the regressor of anoxia was negative, suggesting that trauma rather than anoxia is more likely to present a higher predicted score, and that trauma patients could have a relatively better outcome. The regressor of incidence age in the model was also negative, which demonstrated that

younger patients are more likely to have a higher prediction score than older patients. However, the duration of DOC was a positive regressor, indicating the necessity of long-term monitoring of patients with chronic DOC. In particular, the absolute value of the weight of the incidence age was greater than that of the other clinical characteristics, which suggested that incidence age might be the most important predictor among the clinical characteristics. Notably, in the regression formula, the imaging features accounted for a larger proportion of the total weights than the clinical features (70% vs. 30%), as shown in Fig. 4 (C). We speculated that the patient's residual consciousness capacity, indicated by brain networks and functional connectivity detected from resting state fMRI, might have a stronger prognostic effect in comparison to the clinical characteristics.

Some previous studies have shown that the resting state functional connectivity within the default mode network was decreased in severely brain-damaged patients, in proportion to their degree of consciousness impairment, from locked-in syndrome to minimally conscious, vegetative and coma patients (Vanhaudenhuyse *et al.*, 2010). Moreover, the reduced functional connectivity within the default mode network, specifically between the MPFC and the PCC, may predict the outcome of DOC patients (Silva *et al.*, 2015). Here, our model also validates that the aMPFC and PCC in the default mode network play important roles in predicting the prognosis.

Above all, we found that the functional connectivity between the aMPFC and the DMPFC had the maximum absolute weight in the prognostic regression model. The aMPFC is one of the core brain areas in the default mode network, whereas the

DMPFC is located in the executive control network. Previous studies have demonstrated that this functional connectivity is a negative connectivity in normal healthy populations, with the anti-correlation being proposed as one reflection of the intrinsic functional organization of the human brain (Fox *et al.*, 2005). The default mode network directly contributes to internally generated stimulus-independent thoughts, self-monitoring, and baseline monitoring of the external world, while the executive control network supports active exploration of the external world. Correct communication and coordination between these two intrinsic anti-correlated networks were thought to be very important for optimal information integration and cognitive functioning (Buckner *et al.*, 2008). A recent study found that negative functional connectivities between the default mode network and the task-positive network were only observed in patients who recovered consciousness and healthy controls, whereas positive values were obtained in patients with impaired consciousness (Di Perri *et al.*, 2016). Further, our regression model suggests that the anti-correlations between these two diametrically opposed networks (i.e., default mode network and executive control network) should be the most crucial imaging feature for predicting outcomes of the DOC patients. We therefore conclude that our prognostic model has good interpretability, and that it not only verifies the findings of previous studies but also provides a window to assess the relative significance of various predictors for the prognosis of DOC patients.

However, some caution is warranted. Firstly, a much larger cohort will be needed for further validation. The number of patients, in particular the patients who would

later recover consciousness, was relatively low in this study. Secondly, the signal-to-noise ratio of resting state fMRI would influence functional connectivity analysis, so calibrations will be necessary when applying the predictive model across different sites, including standardizing the MRI acquisition protocols (e.g. scanner hardware, imaging protocols and acquisition sequences) and the patients' management strategies (see supplementary material 10 for more information).

In summary, our novel prognostic model that combines resting state fMRI with clinical characteristics is proposed to predict the one year outcome of DOC patients at an individual level. The average accuracy of classifying a patient as "consciousness recovery" or not was around 90% in the training dataset and two unseen testing datasets. Our model also has good interpretability, and could provide a window to reassure physicians and scientists about the significance of different predictors, including brain networks, functional connectivities and clinical characteristics. Together, these advantages could help to offer an objective prognosis for DOC patients, optimize their management, and deepen our understanding of brain function during unconsciousness.

Acknowledgements

The authors appreciate the help of Ms Rowan Tweedale with the use of the English in this paper.

Funding

This work was partially supported by the Natural Science Foundation of China (Grant Nos. 81471380, 91432302, 31620103905), the Science Frontier Program of the Chinese Academy of Sciences (Grant No. QYZDJ-SSW-SMC019), National Key R&D Program of China (Grant No. 2017YFA0105203), Beijing Municipal Science & Technology Commission (Grant Nos. Z161100000216139, Z161100000216152), and the Guangdong Pearl River Talents Plan Innovative and Entrepreneurial Team grant (2016ZT06S220).

Supplementary material

References

- Bernat JL. Chronic disorders of consciousness. *Lancet* 2006; 367(9517): 1181-92.
- Bernat JL. Prognostic Limitations of Syndromic Diagnosis in Disorders of Consciousness. *AJOB Neuroscience* 2016; 7(1): 46-8.
- Booth CM, Boone RH, Tomlinson G, Detsky AS. Is this patient dead, vegetative, or severely neurologically impaired? Assessing outcome for comatose survivors of cardiac arrest. *Jama-Journal of the American Medical Association* 2004; 291(7): 870-9.
- Bruno M-A, Ledoux D, Vanhaudenhuyse A, Gosseries O, Thibaut A, Laureys S.

Prognosis of Patients with Altered State of Consciousness. In: Schnakers C, Laureys S, editors. *Coma and Disorders of Consciousness*. London: Springer London; 2012. p. 11-23.

Buckner RL, Andrews JR, Schacter DL. The Brain's Default Network. *Ann N Y Acad Sci* 2008; 1124: 1-38.

Celesia GG. Vegetative State Two Decades After the Multi-Society Task Force (MSTF) Report. *Brain Function and Responsiveness in Disorders of Consciousness*: Springer; 2016. p. 171-84.

Chennu S, Annen J, Wannez S, Thibaut A, Chatelle C, Cassoi H, *et al*. Brain networks predict metabolism, diagnosis and prognosis at the bedside in disorders of consciousness. *Brain* 2017; 140: 2120-32.

Coyle D, Stow J, McCreadie K, McElligott J, Carroll A. Sensorimotor Modulation Assessment and Brain-Computer Interface Training in Disorders of Consciousness. *Archives of Physical Medicine and Rehabilitation* 2015; 96(3): S62-S70.

Demertzi A, Antonopoulos G, Heine L, Voss HU, Crone JS, de Los Angeles C, *et al*. Intrinsic functional connectivity differentiates minimally conscious from unresponsive patients. *Brain* 2015; 138: 2619-31.

Demertzi A, Antonopoulos G, Voss HU, Crone JS, Schiff ND, Kronbichler M, *et al*. Audio-visual crossmodal fMRI connectivity differentiates single patients with disorders of consciousness. *Frontiers in Human Neuroscience: Belgian Brain Council 2014 MODULATING THE BRAIN: FACTS, FICTION, FUTURE*; 2014a.

Demertzi A, Gomez F, Crone JS, Vanhaudenhuyse A, Tshibanda L, Noirhomme Q, *et al*. Multiple fMRI system-level baseline connectivity is disrupted in patients with consciousness alterations. *Cortex* 2014b; 52: 35-46.

Demertzi A, Sitt J, Sarasso S, Pinxten W. Measuring states of pathological

(un)consciousness: research dimensions, clinical applications, and ethics; 2017.

Di Perri C, Bahri MA, Amico E, Thibaut A, Heine L, Antonopoulos G, *et al.* Neural correlates of consciousness in patients who have emerged from a minimally conscious state: a cross-sectional multimodal imaging study. *Lancet Neurology* 2016; 15(8): 830-42.

Dolce G, Quintieri M, Serra S, Lagani V, Pignolo L. Clinical signs and early prognosis in vegetative state: A decisional tree, data-mining study. *Brain Injury* 2008; 22(7-8): 617-23.

Dosenbach NUF, Nardos B, Cohen AL, Fair DA, Power JD, Church JA, *et al.* Prediction of Individual Brain Maturity Using fMRI. *Science* 2010; 329(5997): 1358-61.

Drysdale AT, Grosenick L, Downar J, Dunlop K, Mansouri F, Meng Y, *et al.* Resting-state connectivity biomarkers define neurophysiological subtypes of depression. *Nat Med* 2016; advance online publication.

Estraneo A, Moretta P, Loreto V, Lanzillo B, Cozzolino A, Saltalamacchia A, *et al.* Predictors of recovery of responsiveness in prolonged anoxic vegetative state. *Neurology* 2013; 80(5): 464-70.

Estraneo A, Moretta P, Loreto V, Lanzillo B, Santoro L, Trojano L. Late recovery after traumatic, anoxic, or hemorrhagic long-lasting vegetative state. *Neurology* 2010; 75(3): 239-45.

Fan W, Li H, Shan Y, Lv H, Zhang H, Liang Y. Classification of vinegar samples based on near infrared spectroscopy combined with wavelength selection. *Analytical Methods* 2011; 3(8): 1872-6.

Fan Y, Shen D, Gur RC, Gur RE, Davatzikos C. COMPARE: Classification of Morphological Patterns Using Adaptive Regional Elements. *IEEE Transactions on*

Medical Imaging 2007; 26(1): 93-105.

Fischer DB, Boes AD, Demertzi A, Evrard HC, Laureys S, Edlow BL, *et al.* A human brain network derived from coma-causing brainstem lesions. *Neurology* 2016; 87(23): 2427-34.

Fox MD, Snyder AZ, Vincent JL, Corbetta M, Van Essen DC, Raichle ME. The human brain is intrinsically organized into dynamic, anticorrelated functional networks. *Proc Natl Acad Sci U S A* 2005; 102(27): 9673-8.

Galanaud D, Perlberg V, Gupta R, Stevens RD, Sanchez P, Tollard E, *et al.* Assessment of White Matter Injury and Outcome in Severe Brain Trauma A Prospective Multicenter Cohort. *Anesthesiology* 2012; 117(6): 1300-10.

Giacino JT, Schnakers C, Rodriguez-Moreno D, Kalmar K, Schiff N, Hirsch J. Behavioral assessment in patients with disorders of consciousness: gold standard or fool's gold? In: Laureys S, Schiff ND, Owen AM, editors. *Coma Science: Clinical and Ethical Implications*. Amsterdam: Elsevier Science Bv; 2009. p. 33-48.

Golkowski D, Merz K, Mlynarcik C, Kiel T, Schorr B, Lopez-Rolon A, *et al.* Simultaneous EEG-PET-fMRI measurements in disorders of consciousness: an exploratory study on diagnosis and prognosis. *Journal of Neurology* 2017; 264(9): 1986-95.

Gosseries O, Zasler ND, Laureys S. Recent advances in disorders of consciousness: Focus on the diagnosis. *Brain Injury* 2014; 28(9): 1141-50.

Greicius MD, Srivastava G, Reiss AL, Menon V. Default-mode network activity distinguishes Alzheimer's disease from healthy aging: Evidence from functional MRI. *Proceedings of the National Academy of Sciences of the United States of America* 2004; 101(13): 4637-42.

Guyon I, Elisseeff A. An introduction to variable and feature selection. *Journal of*

Machine Learning Research 2003; 3(7-8): 1157-82.

He JH, Cui Y, Song M, Yang Y, Dang YY, Jiang TZ, *et al.* Decreased functional connectivity between the mediodorsal thalamus and default mode network in patients with disorders of consciousness. *Acta Neurologica Scandinavica* 2015; 131(3): 145-51.

Hofmeijer J, van Putten MJAM. EEG in postanoxic coma: Prognostic and diagnostic value. *Clinical Neurophysiology* 2016; 127(4): 2047-55.

Jennett B. Thirty years of the vegetative state: clinical, ethical and legal problems. In: Laureys S, editor. *Boundaries of Consciousness: Neurobiology and Neuropathology*; 2005. p. 537-43.

Kaneko T, Kasaoka S, Miyauchi T, Fujita M, Oda Y, Tsuruta R, *et al.* Serum glial fibrillary acidic protein as a predictive biomarker of neurological outcome after cardiac arrest. *Resuscitation* 2009; 80(7): 790-4.

Kang X-g, Li L, Wei D, Xu X-x, Zhao R, Jing Y-y, *et al.* Development of a simple score to predict outcome for unresponsive wakefulness syndrome. *Critical Care* 2014; 18(1).

Krishnan A, Williams LJ, McIntosh AR, Abdi H. Partial Least Squares (PLS) methods for neuroimaging: A tutorial and review. *Neuroimage* 2011; 56(2): 455-75.

Li H, Liang Y, Xu Q, Cao D. Key wavelengths screening using competitive adaptive reweighted sampling method for multivariate calibration. *Analytica Chimica Acta* 2009; 648(1): 77-84.

Li H, Xu Q, Liang Y. libPLS: an integrated library for partial least squares regression and discriminant analysis. *PeerJ PrePrints* 2014; 2: e190v1.

Luaute J, Maucourt-Boulch D, Tell L, Quelard F, Sarraf T, Iwaz J, *et al.* Long-term outcomes of chronic minimally conscious and vegetative states. *Neurology* 2010;

75(3): 246-52.

Luyt C-E, Galanaud D, Perlberg V, Vanhaudenhuyse A, Stevens RD, Gupta R, *et al.* Diffusion Tensor Imaging to Predict Long-term Outcome after Cardiac Arrest A Bicentric Pilot Study. *Anesthesiology* 2012; 117(6): 1311-21.

Maas AIR, Steyerberg EW, Butcher I, Dammers R, Lu J, Marmarou A, *et al.* Prognostic value of computerized tomography scan characteristics in traumatic brain injury: Results from the IMPACT study. *Journal of Neurotrauma* 2007; 24(2): 303-14.

Magrassi L, Maggioni G, Pistarini C, Di Perri C, Bastianello S, Zippo AG, *et al.* Results of a prospective study (CATS) on the effects of thalamic stimulation in minimally conscious and vegetative state patients. *Journal of Neurosurgery* 2016; 125(4): 972-81.

Mehmood T, Liland KH, Snipen L, Saebo S. A review of variable selection methods in Partial Least Squares Regression. *Chemometrics and Intelligent Laboratory Systems* 2012; 118: 62-9.

Monti MM, Vanhaudenhuyse A, Coleman MR, Boly M, Pickard JD, Tshibanda L, *et al.* Willful Modulation of Brain Activity in Disorders of Consciousness. *New England Journal of Medicine* 2010; 362(7): 579-89.

Nayak P, Mahapatra AK. Single photon emission computed tomography scanning: A predictor of outcome in vegetative state of head injury. *Journal of neurosciences in rural practice* 2011; 2(1): 12-6.

Noirhomme Q, Brecheisen R, Lesenfans D, Antonopoulos G, Laureys S. "Look at my classifier's result": Disentangling unresponsive from (minimally) conscious patients. *Neuroimage* 2017; 145: 288-303.

Owen AM, Coleman MR, Boly M, Davis MH, Laureys S, Pickard JD. Detecting awareness in the vegetative state. *Science* 2006; 313(5792): 1402-.

Phillips CL, Bruno M-A, Maquet P, Boly M, Noirhomme Q, Schnakers C, *et al.* "Relevance vector machine" consciousness classifier applied to cerebral metabolism of vegetative and locked-in patients. *Neuroimage* 2011; 56(2): 797-808.

Pignat J-M, Mauron E, Johr J, de Keranflec'h CG, Van De Ville D, Preti MG, *et al.* Outcome Prediction of Consciousness Disorders in the Acute Stage Based on a Complementary Motor Behavioural Tool. *Plos One* 2016; 11(6).

Power JD, Schlaggar BL, Petersen SE. Recent progress and outstanding issues in motion correction in resting state fMRI. *Neuroimage* 2015; 105: 536-51.

Qin P, Wu X, Huang Z, Duncan NW, Tang W, Wolff A, *et al.* How Are Different Neural Networks Related to Consciousness? *Ann Neurol* 2015; 78(4): 594-605.

Roquet D, Foucher JR, Froehlig P, Renard F, Pottecher J, Besancenot H, *et al.* Resting-state networks distinguish locked-in from vegetative state patients. *Neuroimage-Clinical* 2016; 12: 16-22.

Rossetti AO, Rabinstein AA, Oddo M. Neurological prognostication of outcome in patients in coma after cardiac arrest. *Lancet Neurology* 2016; 15(6): 597-609.

Rundgren M, Karlsson T, Nielsen N, Cronberg T, Johnsson P, Friberg H. Neuron specific enolase and S-100B as predictors of outcome after cardiac arrest and induced hypothermia. *Resuscitation* 2009; 80(7): 784-9.

Schnakers C, Vanhaudenhuyse A, Giacino J, Ventura M, Boly M, Majerus S, *et al.* Diagnostic accuracy of the vegetative and minimally conscious state: clinical consensus versus standardized neurobehavioral assessment. *BMC Neurol* 2009; 9(35).

Seeley WW, Menon V, Schatzberg AF, Keller J, Glover GH, Kenna H, *et al.* Dissociable intrinsic connectivity networks for salience processing and executive control. *Journal of Neuroscience* 2007; 27(9): 2349-56.

Sidaros A, Engberg A, Sidaros K, Liptrot MG, Herning M, Petersen P, *et al.* Diffusion

tensor imaging during recovery from severe traumatic brain injury and relation to clinical outcome: a longitudinal study. *Brain* 2008; 131: 559-72.

Silva S, de Pasquale F, Vuillaume C, Riu B, Loubinoux I, Geeraerts T, *et al.* Disruption of posteromedial large-scale neural communication predicts recovery from coma. *Neurology* 2015; 85(23): 2036-44.

Stender J, Gosseries O, Bruno M-A, Charland-Verville V, Vanhaudenhuyse A, Demertzi A, *et al.* Diagnostic precision of PET imaging and functional MRI in disorders of consciousness: a clinical validation study. *Lancet* 2014; 384(9942): 514-22.

Steppacher I, Eickhoff S, Jordanov T, Kaps M, Witzke W, Kissler J. N400 predicts recovery from disorders of consciousness. *Ann Neurol* 2013; 73(5): 594-602.

Stevens RD, Sutter R. Prognosis in Severe Brain Injury. *Critical Care Medicine* 2013; 41(4): 1104-23.

Steyerberg E. Clinical prediction models: a practical approach to development, validation, and updating: Springer Science & Business Media; 2008.

Tan B, Liang Y, Yi L, Li H, Zhou Z, Ji X, *et al.* Identification of free fatty acids profiling of type 2 diabetes mellitus and exploring possible biomarkers by GC-MS coupled with chemometrics. *Metabolomics* 2010; 6(2): 219-28.

The Multi-Society Task Force on PVS. Medical Aspects of the Persistent Vegetative State. *New England Journal of Medicine* 1994; 330(21): 1499-508.

Vanhaudenhuyse A, Noirhomme Q, Tshibanda LJF, Bruno MA, Boveroux P, Schnakers C, *et al.* Default network connectivity reflects the level of consciousness in non-communicative brain-damaged patients. *Brain* 2010; 133: 161-71.

Wannez S, Heine L, Thonnard M, Gosseries O, Laureys S, Coma Sci Grp C. The Repetition of Behavioral Assessments in Diagnosis of Disorders of Consciousness.

Ann Neurol 2017; 81(6): 883-9.

Wold S, Sjostrom M, Eriksson L. PLS-regression: a basic tool of chemometrics. Chemometrics and Intelligent Laboratory Systems 2001; 58(2): 109-30.

Wu X, Zou Q, Hu J, Tang W, Mao Y, Gao L, *et al.* Intrinsic Functional Connectivity Patterns Predict Consciousness Level and Recovery Outcome in Acquired Brain Injury. Journal of Neuroscience 2015; 35(37): 12932-46.

Yao S, Song J, Gao L, Yan Y, Huang C, Ding H, *et al.* Thalamocortical Sensorimotor Circuit Damage Associated with Disorders of Consciousness for Diffuse Axonal Injury Patients. Journal of the Neurological Sciences 2015; 356(1-2): 168-74.

Zandbergen EGJ, de Haan RJ, Stoutenbeek CP, Koelman J, Hijdra A. Systematic review of early prediction of poor outcome in anoxic-ischaemic coma. Lancet 1998; 352(9143): 1808-12.

Legend

Table 1 Demographic and clinical characteristics of the patients in the three datasets.

	Beijing_750 (n=63)	Beijing_HDxt (n=25)	Guangzhou_HDxt (n=24)
Gender, M/F	36/27	18/7	14/10
Etiology			
Trauma/Stroke/Anoxia	17/21/25	12/6/7	8/0/16
Age at the <i>T0</i> (years)			
Mean(SD)	42.8(13.8)	40.7(15.2)	39.3(16.9)
Range	18.0~71.0	18.0~68.0	15.0~78.0
Time to MRI (months)			
Range	1.0~77.0	1.0~44.0	1.0~10.0
Mean(SD)	7.4(12.8)	5.4(8.4)	2.3(2.4)
Median	3.0	3.0	1.5
Band			
[1,3]	32	13	20
(3,6]	15	8	2
(6,12]	11	3	2
>12	5	1	0
Follow-up time (months)			
Range	12.0~51.0	14.0~53.0	27.0~78.0
Mean(SD)	21.0(9.8)	41.7(8.4)	52.2(14.5)
Median	15.0	43.0	53.0
Band			
[12,24]	38	2	0
(24,48]	24	20	8
>48	1	3	16
Diagnosis at the <i>T0</i>			
MCS/VS	17/46	5/20	8/16
CRS-R total score			
Mean(SD)	7.3(2.9)	6.5(2.3)	7.1(4.1)
Range	3.0~18.0	3.0~14.0	3.0~17.0
Outcome at the <i>T1</i>			
CRS-R total score			
Mean(SD)	9.9(5.1)	12.7(6.4)	N/A
Range	3.0~22.0	5.0~23.0	N/A
GOS score			
GOS=5	0	0	0
GOS=4	5	5	1
GOS=3	8	7	5
GOS≤2	50	13	18

Abbreviations: CRS-R: Coma Recovery Scale–Revised; GOS: Glasgow Outcome Scale; MCS: minimally conscious state; N/A: not available; SD: standard deviation; VS: vegetative state/unresponsive wakefulness syndrome.

Fig. 1 Conceptual paradigm of the study. CRS-R: Coma Recovery Scale Revised scale;
GOS: Glasgow Outcome Scale.

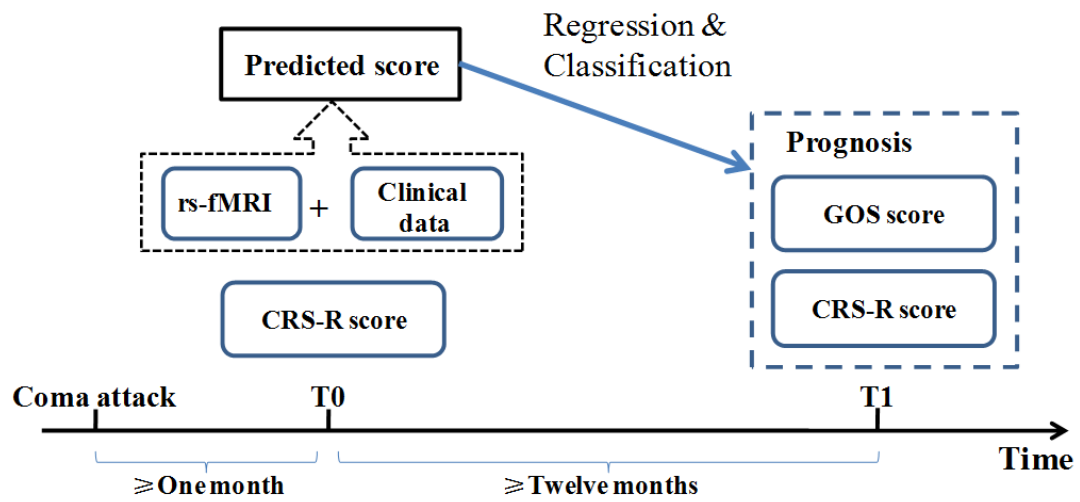


Fig. 2 Data analysis pipeline. All datasets involved in this study included resting state fMRI and clinical data. For the fMRI data in the training dataset, data analysis first encompassed preprocessing and imaging feature selection and extraction. Partial least square regression was then used to generate the regression model using the selected imaging features and clinical features in the training dataset. In this way, a prediction score that depicts the possibility of consciousness recovery was computed for each patient. The optimal cut-off value for classifying an individual patient as responsive or non-responsive was then calculated, and the prognostic classification model was obtained. The two testing datasets were only used to externally validate the regression and classification model.

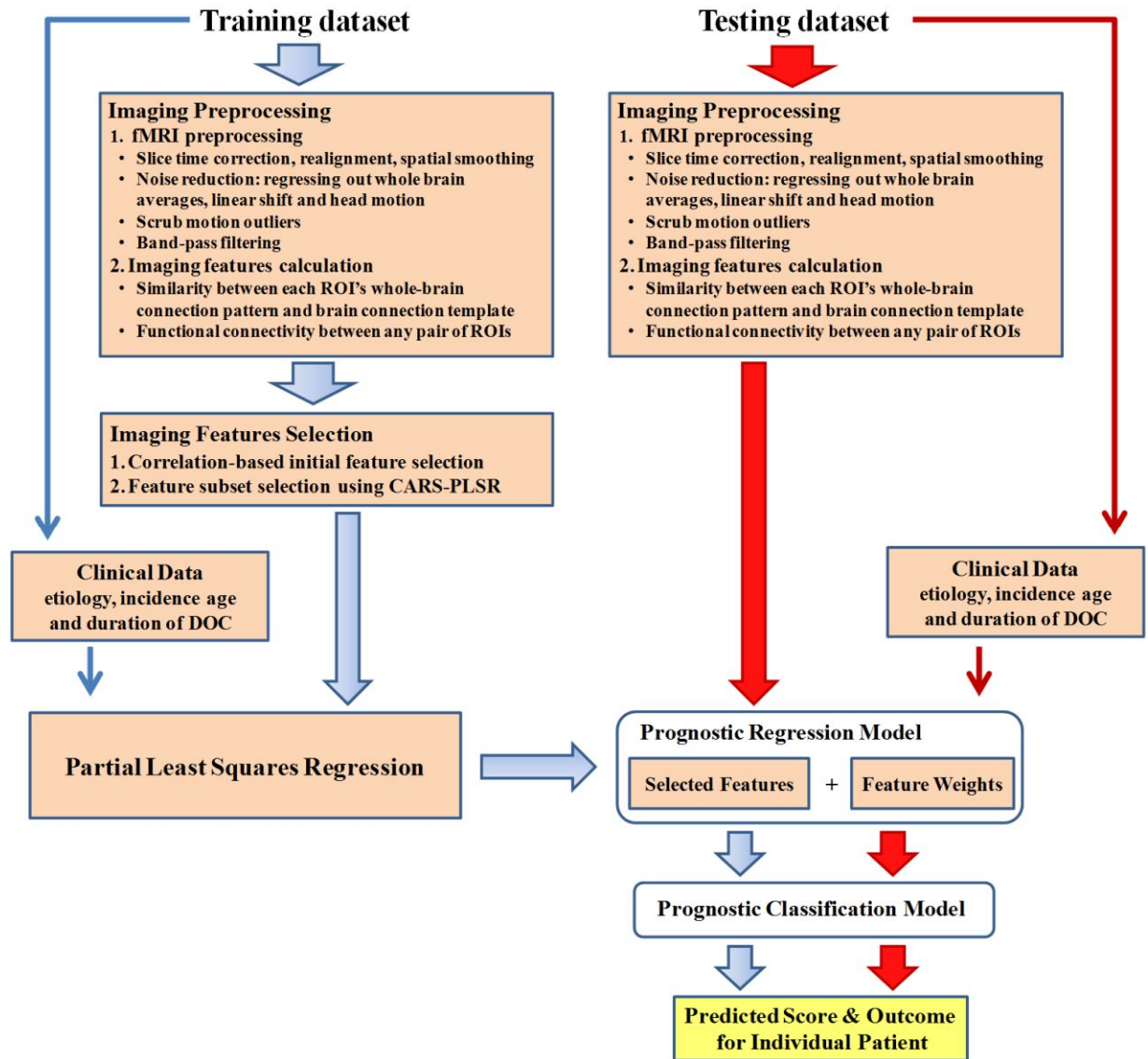
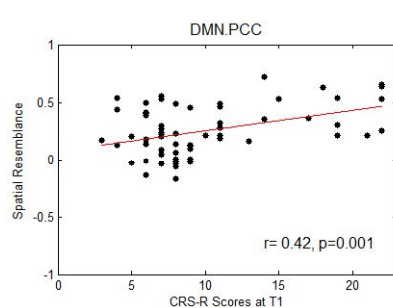
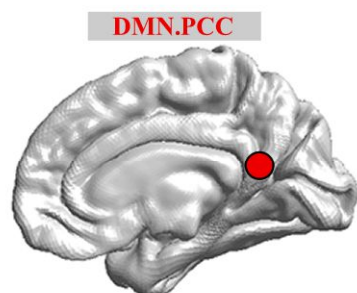
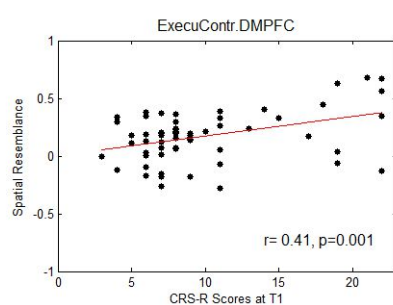
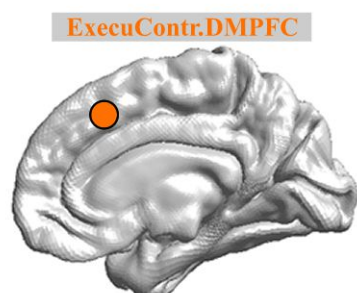
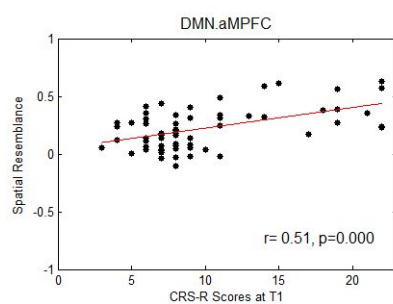
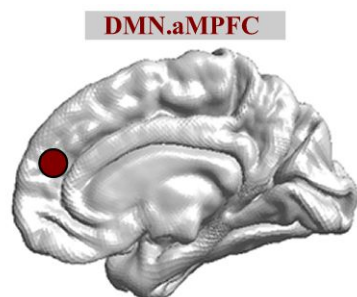
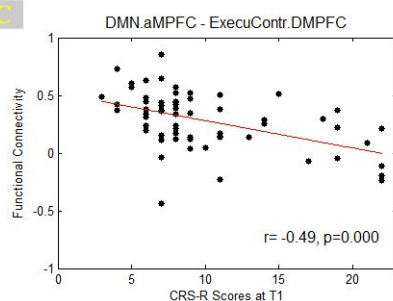
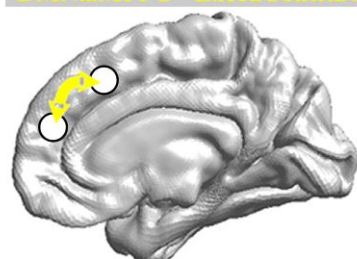


Fig. 3 Imaging features involved in the prognostic regression model. DMN.aMPFC: anterior medial prefrontal cortex in the default mode network; DMN.PCC: posterior cingulate cortex/precuneus in the default mode network; ExecuContr.DMPFC: dorsal medial prefrontal cortex in the executive control network; Auditory.MCC: middle cingulate cortex in the auditory network; Visual.R.V1: right lateral primary visual cortex in the visual network. DMN.aMPFC - ExecuContr.DMPFC: the functional connectivity between DMN.aMPFC and ExecuContr.DMPFC; Auditory.MCC - Visual.R.V1: the functional connectivity between Auditory.MCC and Visual.R.V1.



DMN.aMPFC - ExecuContr.DMPFC



Auditory.MCC - Visual.R.V1

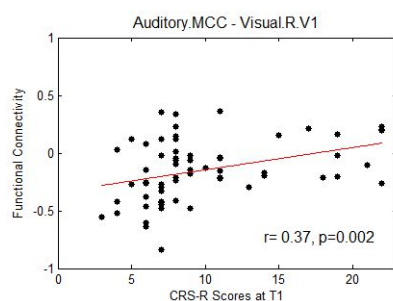
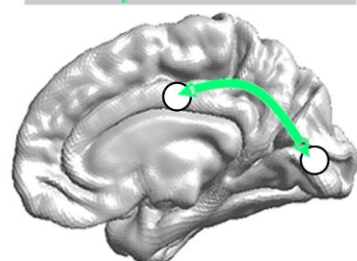


Fig. 4 Prognostic regression model. In the four subplots, each color denotes a particular predictor. **(A)**. Regression formula. **(B)**. Weights for each imaging and clinical feature in the regression model. The negative weights are shown to the left of the vertical blank line. The positive weights are shown to the right. **(C)**. A pie chart showing the weight distribution of the regression model. The exploded wedge represents the total distribution of the clinical features. **(D)**. The imaging features in the model are rendered on a 3D surface plot template in medial view.

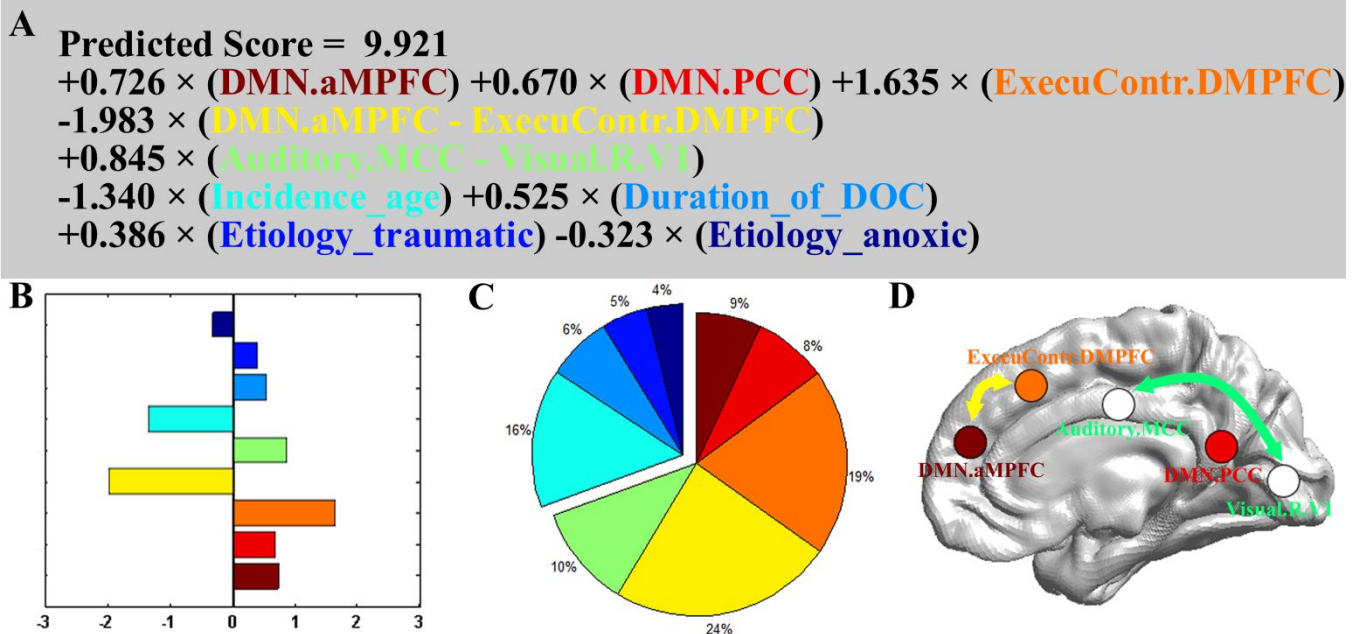
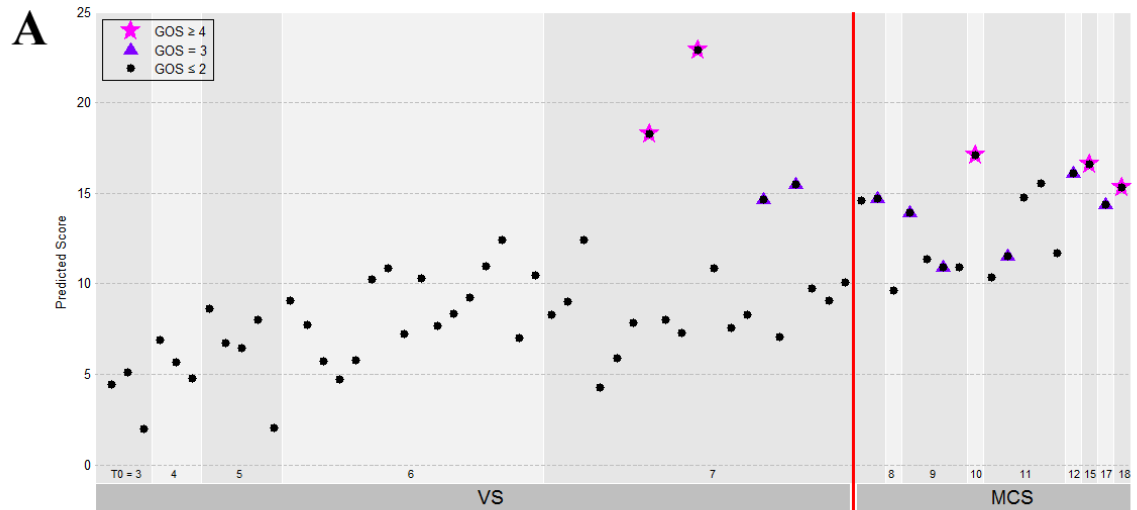


Fig. 5 The performance of the prediction model on the training dataset. **(A)**. Individual predicted scores for each DOC patient in the training dataset. The CRS-R score at the *T0* time point is shown on the x axis and the predicted score on the y axis. The patients diagnosed as VS/UWS at the *T0* time point are shown to the left of the vertical red solid line, whereas the patients diagnosed as MCS at this time point are shown to the right. The purplish red pentagram, imperial purple triangle and blank circle mark the patients with a GOS score ≥ 4 , $=3$ and ≤ 2 , respectively, at the *T1* time point. **(B)**. Agreement between the CRS-R scores at the *T1* time point and the predicted scores. The left panel shows the correlation between the CRS-R scores at the *T1* time point and the predicted scores, and the right panel shows the differences between them using the Bland-Altman plot. **(C)**. Bar chart showing the numbers or proportions of DOC patients in each band of predicted scores. In these two panels, the y axis shows the predicted score. **(D)**. The area under the receiver-operating characteristic (ROC) curve. The star on the curve represents the point with the maximal sum of true positive and false negative rates on the ROC curve, which were chosen as the cut-off threshold for classification. Here, the corresponding predicted score=13.9.



B Agreement between CRS-R Scores at T1 and Predicted Scores

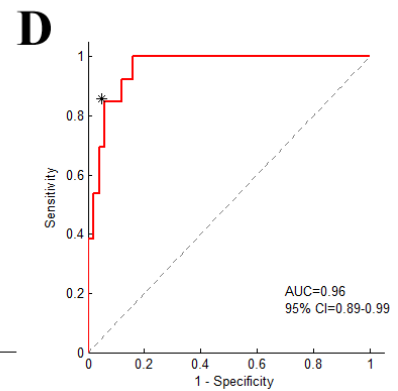
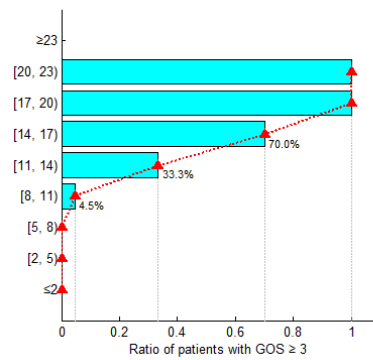
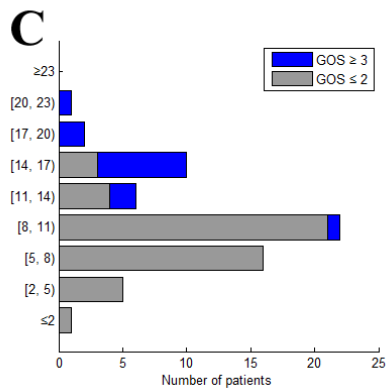
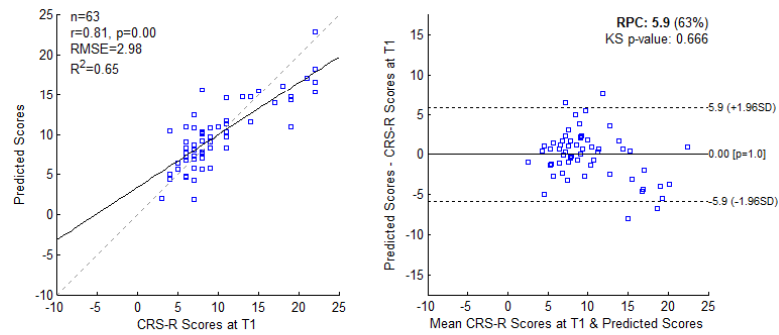
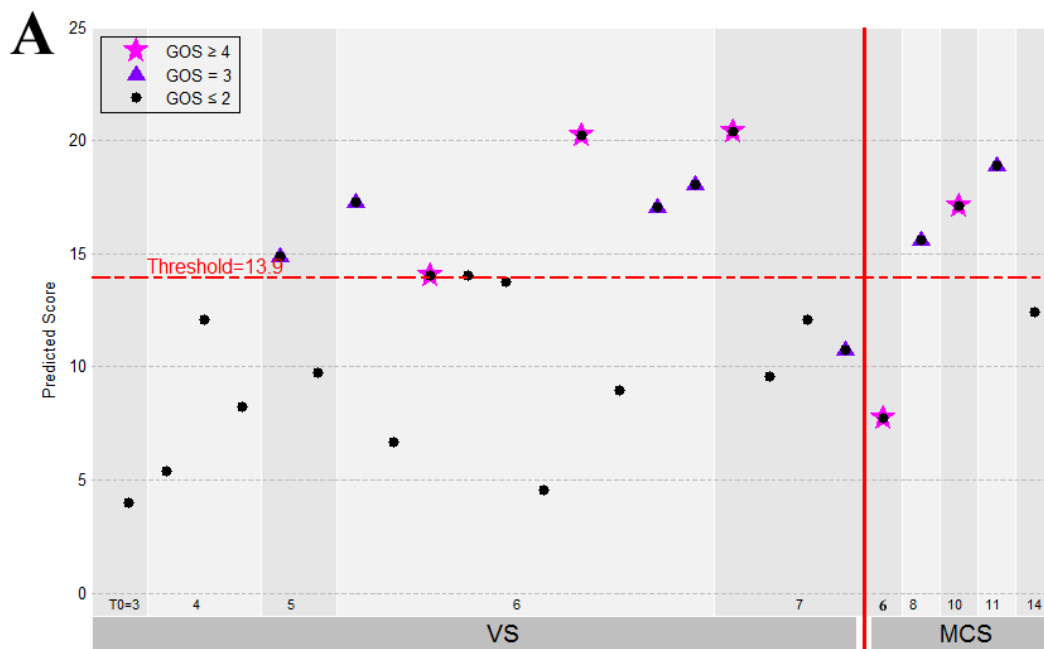
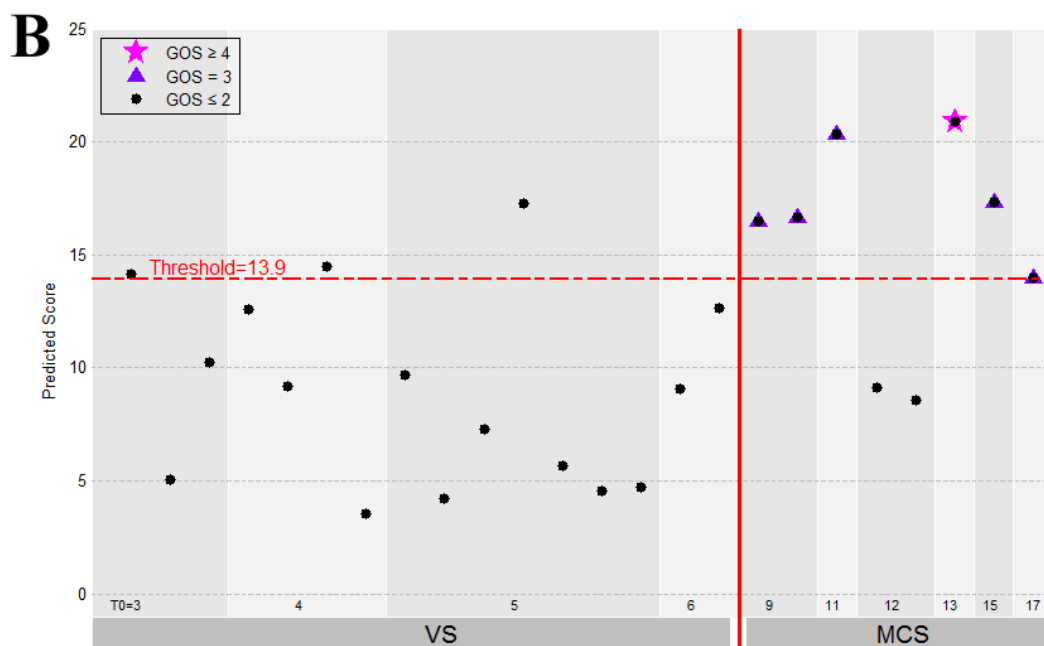
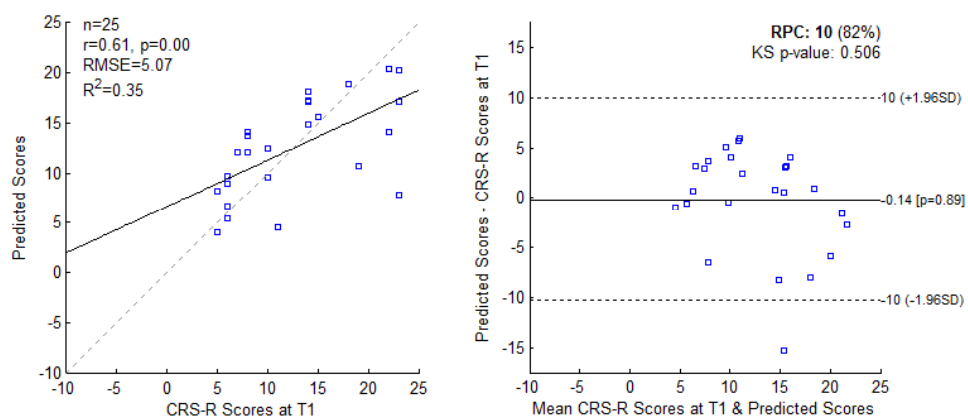


Fig. 6 The performance of the prediction model on the two testing datasets. **(A)**. The individual predicted score (top panel) and agreement between the CRS-R scores at the *T1* time point and the predicted scores (bottom panel) for the testing dataset "Beijing HxDt". **(B)**. The individual predicted score for each DOC patient in the testing dataset "Guangzhou HxDt". The legend description is same as for Fig. 5.



Agreement between CRS-R Scores at T1 and Predicted Scores



Supplementary Material 1: Demographics

Demographic and clinical characteristics of patients and normal controls in this study. The patients underwent the evaluations twice weekly (or more) within two weeks before MRI scanning. The highest CRS-R score was considered as the diagnosis and listed in the following tables. T0: the time point of the MRI scanning; T1: the time point of follow-up.

(1) Beijing_750 dataset:

patient alias	gender	age (years)	diagnose	etiology	structural lesions on MRI	time to MRI (months)	number of CRS-R assessments	CRS-R score at T0	CRS-R subscore at T0	CRS-R score at T1	CRS-R subscore at T1	follow-up (months)	GOS	predicted score
001	M	36	VS/UWS	Anoxia	Diffuse pons damage	1	6	7	022102	22	446323	15	4	18.26
002	M	29	MCS	Trauma	Bilateral-temporo-parietal damage	9	4	18	355113	22	456223	39	4	15.31
003	F	33	VS/UWS	Trauma	Bilateral-frontal lobe damage, atrophy	12	5	7	102202	22	455323	12	4	22.88
004	F	28	MCS	Trauma	L-frontal-temporal lobe damage	1	4	15	335103	22	456223	19	4	16.58

005	M	23	MCS	Anoxia	Diffuse cortical & subcortical atrophy	3	4	10	232102	21	455223	13	4	17.08
006	M	45	MCS	Stroke	L-temporo-parietal damage	9	4	9	222102	17	334223	12	3	13.94
007	M	39	MCS	Stroke	Brainstem damage	1	4	17	345113	19	445123	12	3	14.39
008	F	27	MCS	Trauma	L-basal ganglia damage	10	6	12	332103	18	345123	19	3	16.09
009	M	23	MCS	Trauma	Diffuse cortical & subcortical atrophy	6	4	9	132102	19	444223	13	3	10.94
010	M	42	MCS	Stroke	L-basal ganglia damage	3	7	7	103102	19	416323	12	3	14.72
011	M	53	MCS	Stroke	Diffuse cortical & basal ganglia (caudates) damage	7	5	11	332102	14	332123	14	3	11.55
012	F	40	VS/UWS	Stroke	Diffuse cortical & basal ganglia damage	5	6	7	112102	14	333122	12	3	14.67
013	M	22	VS/UWS	Trauma	L-frontal-temp	3	4	7	112102	15	334122	27	3	15.48

					oro-parietal lobe damage									
014	F	64	VS/UWS	Stroke	L-thalamus, basal ganglia lesions	1	4	7	112102	11	233102	17	2	8.28
015	F	42	VS/UWS	Anoxia	Diffuse anoxic cortical lesions	1	4	7	112102	9	222102	14	2	9.02
016	M	45	VS/UWS	Anoxia	Diffuse anoxic cortical lesions	9	5	5	002102	7	112102	15	2	8.65
017	F	60	VS/UWS	Anoxia	Diffuse anoxic cortical lesions	4	4	6	102102	6	102102	13	2	7.71
018	M	42	VS/UWS	Stroke	R-cerebral hemisphere lesions	6	4	7	112102	7	112102	14	2	12.44
019	M	51	VS/UWS	Anoxia	Diffuse cortical & subcortical atrophy	3	4	7	112102	7	112102	28	2	4.28
020	F	35	VS/UWS	Anoxia	Bilateral-front al lobe damage, atrophy	2	4	7	112102	7	112102	13	2	5.87
021	M	71	VS/UWS	Trauma	Diffuse cortical & subcortical atrophy	6	6	3	101100	4	101101	13	2	4.46

022	F	30	VS/UWS	Anoxia	Bilateral-basal ganglia damage	2	4	4	002002	7	022102	38	2	6.92
023	F	58	VS/UWS	Trauma	Diffuse cortical & subcortical atrophy	2	4	3	002100	4	002101	14	2	5.09
024	M	23	MCS	Trauma	R-basal ganglia (caudates) damage	5	5	7	103102	11	223202	12	2	14.57
025	F	66	VS/UWS	Trauma	Bilateral-temp oro-parietal damage	1	4	6	102102	8	113102	32	2	5.71
026	F	25	VS/UWS	Anoxia	Diffuse cortical & subcortical atrophy	3	4	5	102002	6	112002	36	2	6.75
027	M	48	VS/UWS	Anoxia	Diffuse cortical & subcortical atrophy	4	5	7	112102	8	113102	29	2	7.83
028	F	28	MCS	Anoxia	Diffuse cortical & subcortical atrophy	5	4	9	222102	11	233102	32	2	11.36

029	M	57	VS/UWS	Anoxia	Diffuse cortical & subcortical atrophy	11	4	6	102102	6	102102	33	2	4.70
030	M	61	MCS	Stroke	Bilateral-temp oro-parietal lobe damage	2	4	11	134102	11	223112	12	2	10.34
031	M	40	VS/UWS	Anoxia	Diffuse cortical & subcortical atrophy	4	4	4	001102	5	011102	27	2	5.70
032	M	39	VS/UWS	Stroke	R-basal ganglia damage, atrophy	3	4	7	112102	7	112102	12	2	8.03
033	M	41	VS/UWS	Anoxia	Diffuse cortical & subcortical atrophy	2	4	5	002102	5	002102	13	2	6.44
034	M	26	VS/UWS	Stroke	Diffuse cortical & subcortical atrophy	54	4	7	112102	7	112102	38	2	7.28
035	F	50	VS/UWS	Anoxia	Diffuse cortical & subcortical	8	6	6	102102	9	122202	12	2	5.77

					atrophy									
036	F	53	VS/UWS	Stroke	Bilateral brainstem, midbrain damage	3	4	5	112100	7	112102	28	2	8.02
037	M	67	VS/UWS	Stroke	R- brainstem, cerebellar damage	1	4	5	112100	3	002001	12	2	2.04
038	M	45	MCS	Stroke	Diffuse cortical & subcortical atrophy	2	5	9	132102	10	222112	13	2	10.91
039	F	35	VS/UWS	Anoxia	Diffuse cortical & subcortical atrophy	3	4	6	102102	8	112202	19	2	10.24
040	F	46	MCS	Trauma	Diffuse axonal injury	77	7	11	222212	13	332212	51	2	14.76
041	M	49	VS/UWS	Stroke	Bilateral-brain stem, cerebellar damage	10	4	7	112102	7	112102	28	2	10.87
042	M	45	VS/UWS	Stroke	Diffuse cortical & basal ganglia damage	3	4	7	112102	8	122102	19	2	7.59

043	M	18	VS/UWS	Anoxia	Diffuse cortical & subcortical atrophy	8	5	6	111102	9	123102	12	2	10.85
044	M	53	VS/UWS	Anoxia	Bilateral-occipital lobe damage, atrophy	2	4	3	002001	7	112102	34	2	1.98
045	M	46	VS/UWS	Trauma	R-temporo-parietal damage	4	4	6	101202	6	101202	13	2	7.23
046	F	29	VS/UWS	Anoxia	Diffuse cortical & subcortical atrophy	28	4	7	112102	9	123102	12	2	8.31
047	F	47	MCS	Stroke	R-basal ganglia damage	47	5	8	113102	11	222212	12	2	9.66
048	M	58	VS/UWS	Stroke	Bilateral-temporo-parietal lobe damage	6	4	7	112102	8	113102	27	2	7.05
049	M	66	VS/UWS	Anoxia	L-frontal lobe damage	4	4	4	002002	6	102102	38	2	4.79
050	M	34	VS/UWS	Trauma	Diffuse axonal injury	3	4	6	112101	8	122102	14	2	10.28
051	F	31	MCS	Trauma	L-frontal-temporo-parietal	3	5	11	133202	8	112202	15	2	15.56

					lobe damage									
052	M	33	VS/UWS	Stroke	L-temporo-parietal lobe damage	17	4	6	102102	8	113102	13	2	7.67
053	F	31	VS/UWS	Anoxia	Diffuse cortical & basal ganglia (caudates) damage	1	4	6	102102	6	102102	27	2	8.36
054	F	28	VS/UWS	Anoxia	Diffuse cortical & subcortical atrophy	3	4	6	102102	8	112202	32	2	9.23
055	F	26	VS/UWS	Stroke	L-basal ganglia damage	4	4	6	102102	6	102102	12	2	10.96
056	M	45	VS/UWS	Trauma	Diffuse axonal injury	1	4	6	102102	6	102102	29	2	9.05
057	F	69	VS/UWS	Stroke	Diffuse cortical & subcortical atrophy	4	4	6	102102	7	102202	33	2	12.43
058	F	68	VS/UWS	Trauma	Diffuse axonal injury	6	6	7	112102	9	132102	17	2	9.74
059	M	50	VS/UWS	Stroke	L-frontal-temporo-parietal lobe damage	3	4	6	111102	8	222002	27	2	7.01

060	M	60	MCS	Trauma	Bilateral brainstem, midbrain damage	7	4	11	134102	11	223112	30	2	11.69
061	M	44	VS/UWS	Anoxia	Diffuse cortical & subcortical atrophy	2	4	6	102102	4	002101	13	2	10.48
062	F	35	VS/UWS	Anoxia	Bilateral-basal ganglia damage	3	5	7	211102	9	231102	27	2	9.07
063	F	43	VS/UWS	Anoxia	Diffuse cortical & subcortical atrophy	2	4	7	112102	8	202112	29	2	10.09

(2) Beijing_HDxt dataset:

patient alias	gender	age (years)	diagnose	etiology	structural lesions on MRI	time to MRI (months)	number of CRS-R assessments	CRS-R score at T0	CRS-R subscore at T0	CRS-R score at T1	CRS-R subscore at T1	follow-up (months)	GOS	predicted score
001	M	19	VS/UWS	Trauma	L-temporo-parietal lobe damage	6	4	7	112102	22	456223	40	4	20.37
002	M	26	MCS	Trauma	R-thalamus, basal ganglia lesions	3	6	10	232102	23	456323	47	4	17.12
003	F	22	VS/UWS	Trauma	L-temporal lobe damage	4	4	6	102102	22	456223	47	4	14.05
004	M	41	VS/UWS	Stroke	Bilateral brainstem, midbrain damage	3	4	6	112101	23	456323	50	4	20.23
005	M	36	MCS	Stroke	Bilateral brainstem damage	4	4	6	003102	23	456323	39	4	7.75
006	M	34	VS/UWS	Anoxia	Diffuse cortical & subcortical atrophy	1	4	6	111102	14	323123	31	3	17.25
007	F	18	VS/UWS	Trauma	Diffuse axonal injury	3	4	5	012002	14	332123	41	3	14.86

008	M	58	MCS	Trauma	R-frontal lobe damage	12	4	8	113102	15	333123	40	3	15.62
009	M	41	MCS	Trauma	R-frontal-tem poro-parietal lobe damage	1	5	11	233012	18	344223	42	3	18.89
010	M	46	VS/UWS	Stroke	L-brainstem, cerebellar damage	7	4	6	102102	14	332123	53	3	17.05
011	M	25	VS/UWS	Anoxia	Diffuse cortical & subcortical atrophy	4	6	6	102102	14	224123	46	3	18.07
012	M	58	VS/UWS	Trauma	L-brainstem damage	1	7	7	112102	19	355123	40	3	10.75
013	M	36	VS/UWS	Trauma	L-frontal-tem poro-parietal lobe damage	6	4	7	112102	10	232102	44	2	9.58
014	M	58	VS/UWS	Trauma	R-frontal-tem poro-parietal lobe damage	4	4	6	102102	6	102102	45	2	6.69
015	M	65	VS/UWS	Stroke	Diffuse cortical & subcortical atrophy	3	4	3	100002	5	101102	43	2	4.01
016	F	24	VS/UWS	Trauma	Diffuse axonal injury	44	6	6	102102	8	122102	44	2	14.03

017	F	46	VS/UWS	Stroke	L-pons damage	2	4	7	112102	7	112102	40	2	12.11
018	M	53	VS/UWS	Anoxia	Diffuse cortical & subcortical atrophy	3	4	4	101002	6	102102	41	2	5.38
019	F	32	VS/UWS	Trauma	L-temporo-parietal lobe damage	3	4	6	102102	8	112202	23	2	13.76
020	M	41	VS/UWS	Anoxia	Diffuse cortical & subcortical atrophy	2	4	4	101002	8	112202	40	2	12.06
021	F	33	VS/UWS	Anoxia	Diffuse cortical & subcortical atrophy	7	5	6	211002	11	232202	47	2	4.55
022	M	49	VS/UWS	Anoxia	Diffuse cortical & subcortical atrophy	2	4	6	102102	6	102102	14	2	8.97
023	F	25	MCS	Anoxia	Bilateral thalamus, brainstem damage	4	7	14	450023	10	240022	50	2	12.42
024	M	63	VS/UWS	Stroke	L-basal	5	4	4	001102	5	101102	48	2	8.22

					ganglia lesions									
025	M	68	VS/UWS	Trauma	L-frontal-tem poro-parietal lobe damage	2	4	5	002102	6	012102	47	2	9.72

(3) Guangzhou_HDxt dataset:

patient alias	gender	age (years)	diagnose	etiology	time to MRI(months)	CRS-R score at T0	CRS-R subscore at T0	follow-up (months)	GOS	predicted score
001	F	15	MCS	Anoxia	1	13	135112	59	4	20.92
002	M	29	MCS	Trauma	4	9	114012	61	3	16.50
003	F	27	MCS	Trauma	1	9	105102	29	3	16.67
004	F	20	MCS	Trauma	2	8	113102	41	3	20.37
005	M	30	MCS	Trauma	1	15	116223	63	3	17.34
006	M	31	MCS	Trauma	1	20	445223	51	3	14.00
007	M	28	VS/UWS	Anoxia	1	5	102002	69	2	9.71
008	M	48	MCS	Trauma	1	12	234102	55	2	9.11
009	M	46	VS/UWS	Trauma	2	4	102001	65	2	12.58
010	M	78	VS/UWS	Anoxia	1	4	100102	49	2	9.20
011	M	39	VS/UWS	Anoxia	1	5	002102	51	2	4.20
012	F	46	VS/UWS	Anoxia	2	4	001102	46	2	14.49
013	M	39	VS/UWS	Anoxia	2	5	102002	43	2	7.30
014	M	16	VS/UWS	Anoxia	2	3	001002	71	2	14.17
015	M	25	MCS	Anoxia	1	12	135102	78	2	8.56
016	F	76	VS/UWS	Anoxia	5	4	100102	59	2	3.57
017	M	36	VS/UWS	Trauma	2	5	001202	65	2	17.28
018	M	32	VS/UWS	Anoxia	10	6	102102	56	2	5.66
019	F	49	VS/UWS	Anoxia	1	6	102102	49	2	4.55
020	F	52	VS/UWS	Anoxia	1	3	000102	27	2	5.08
021	M	62	VS/UWS	Anoxia	2	3	001002	28	2	10.26

022	F	33	VS/UWS	Anoxia	2	6	102102	29	2	9.09
023	F	28	VS/UWS	Anoxia	9	6	102102	67	2	12.62
024	F	57	VS/UWS	Anoxia	1	5	002102	42	2	4.72

(4) Beijing_750_normal_control:

alias	gender	age	handedness
NC001	F	40	Right
NC002	M	50	Right
NC003	F	34	Right
NC004	M	25	Right
NC005	M	28	Right
NC007	F	24	Right
NC008	F	47	Right
NC009	F	22	Right
NC010	F	60	Right
NC012	F	26	Right
NC013	M	21	Right
NC014	F	27	Right
NC015	M	40	Right
NC016	M	44	Right
NC017	F	22	Right
NC018	M	50	Right
NC019	M	27	Right
NC020	F	43	Right
NC021	F	25	Right
NC022	M	54	Right
NC023	F	52	Right
NC026	M	46	Right

NC027	F	52	Right
NC028	M	29	Right
NC029	F	46	Right
NC030	M	44	Right
NC031	M	30	Right
NC032	M	31	Right
NC033	M	32	Right
NC034	M	30	Right

(5) Beijing_HDxt_normal_control:

alias	gender	age	handedness
NC001_HDxt	M	44	Right
NC002_HDxt	M	42	Right
NC003_HDxt	M	30	Right
NC004_HDxt	M	40	Right
NC005_HDxt	M	30	Right
NC006_HDxt	M	30	Right
NC007_HDxt	F	58	Right
NC008_HDxt	F	54	Right
NC009_HDxt	F	41	Right
NC010_HDxt	F	41	Right

Supplementary Material 2: Regions of Interest

The six brain networks investigated in this study and the names of regions of interest (ROI). The following table represented the six brain networks, the name of ROIs, the peak coordinates in the Montreal Neurological Institute (MNI) space and the corresponding references. All of ROI were defined as a spherical region with a radius of 6mm at the center of the peak coordinates of the ROI.

Brain Network	ROI name	ROI Abbreviation	Peak MNI coordinates	References
Default mode				(Raichle, 2011, Demertzi et al., 2015)
	Anterior medial prefrontal cortex	aMPFC	-1 54 27	
	Posterior cingulate cortex/precuneus	PCC	0 -52 27	
	Left lateral parietal cortex	L.LatP	-46 -66 30	
	Right lateral parietal cortex	R.LatP	49 -63 33	
Executive control				(Seeley et al., 2007, Raichle, 2011)
	Dorsal medial PFC	DMPFC	0 27 46	
	Left anterior prefrontal cortex	L.PFC	-44 45 0	
	Right anterior prefrontal cortex	R.PFC	44 45 0	
	Left superior parietal cortex	L. Parietal	-50 -51 45	
	Right superior parietal cortex	R. Parietal	50 -51 45	
Salience				(Seeley et al., 2007, Raichle, 2011, Demertzi et al., 2015)
	Left orbital frontoinsula	L.AIns	-40 18 -12	
	Right orbital frontoinsula	R.AIns	42 10 -12	
	Dorsal anterior cingulate	dACC	0 18 30	
Sensorimotor				(Raichle, 2011, Demertzi et al., 2015)
	Left primary motor cortex	L.M1	-39 -26 51	
	Right primary motor cortex	R.M1	38 -26 51	
	Supplementary motor area	SMA	0 -21 51	
Auditory				(Raichle, 2011, Demertzi et al.,

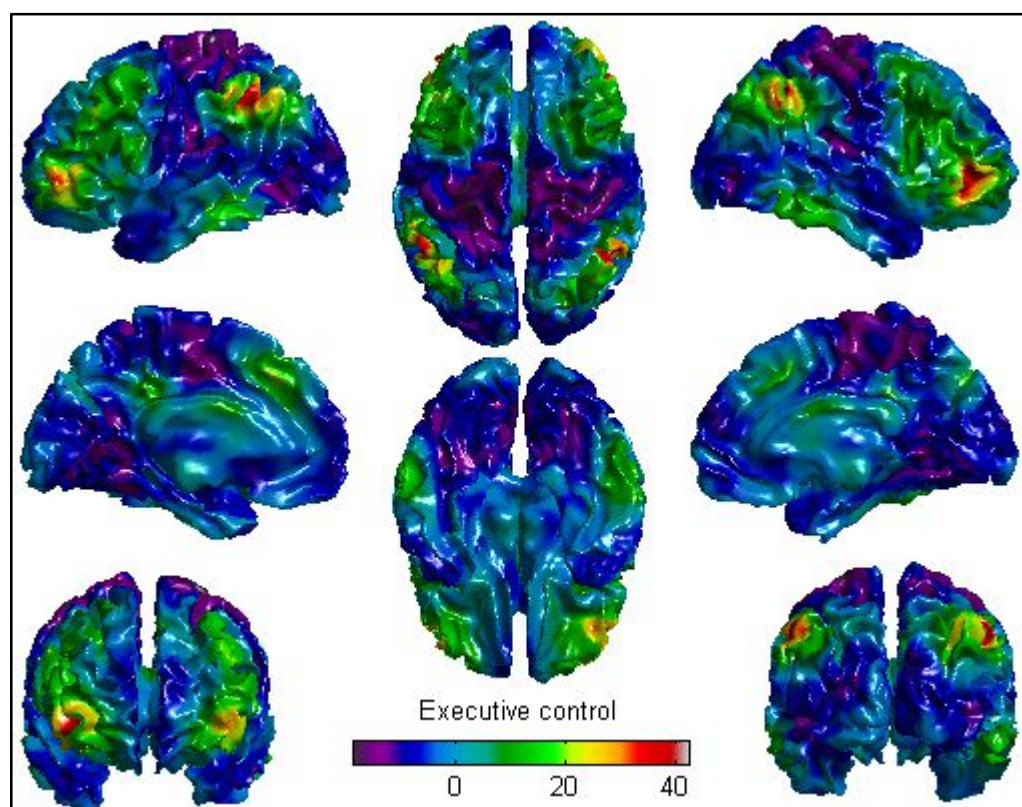
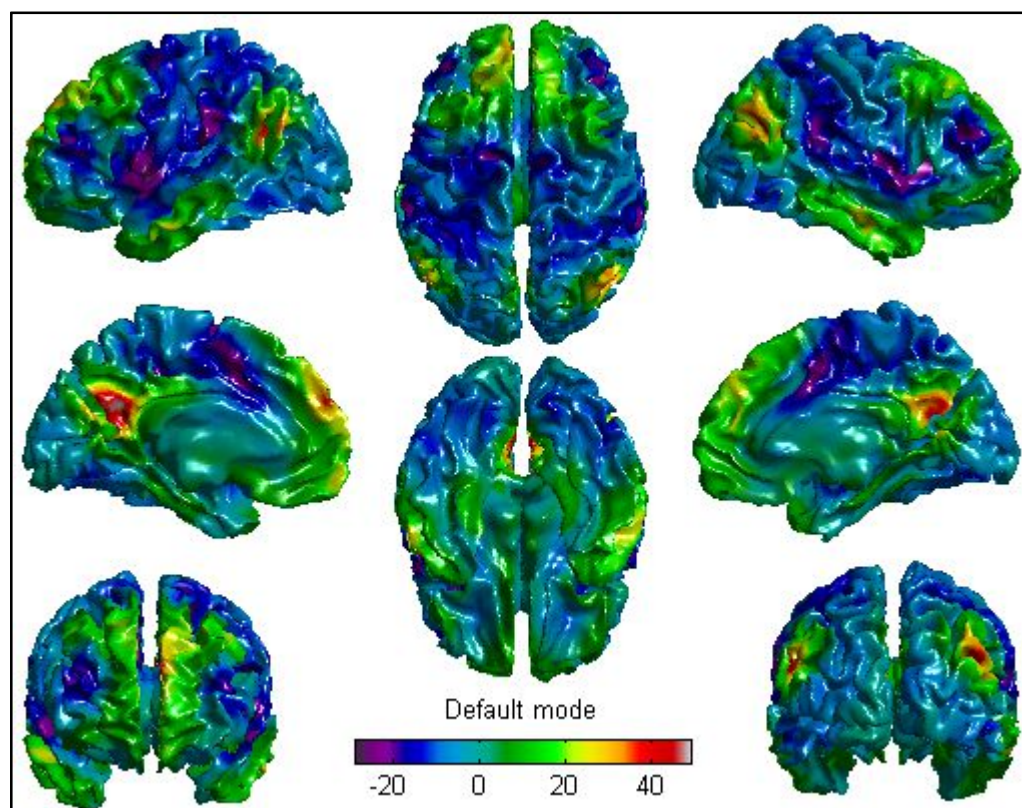
Brain Network	ROI name	ROI Abbreviation	Peak MNI coordinates	References
				2015)
	Left Primary auditory cortex	L.A1	-62 -30 12	
	Right Primary auditory cortex	R.A1	59 -27 15	
	Middle cingulate cortex	MCC	0 -7 43	
Visual				(Demertzi et al., 2015)
	Left primary visual cortex	L.V1	-13 -85 6	
	Right primary visual cortex	R.V1	8 -82 6	
	Left associative visual cortex	L.V4	-30 -89 20	
	Right associative visual cortex	R.V4	30 -89 20	

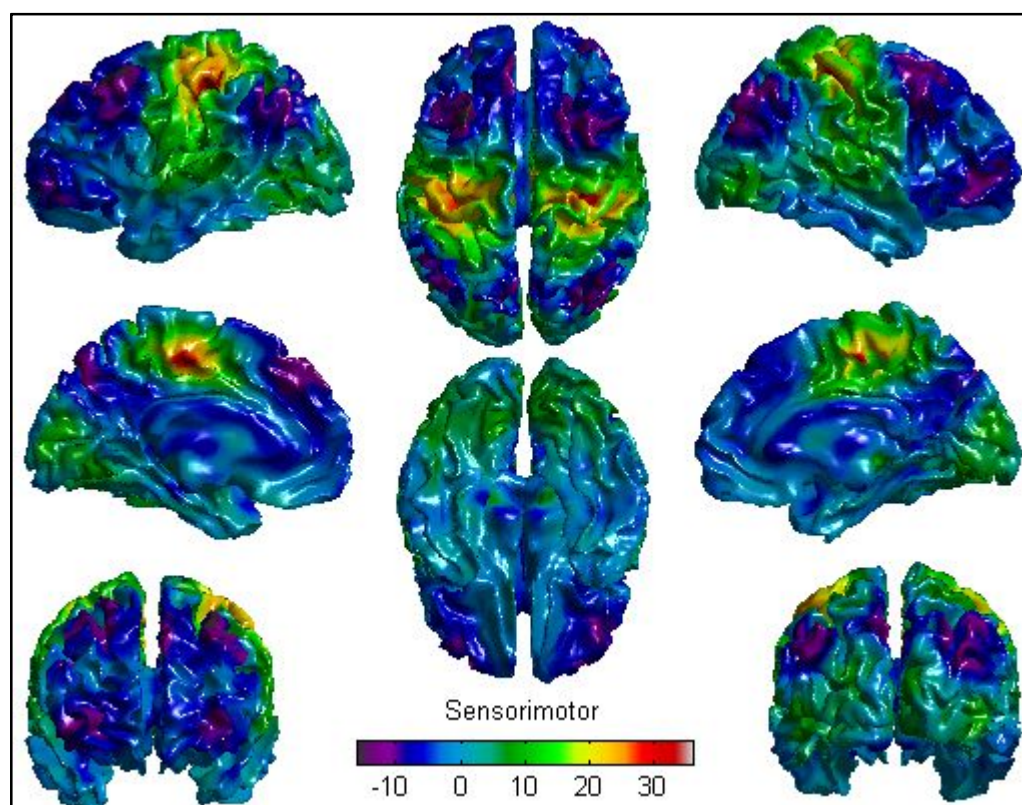
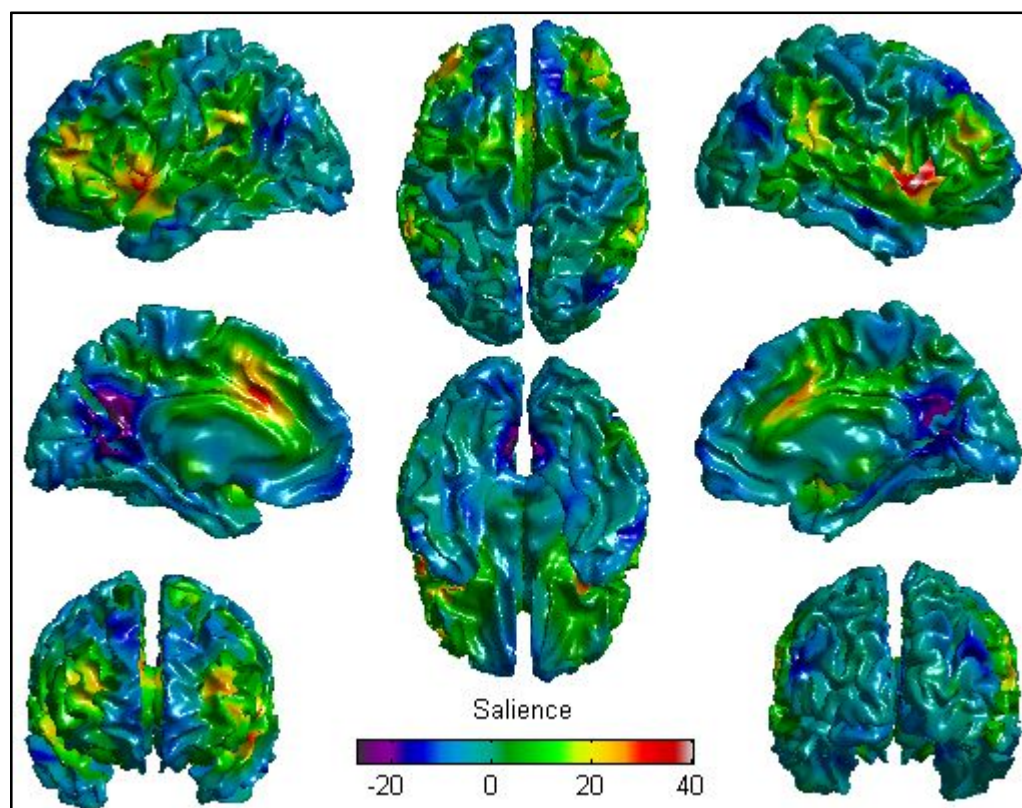
References:

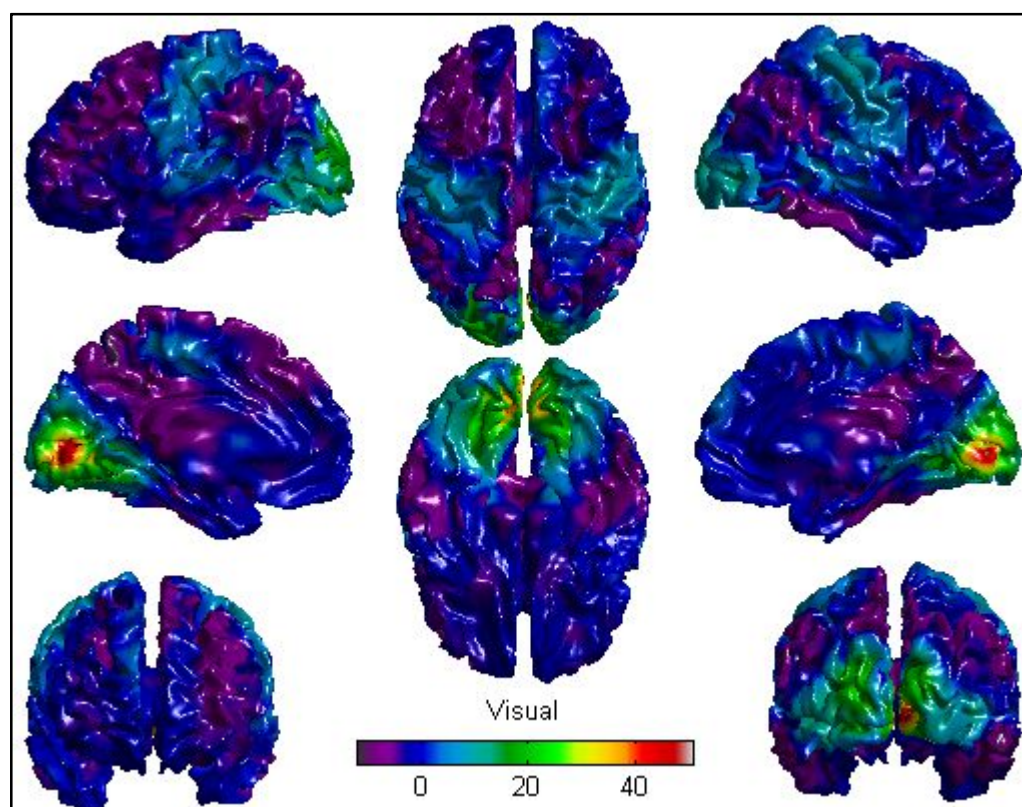
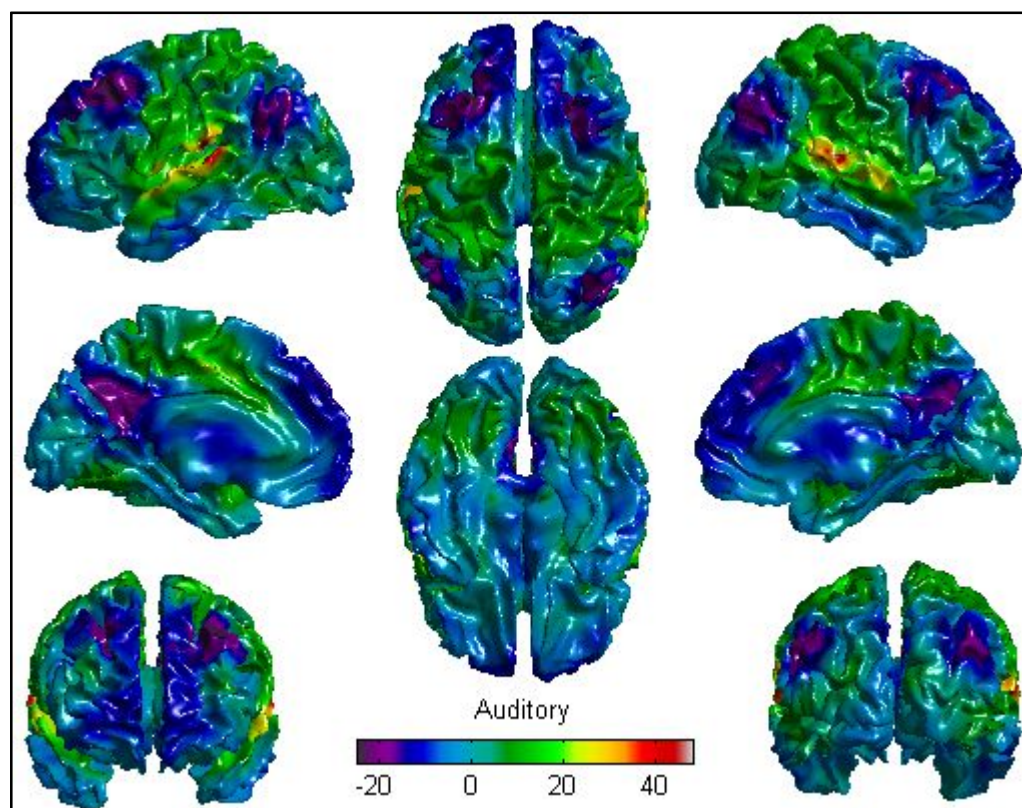
- Demertzi A, Antonopoulos G, Heine L, Voss HU, Crone JS, de Los Angeles C, Bahri MA, Di Perri C, Vanhaudenhuyse A, Charland-Verville V, Kronbichler M, Trinka E, Phillips C, Gomez F, Tshibanda L, Soddu A, Schiff ND, Whitfield-Gabrieli S, Laureys S (2015) Intrinsic functional connectivity differentiates minimally conscious from unresponsive patients. *Brain* 138:2619-2631.
- Raichle ME (2011) The restless brain. *Brain connectivity* 1:3-12.
- Seeley WW, Menon V, Schatzberg AF, Keller J, Glover GH, Kenna H, Reiss AL, Greicius MD (2007) Dissociable intrinsic connectivity networks for salience processing and executive control. *Journal of Neuroscience* 27:2349-2356.

Supplementary Material 3: Brain Functional Network Templates

Although the neurobiological implications of the spontaneous neuronal activity are not very clear, spontaneous fluctuations in the blood oxygenation level-dependent signal have been found to be coherent within a variety of functionally relevant brain regions, which are denoted as representing a "network". Moreover, several networks have been found to be spatially consistent across different subjects (Damoiseaux et al., 2006). Researchers suggested that the brain networks assessed by resting state fMRI may reflect an intrinsic functional architecture of the brain (Raichle, 2011). As mentioned in the manuscript, multiple networks were reported to be disrupted in the DOC patients. Here, this study focused on the cortex, so six functional networks were investigated, including default mode network, executive control network, salience, sensorimotor, auditory, and visual network. The six brain functional network templates were created for the corresponding brain networks. These templates were separately shown on the brain surface using the SurfStat toolbox (<http://www.math.mcgill.ca/keith/surfstat/>).







References:

- Damoiseaux JS, Rombouts SA, Barkhof F, Scheltens P, Stam CJ, Smith SM, Beckmann CF (2006)
Consistent resting-state networks across healthy subjects. Proc Natl Acad Sci U S A
103:13848-13853.
- Raichle ME (2011) The restless brain. Brain connectivity 1:3-12.

Supplementary Material 4: Quality Control for Resting State Functional Connectivity

During the MRI scanning, the foam pad and headphones were used to reduce head motion and scanner noise. The normal controls were instructed to keep still with their eyes closed, as motionless as possible and not to think about anything in particular. The same instructions were given to the patients but due to their consciousness and cognitive impairments, we could not fully control for a prolonged eye-closed yet awake scanning session.

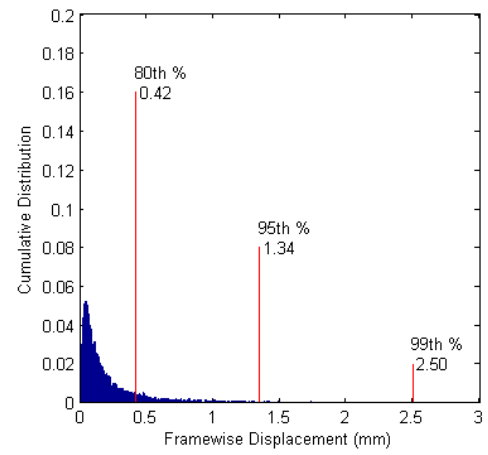
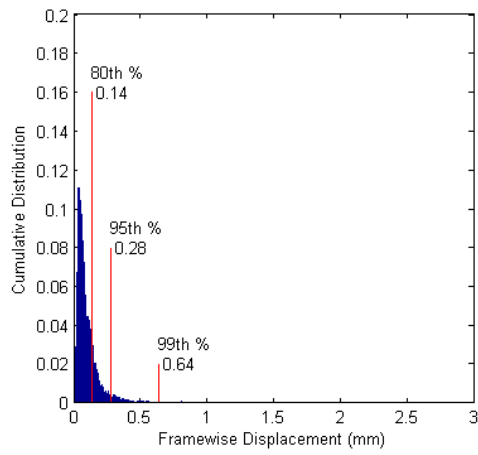
The section (**A**) shows cumulative distribution of head motion per volume (framewise displacement) for normal controls and the patients. The section (**B**) shows the results of control quality of resting state fMRI in this study. The section (**C**) shows the histogram of the remaining number of fMRI volumes after scrubbing.

(A). Cumulative distribution of head motion per volume (framewise displacement) for normal controls and DOC patients separately in the training dataset "Beijing 750" (A1), the testing dataset "Beijing HDxt" (A2), and the testing dataset "Guangzhou HDxt" (A3). The normal controls were shown in left column, whereas the DOC patients were shown in right column. No healthy control data were available for the Guangzhou centre. In both patients and controls, head position was stable to within 1.5 mm for the vast majority (>95%) of brain volumes.

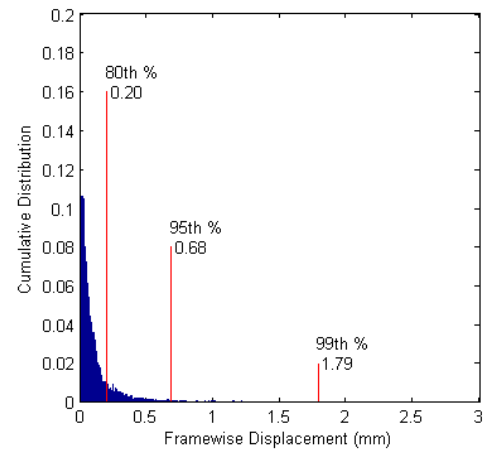
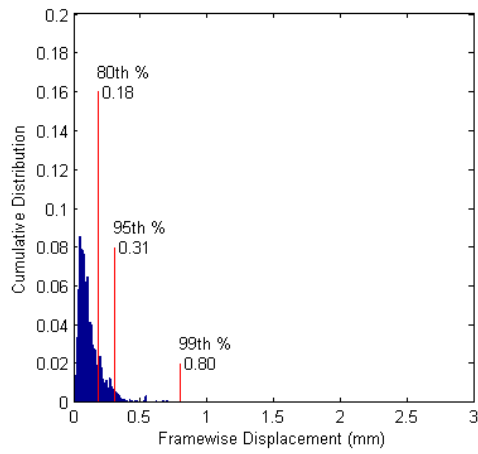
Normal Controls

DOC Patients

A1

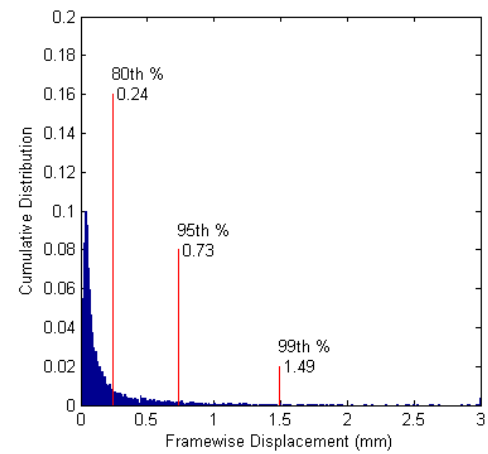


A2



A3

N/A

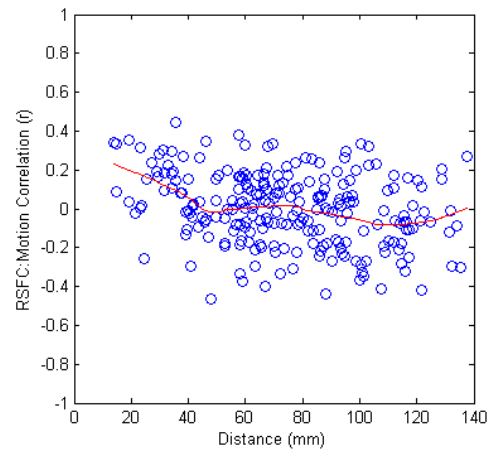
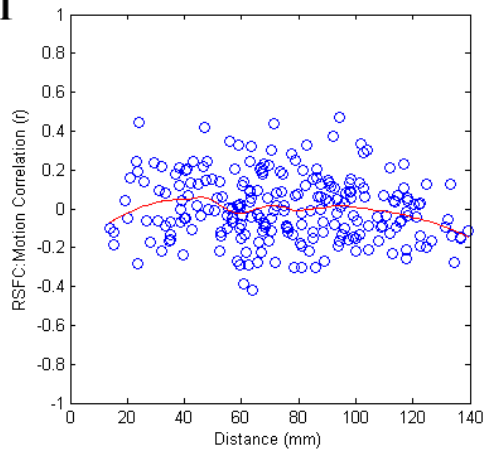


(B) Correlations between motion artifact and neuroanatomical distance between the ROIs in this study. Prior studies have shown that motion artifacts tend to vary with neuroanatomical distance between brain nodes. Here, we conducted quality control analyses as described in the previous study (Power et al., 2015). Specifically, we computed correlations between head motion (mean FD) and each resting state functional connectivity (RSFC) feature and plotted them as a function of neuroanatomical distance (mm) for subjects in the training dataset "Beijing 750" (B1), the testing dataset "Beijing HDxt" (B2), and the testing dataset "Guangzhou HDxt" (B3). Smoothing curves (in red) were plotted using a moving average filter.

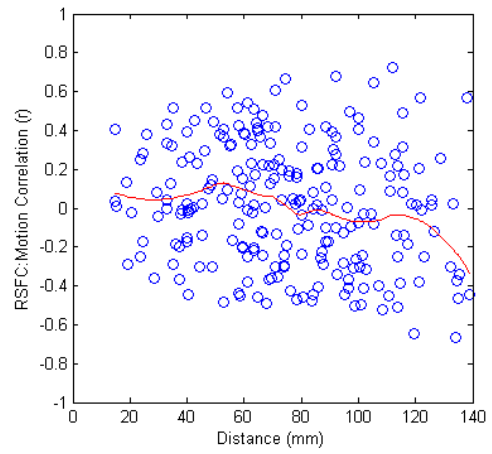
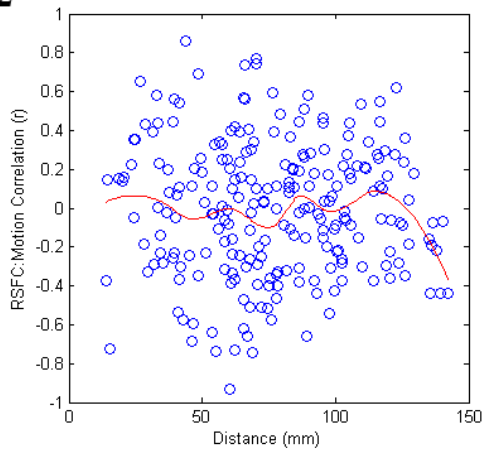
Normal Controls

DOC Patients

B1

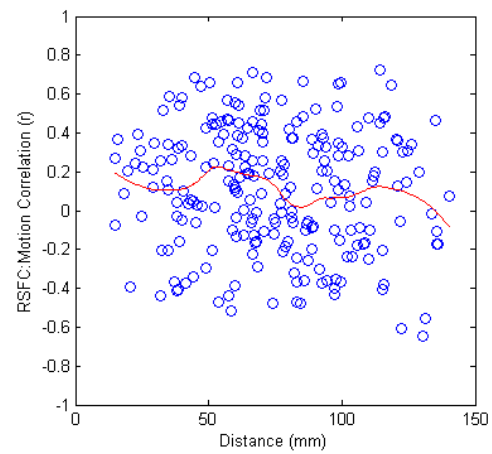


B2

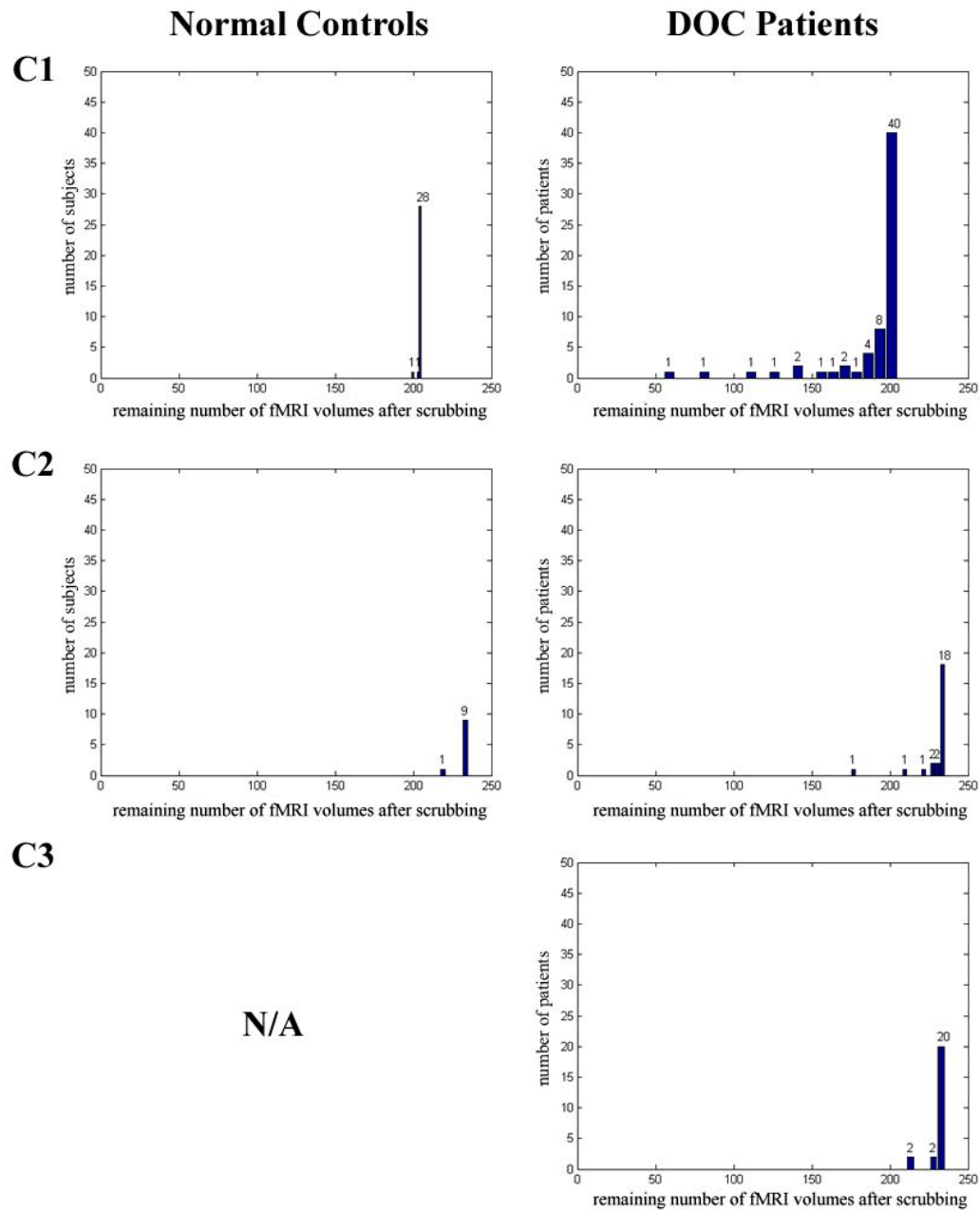


B3

N/A



(C) Histogram of the remaining number of fMRI volumes after scrubbing for each population, specifically "Beijing 750" dataset (C1), "Beijing HDxt" dataset (C2), and "Guangzhou HDxt" dataset (C3).



References:

Power JD, Schlaggar BL, Petersen SE (2015) Recent progress and outstanding issues in motion correction in resting state fMRI. *Neuroimage* 105:536-551.

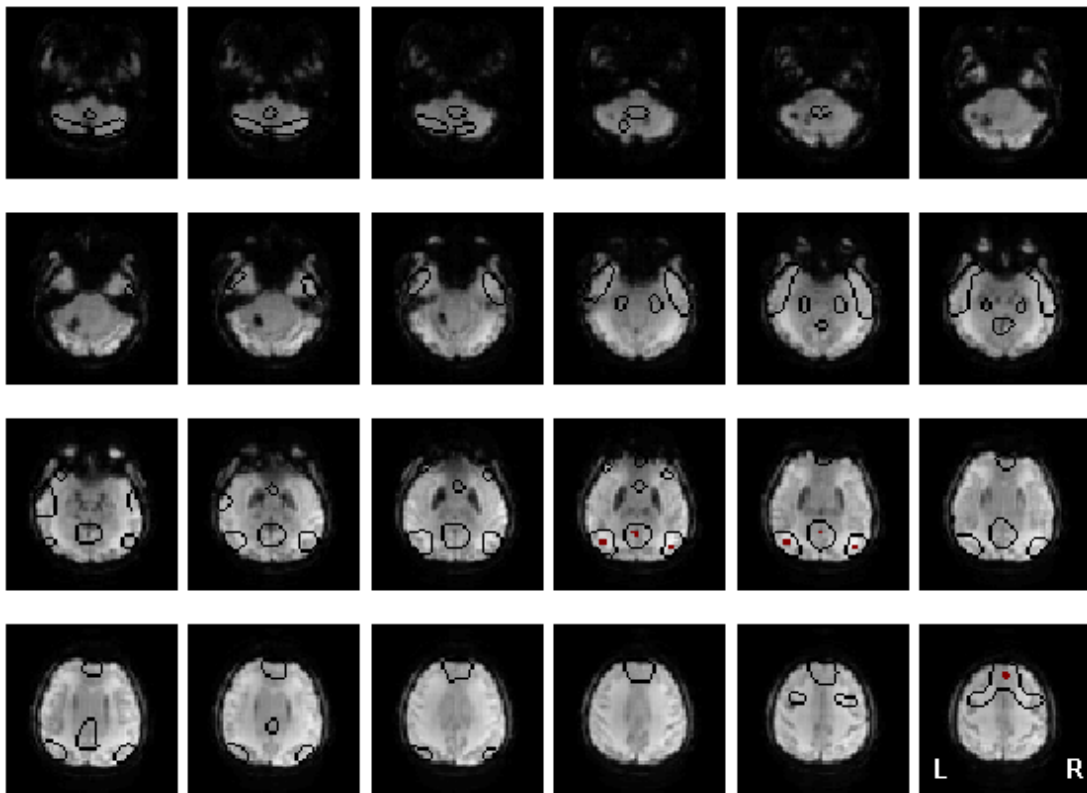
Supplementary Material 5: Warped Regions of Interest & Brain Network templates

The conventional fMRI preprocess normalizes individual fMRI images into a standard space defined by a specific template image. Here, we generated a functional connectivity image for each patient in his/her own fMRI space. During the preprocessing of each patient's fMRI scans, the 22 ROIs and the 6 brain network templates were spatially warped to individual fMRI space and resampled to the voxel size of the individual fMRI image. To ensure the registration, we developed some tools to visually check the transformed ROIs and brain network templates for each subject in this study.

As the examples, we here illustrate the warped ROIs in the default mode network (DMN) for the 3 DOC patients with a GOS score 2,3,4, respectively. Additionally, as a reference, we show the similar figures for a normal control. The ROIs in the DMN include the anterior medial prefrontal cortex (aMPFC), the posterior cingulate cortex/precuneus (PCC), the left lateral parietal cortex (L.LatP), the right lateral parietal cortex (R.LatP). The details about these 4 ROIs are listed in the supplementary material 2, and the brain network template of the DMN is provided in the supplementary material 3.

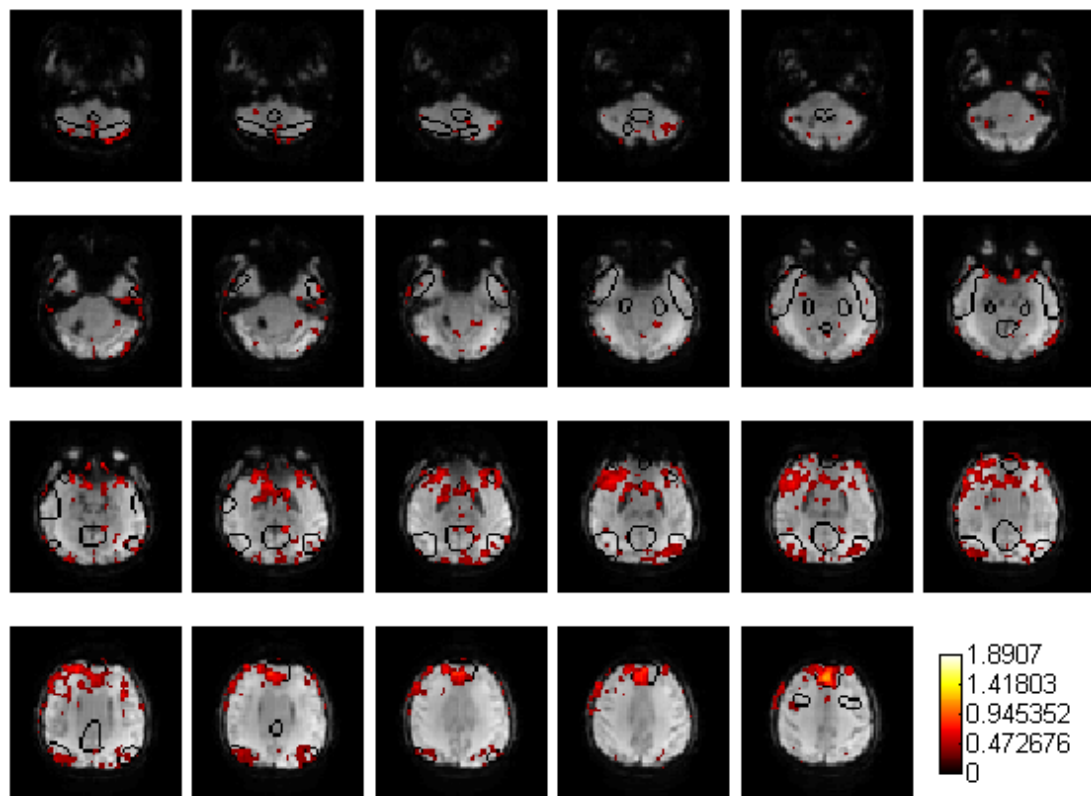
(1) "Beijing_750" dataset, patient alias='056', diagnosis = VS/UWS, GOS score=2

- The transformed 4 ROIs and brain network template of DMN. In this figure, the red regions represent the 4 ROIs warped to the patient's fMRI space, whereas the black contours within the brain outline the key brain regions for the warped brain network template of the DMN. Notably, the black contours were only for illumination, and they were obtained above the threshold 10 of the warped brain network template.

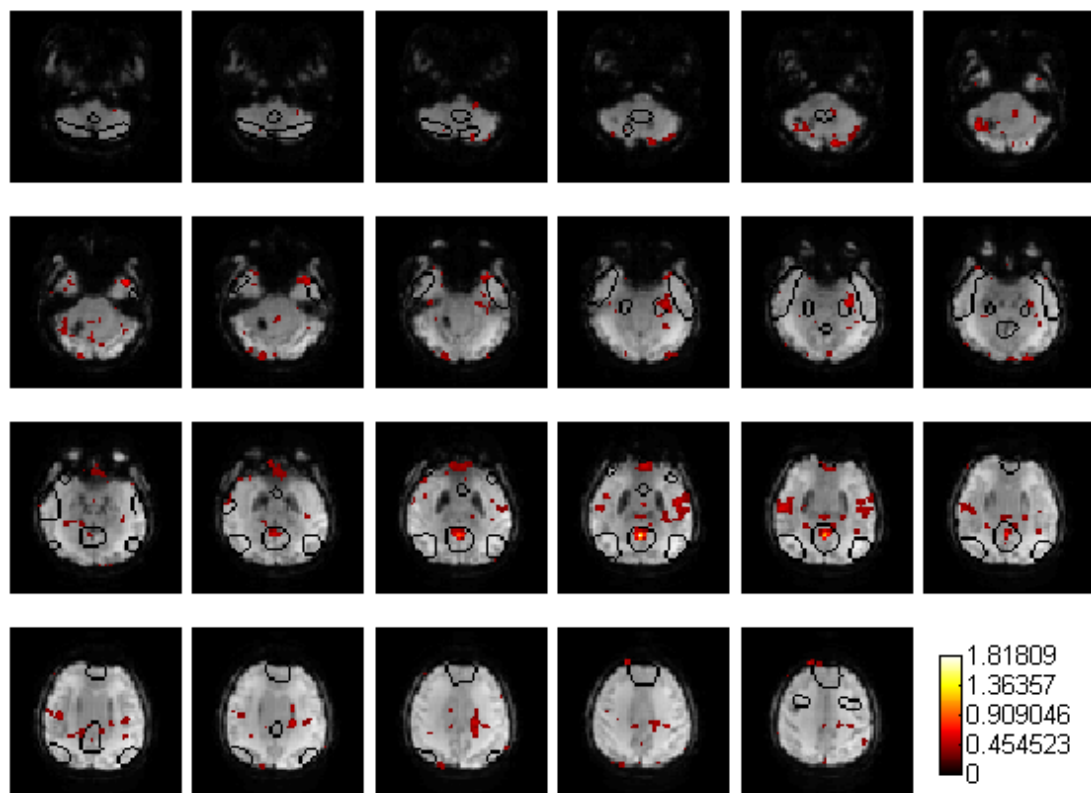


- The functional connectivity Z maps using the warped ROI. The bar in each figure represents the Z value of functional connectivity map of the corresponding ROI across the whole brain.

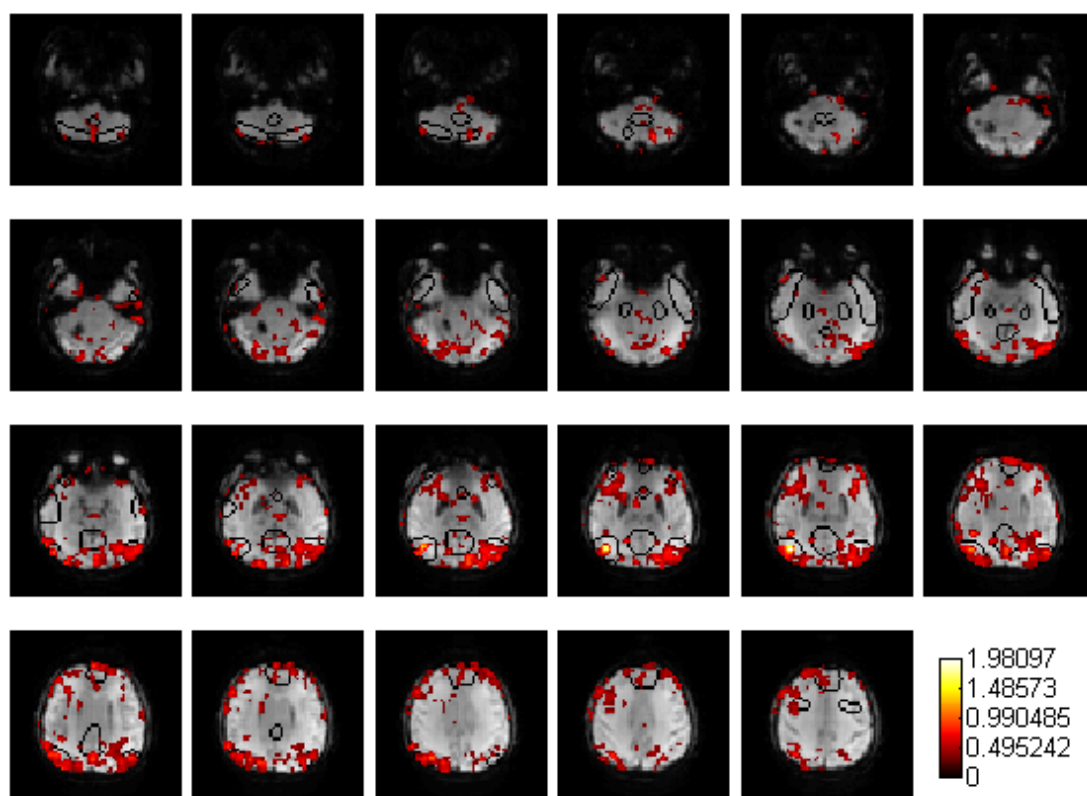
aMPFC:



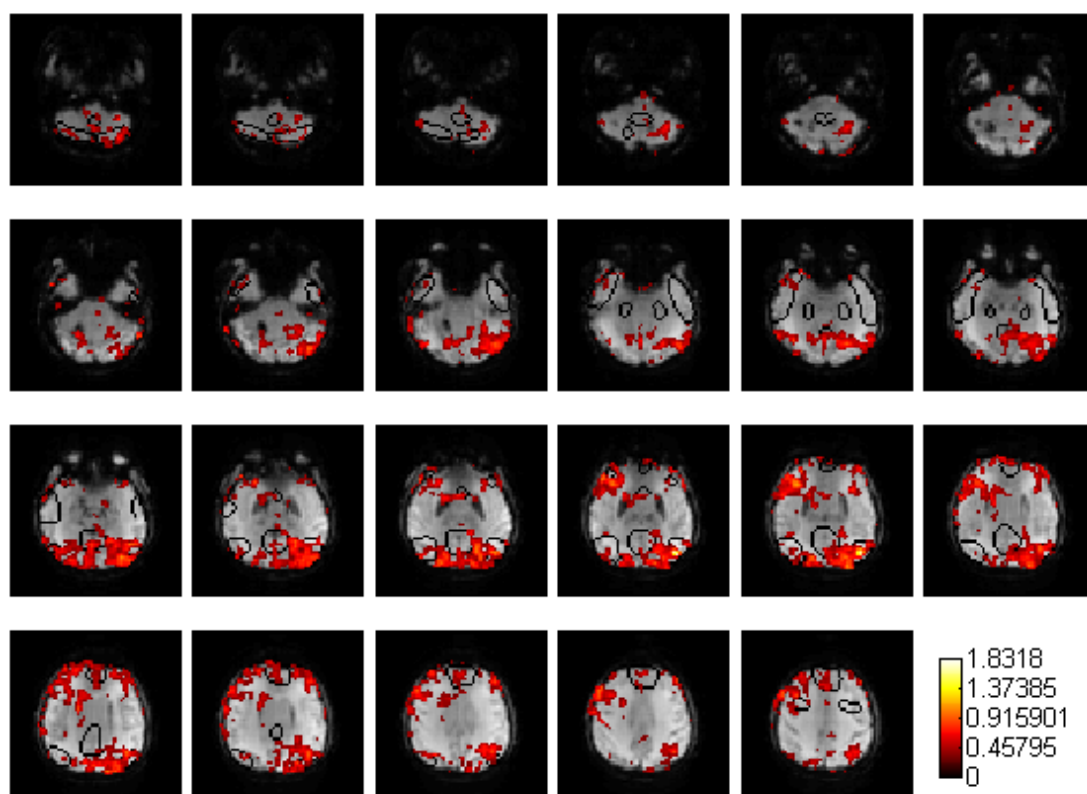
PCC:



L.LatP:

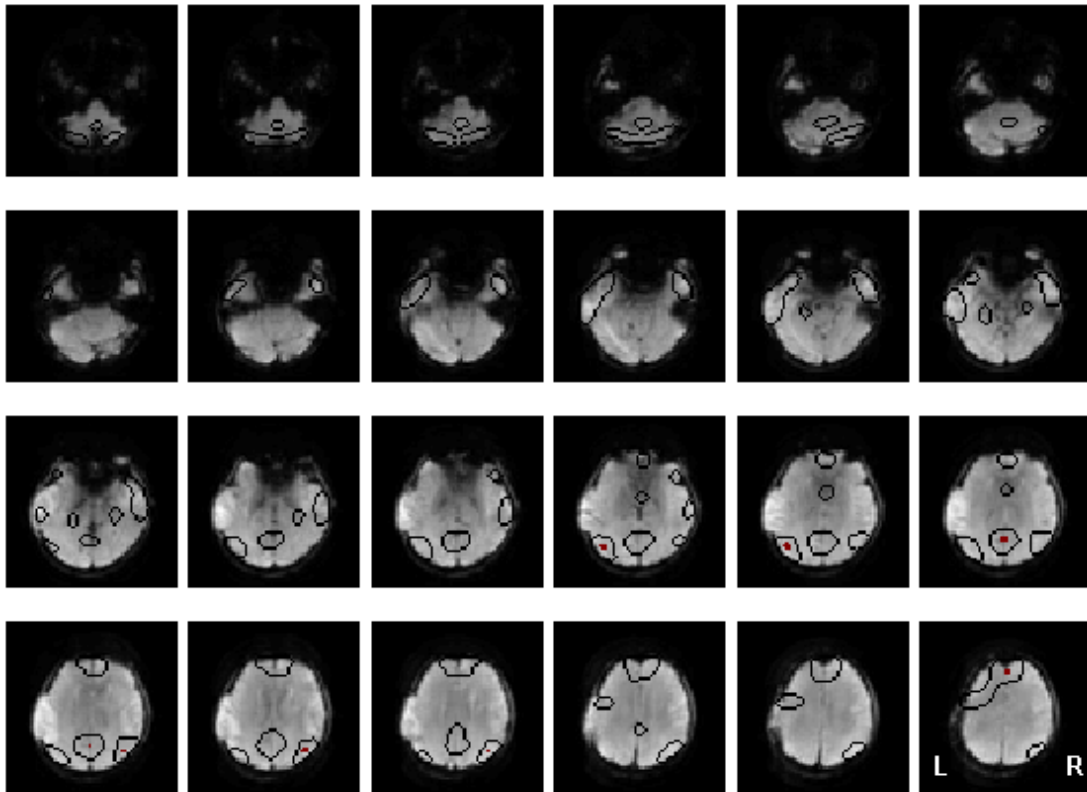


R.LatP:



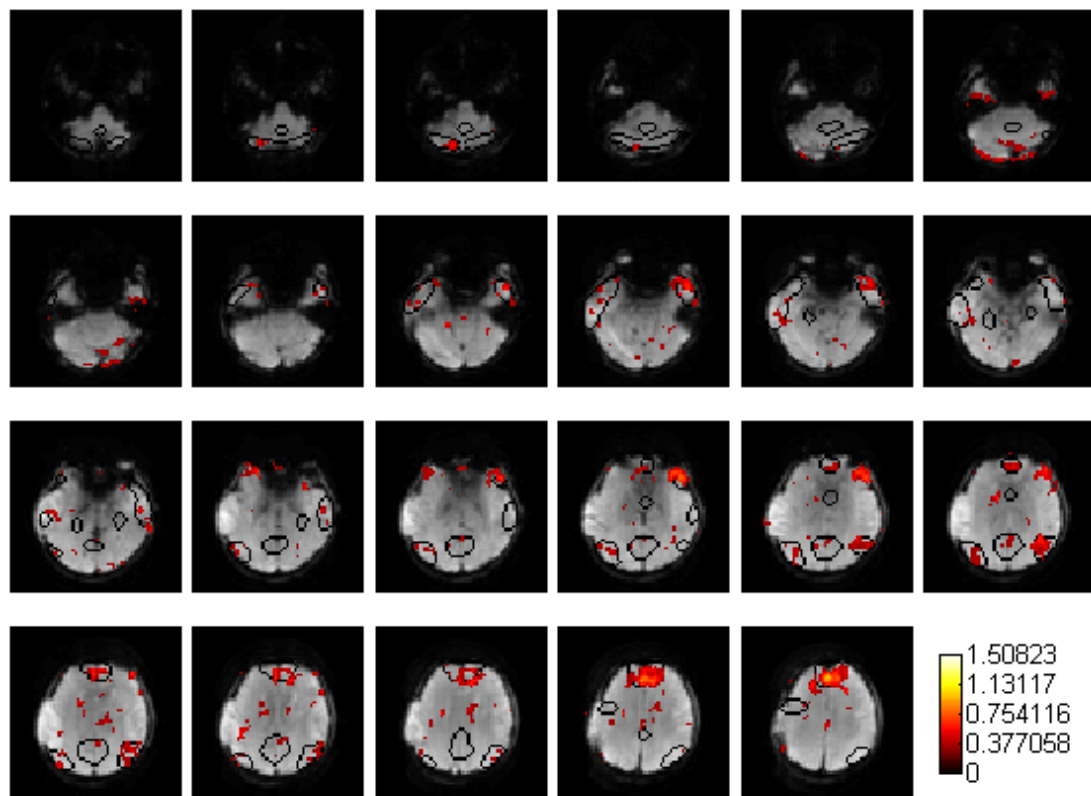
(2) "Beijing_750" dataset, patient alias='013', diagnosis = VS/UWS, GOS score=3

- The transformed 4 ROIs and brain network template of DMN.

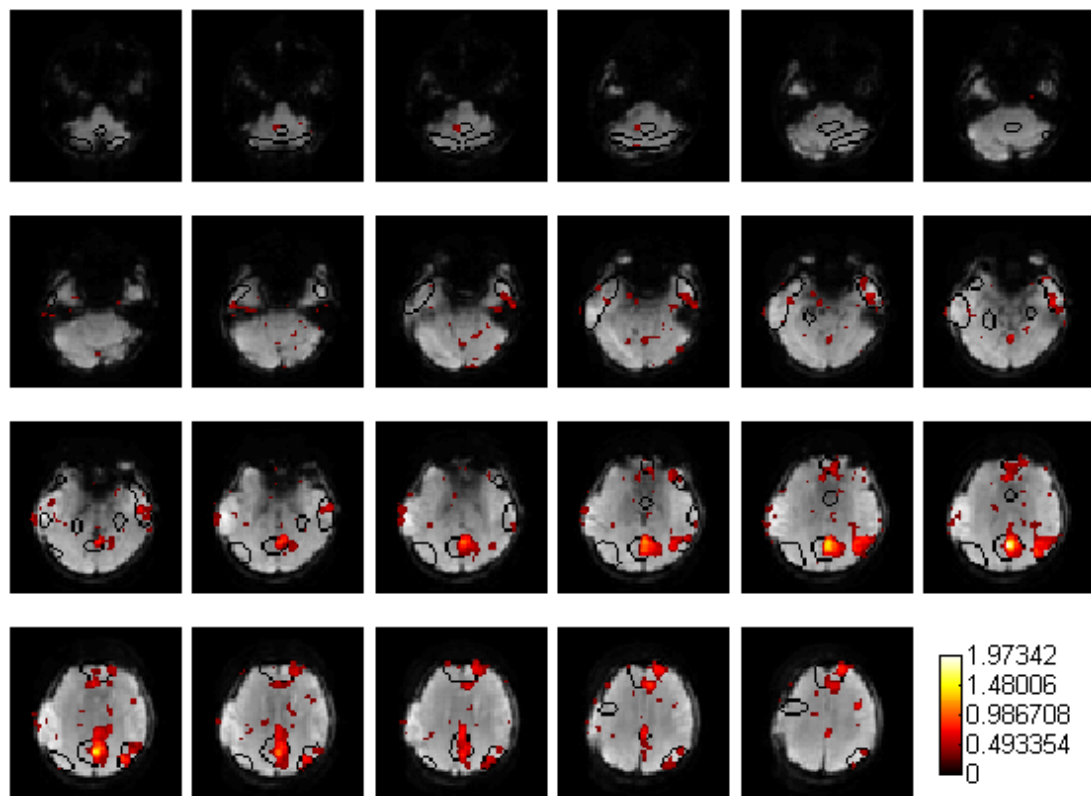


- The functional connectivity Z maps using the warped ROI.

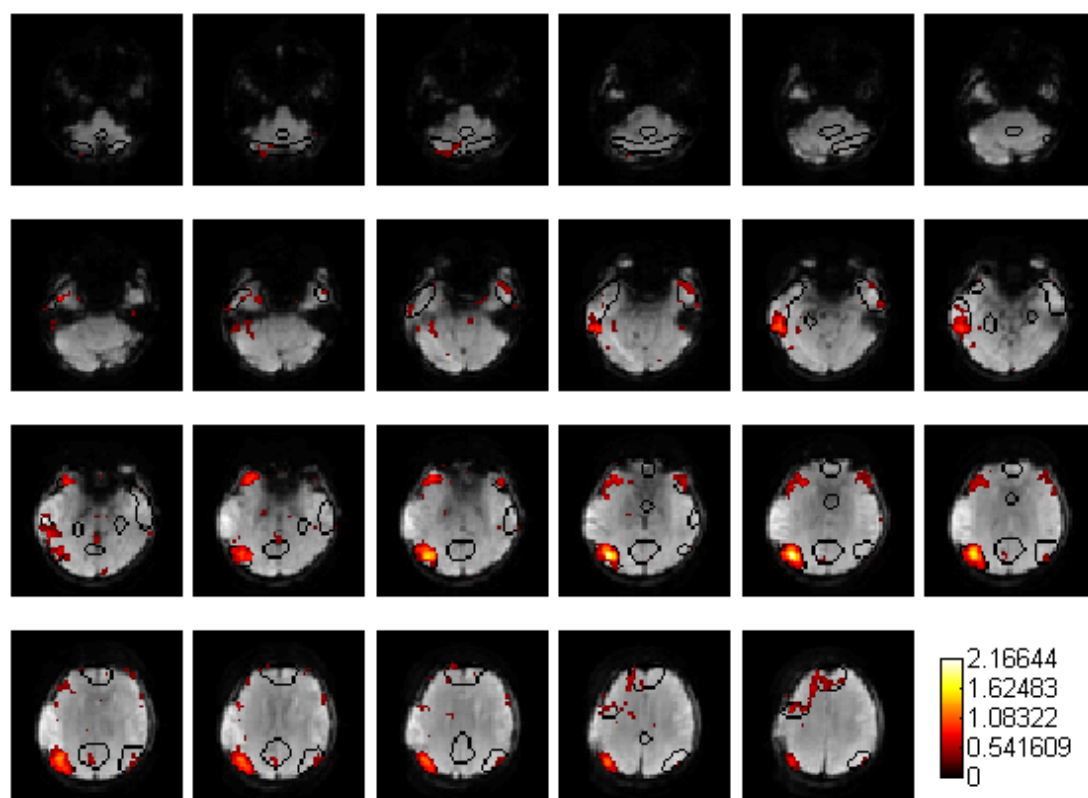
aMPFC:



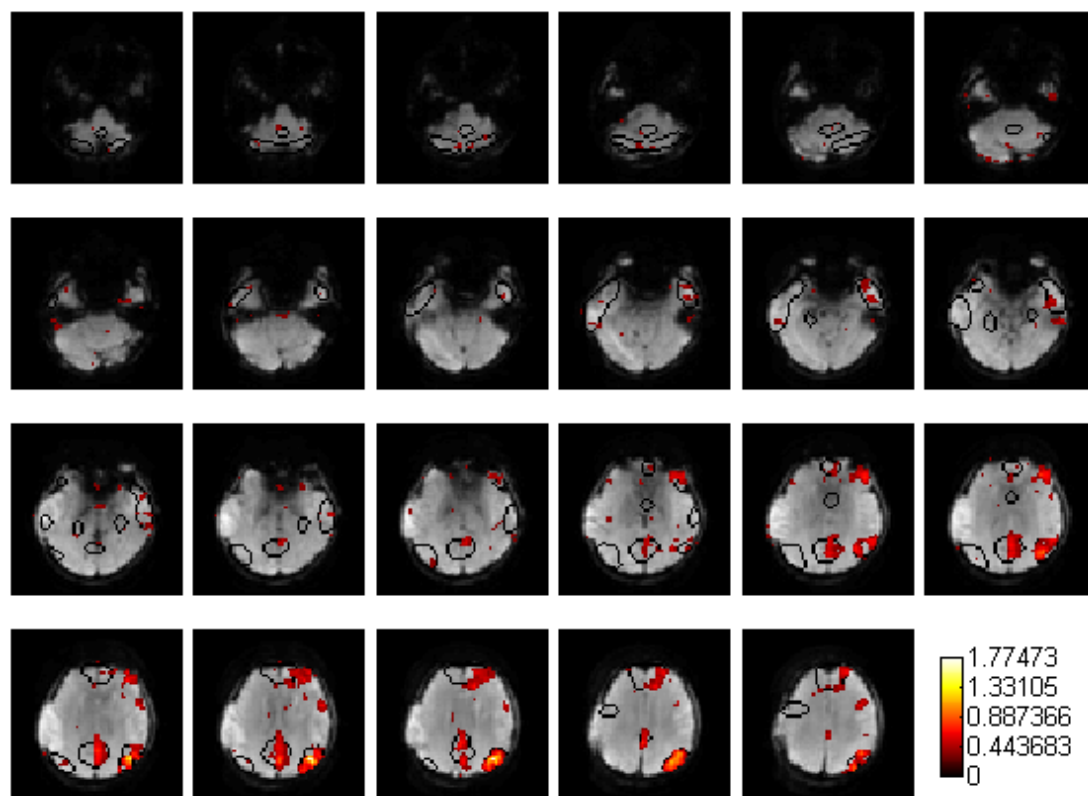
PCC:



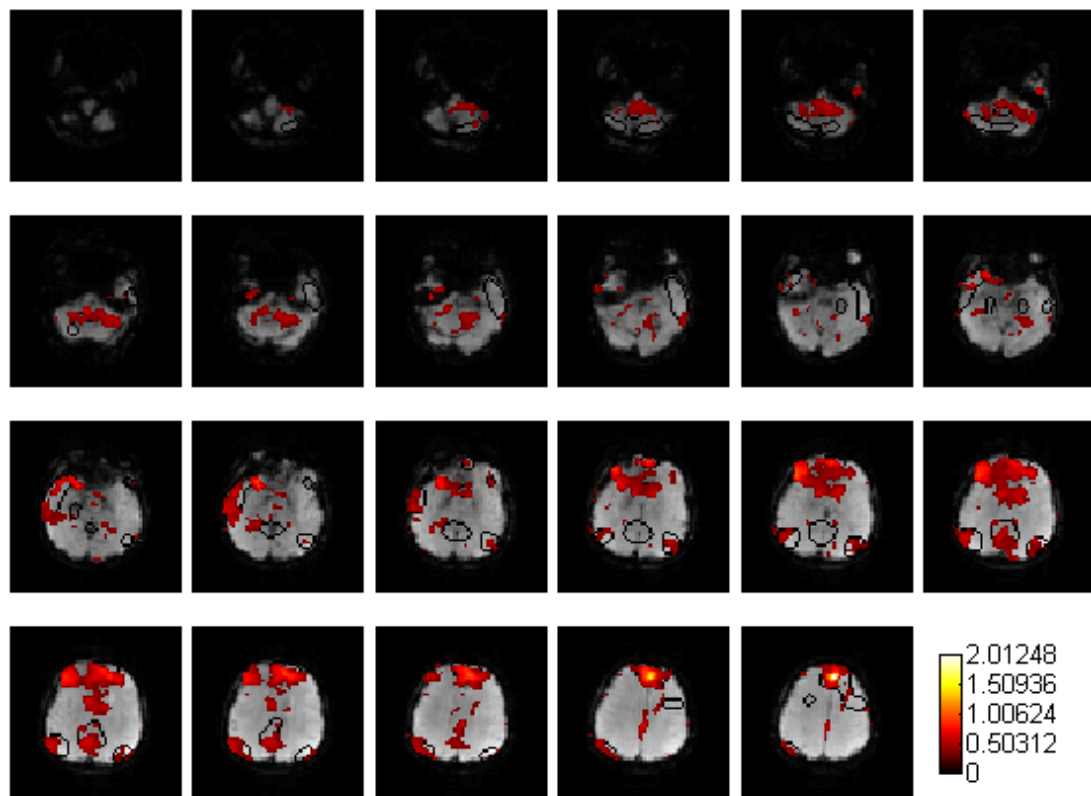
L.LatP:



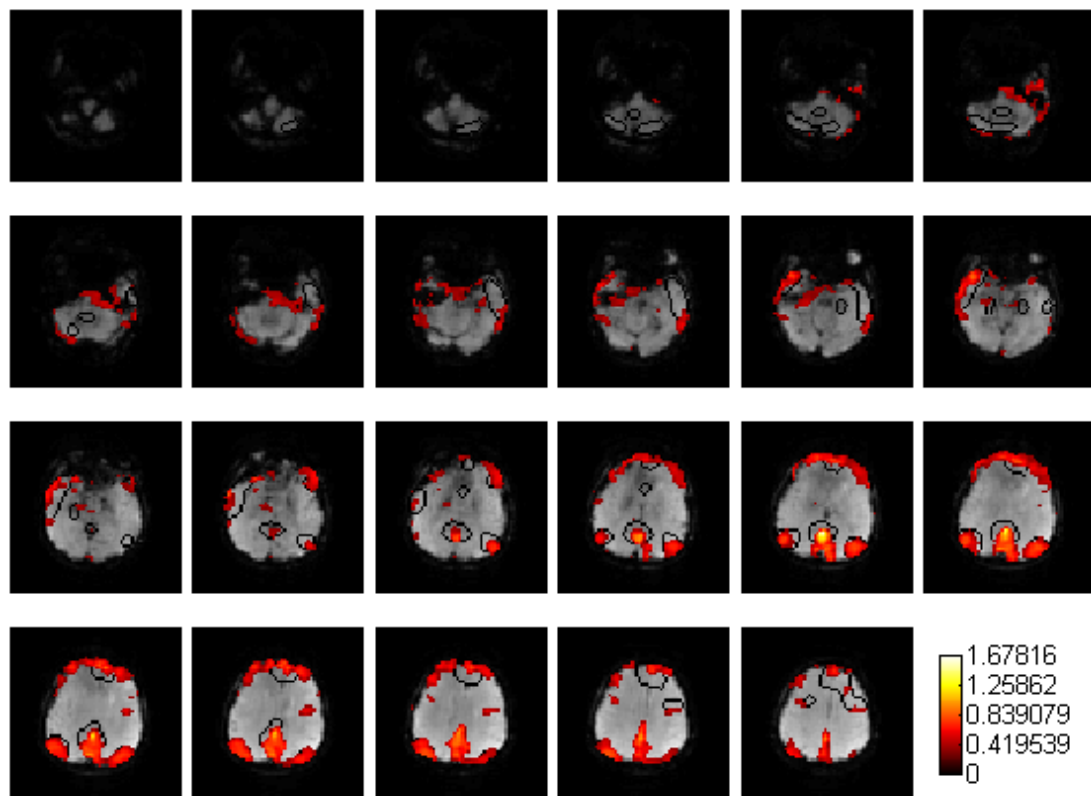
R.LatP:



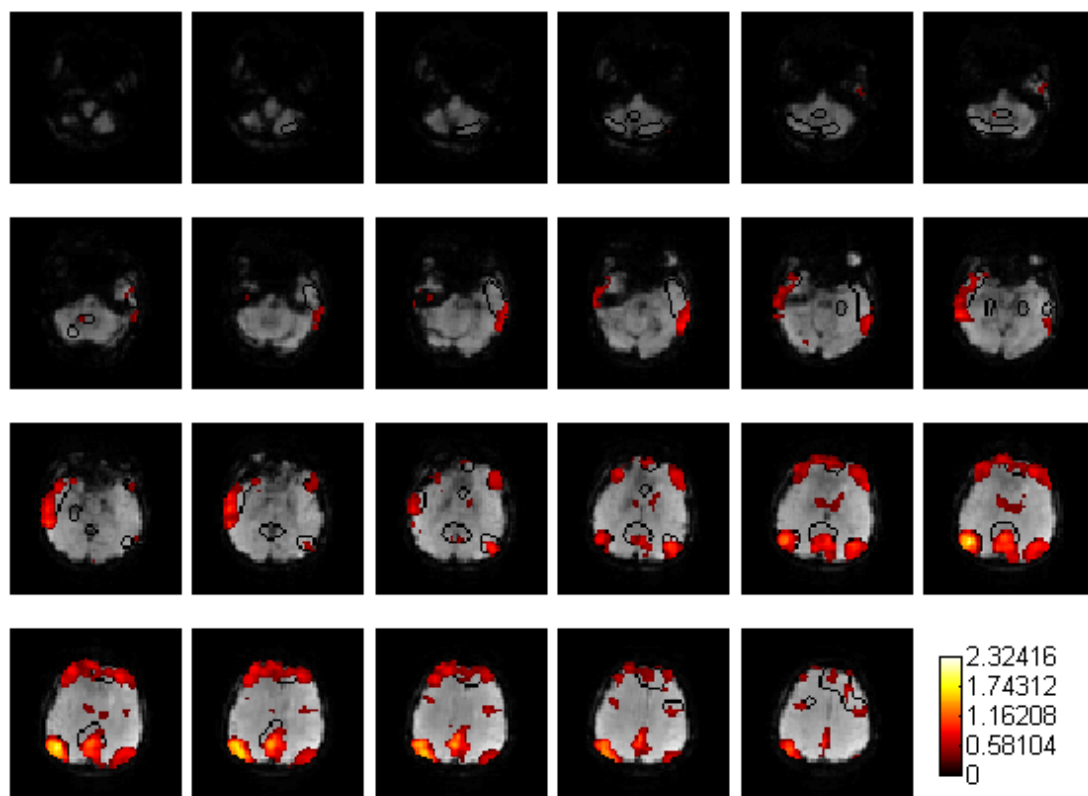
aMPFC:



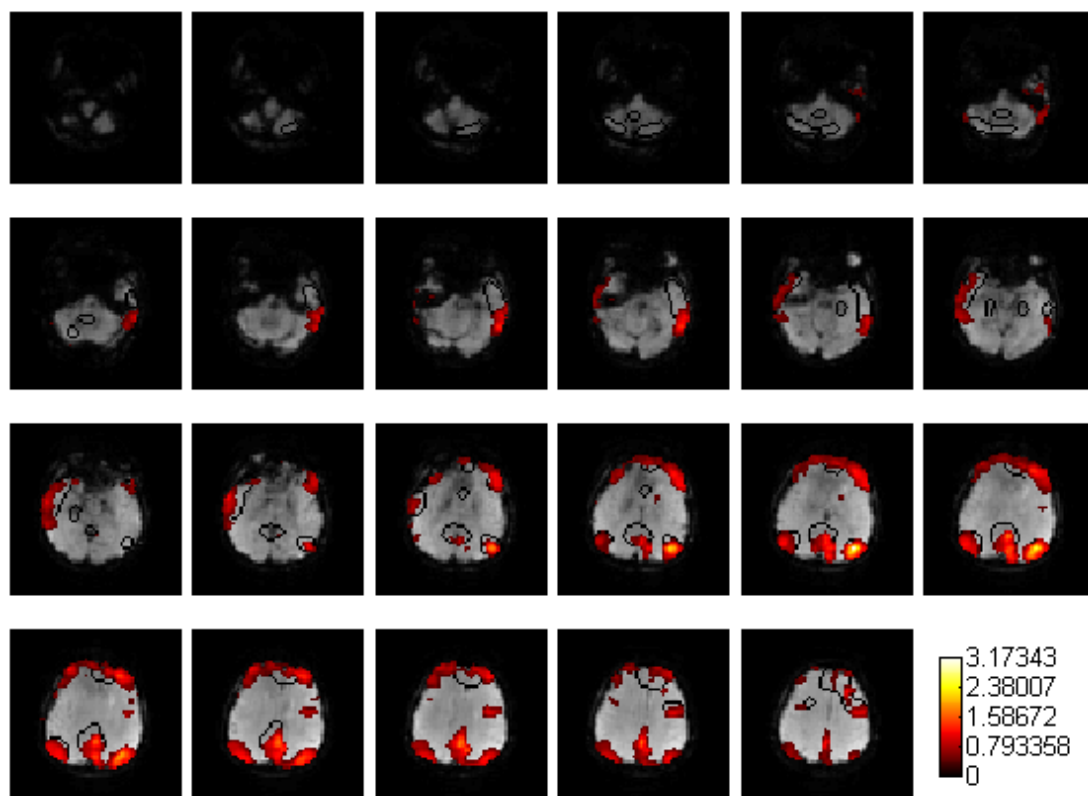
PCC:



L.LatP:

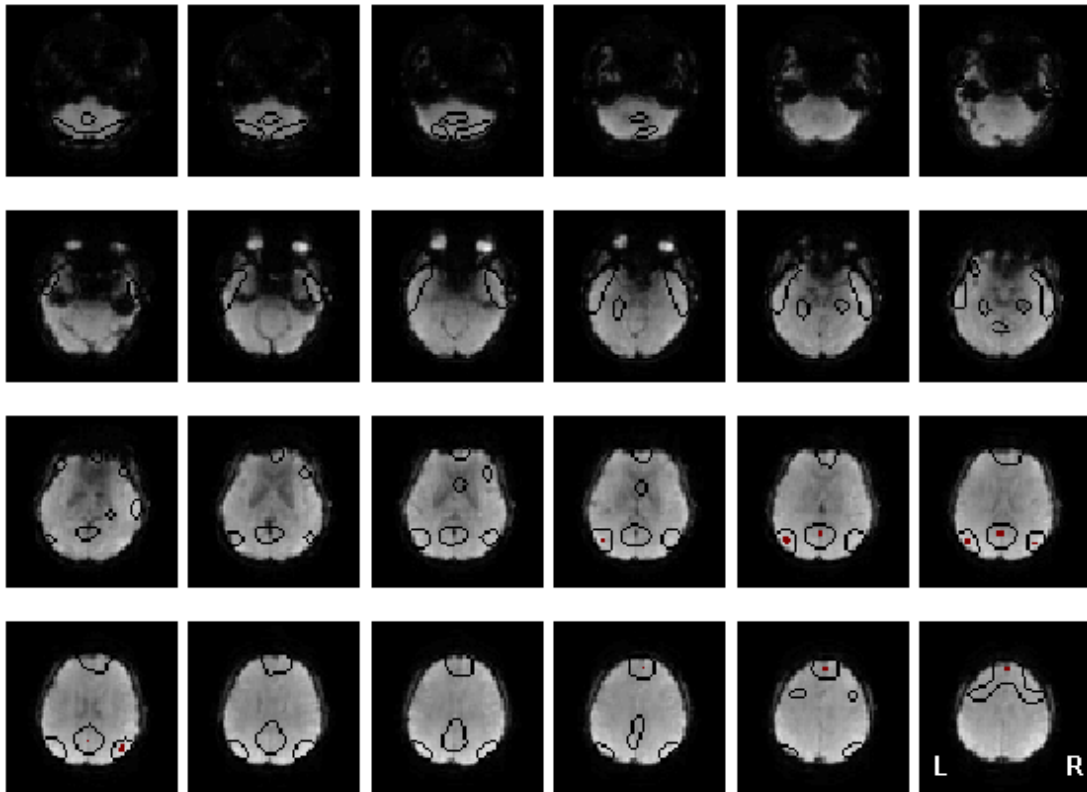


R.LatP:



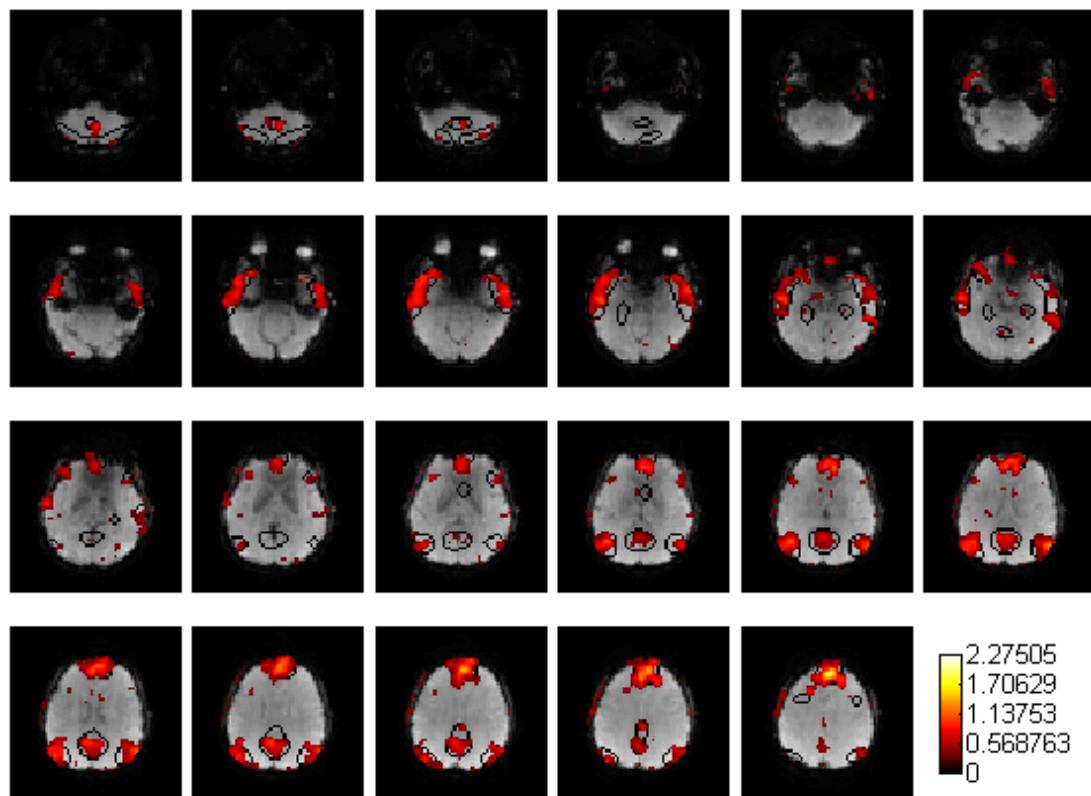
(4) "Beijing_750" dataset, normal control, alias='NC002'

- The transformed 4 ROIs and brain network template of DMN.

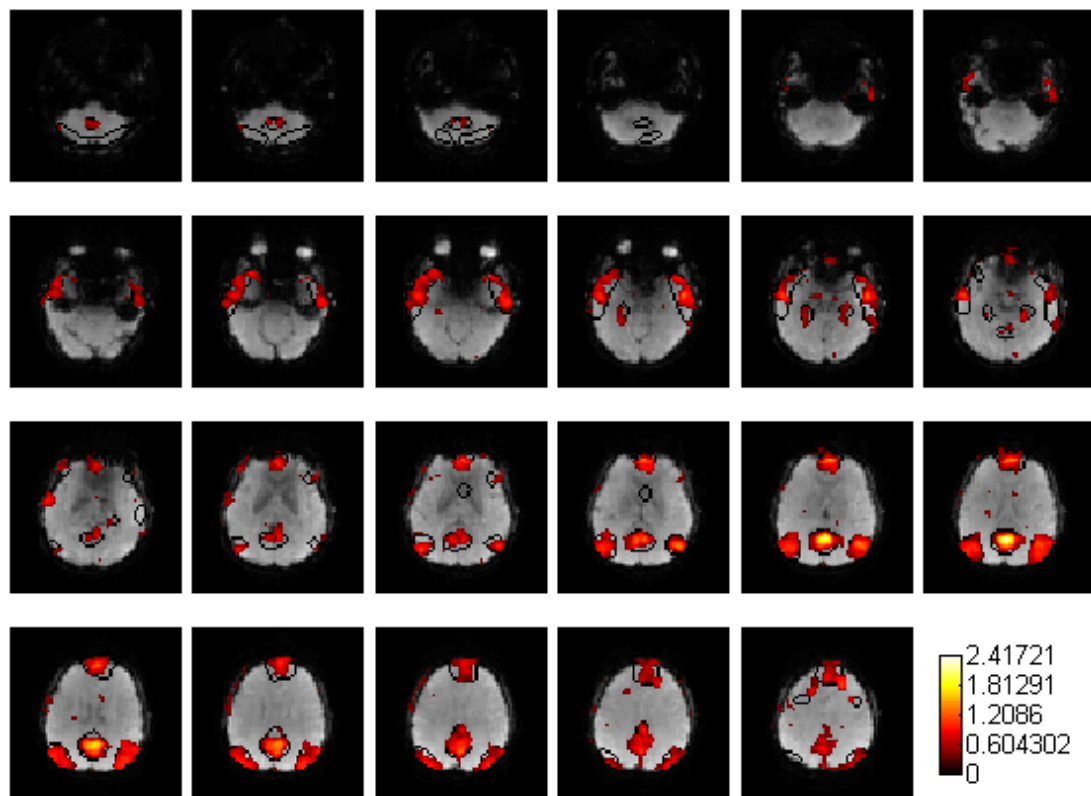


- The functional connectivity Z maps using the warped ROI.

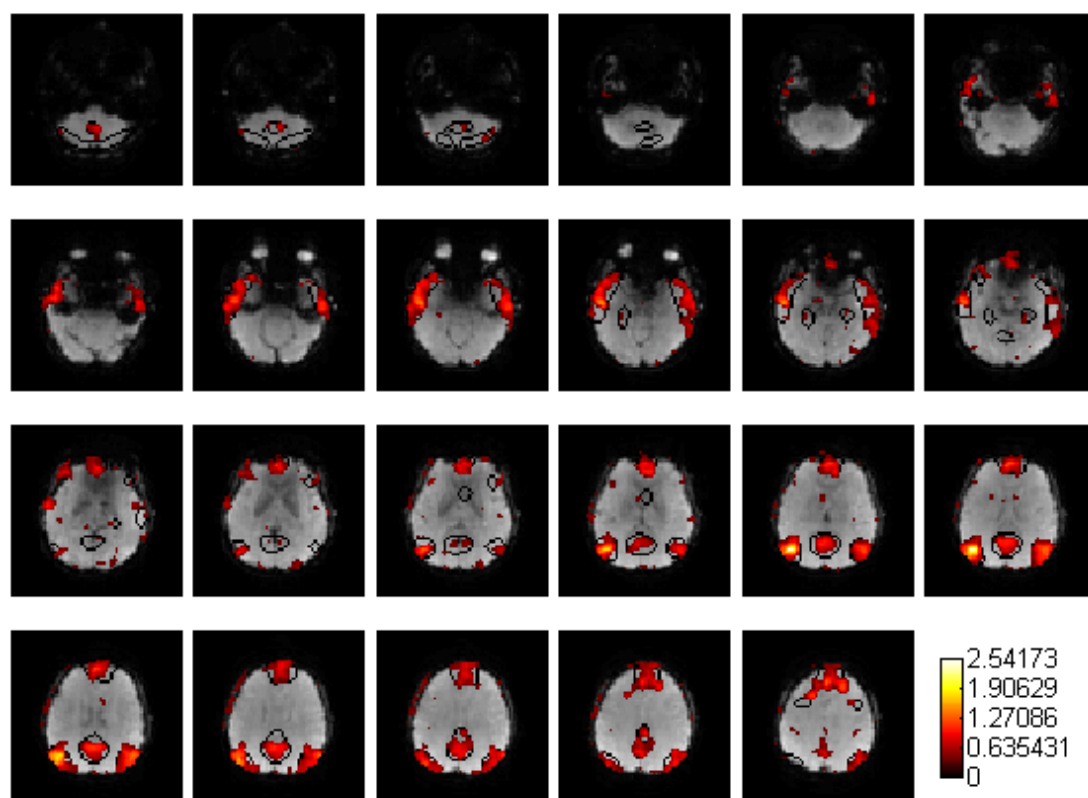
aMPFC:



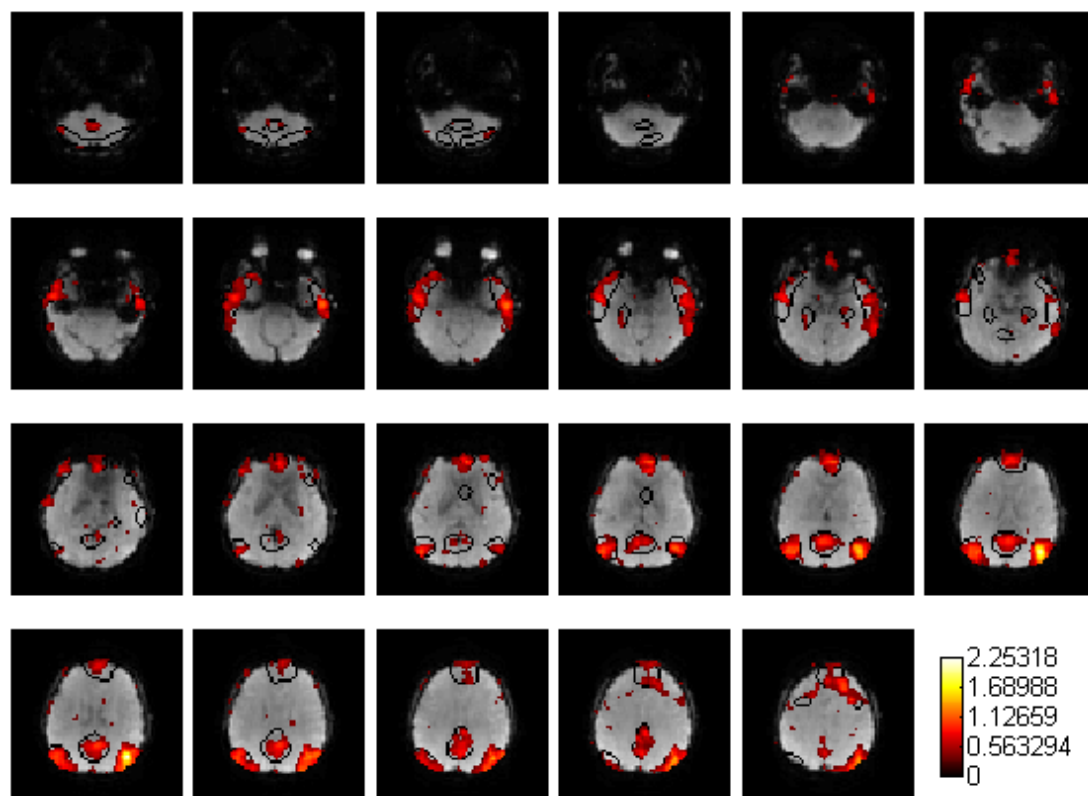
PCC:



L.LatP:



R.LatP:

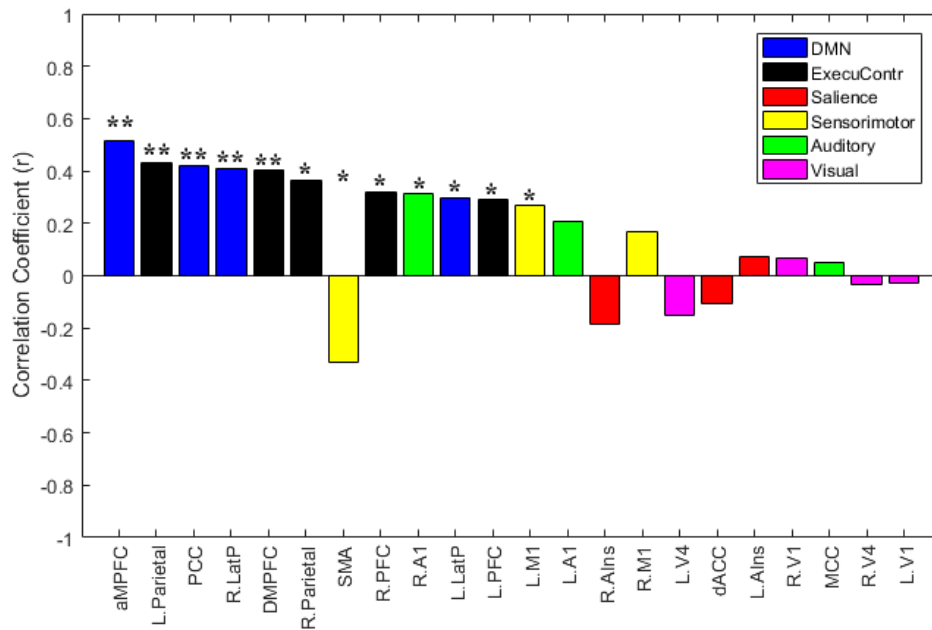


Supplementary Material 6: Correlations between Imaging Features and CRS-R *T1* Scores

(A). The brain area connection features and their Pearson's correlations to the CRS-R scores at the T1 time point across the DOC patients in the training dataset "Beijing 750". Specifically, the brain area connection features are the spatial resemblance between the functional connection patterns of each ROI and the responding brain network templates across the whole brain. The full names of the ROIs are provided in the supplementary material 2.

**₁: $p < 0.05$, FDR corrected; *₁: $p < 0.05$, uncorrected.

	ROI name	Pearson's correlation coefficient and p value
**	DMN.aMPFC	$r = 0.514$, $p = 0.000$
**	ExecuContr.L.Parietal	$r = 0.429$, $p = 0.000$
**	DMN.PCC	$r = 0.420$, $p = 0.001$
**	DMN.R.LatP	$r = 0.407$, $p = 0.001$
**	ExecuContr.DMPFC	$r = 0.405$, $p = 0.001$
*	ExecuContr.R.Parietal	$r = 0.363$, $p = 0.003$
*	Sensorimotor.SMA	$r = -0.332$, $p = 0.008$
*	ExecuContr.R.PFC	$r = 0.320$, $p = 0.011$
*	Auditory.R.A1	$r = 0.315$, $p = 0.012$
*	DMN.L.LatP	$r = 0.298$, $p = 0.018$
*	ExecuContr.L.PFC	$r = 0.291$, $p = 0.021$
*	Sensorimotor.L.M1	$r = 0.267$, $p = 0.035$
	Auditory.L.A1	$r = 0.206$, $p = 0.105$
	Salience.R.AIns	$r = -0.187$, $p = 0.142$
	Sensorimotor.R.M1	$r = 0.167$, $p = 0.191$
	Visual.L.V4	$r = -0.151$, $p = 0.236$
	Salience.dACC	$r = -0.104$, $p = 0.418$
	Salience.L.AIns	$r = 0.075$, $p = 0.560$
	Visual.R.V1	$r = 0.065$, $p = 0.611$
	Auditory.MCC	$r = 0.053$, $p = 0.682$
	Visual.R.V4	$r = -0.031$, $p = 0.809$
	Visual.L.V1	$r = -0.028$, $p = 0.830$

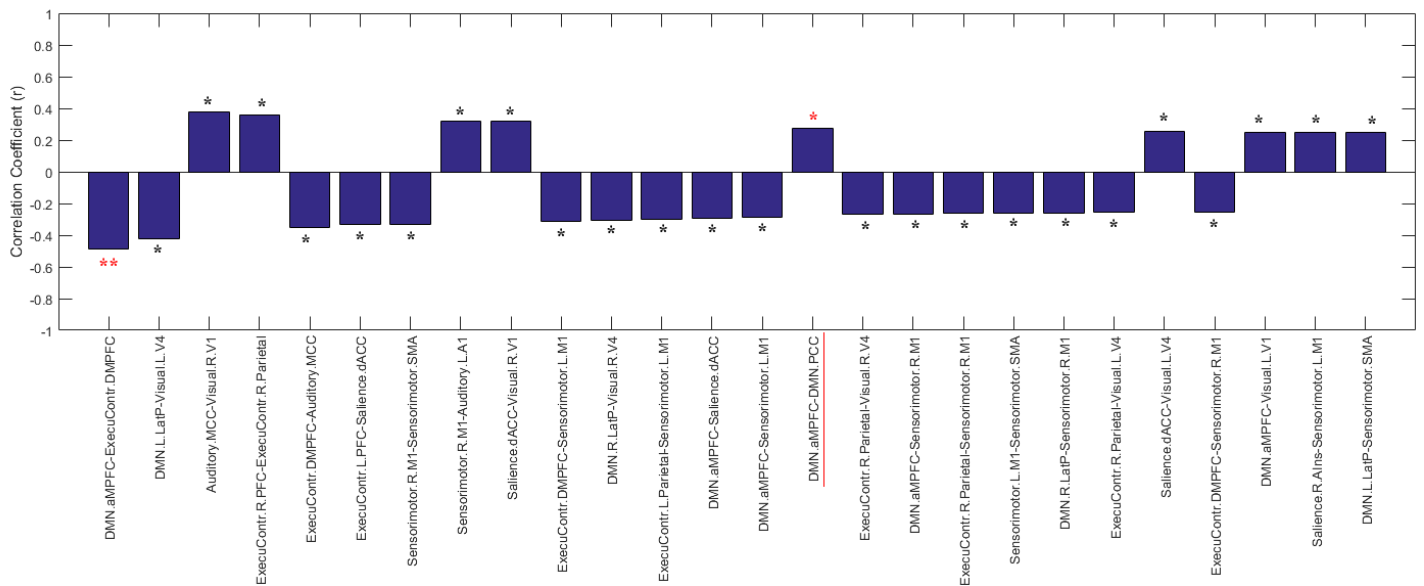


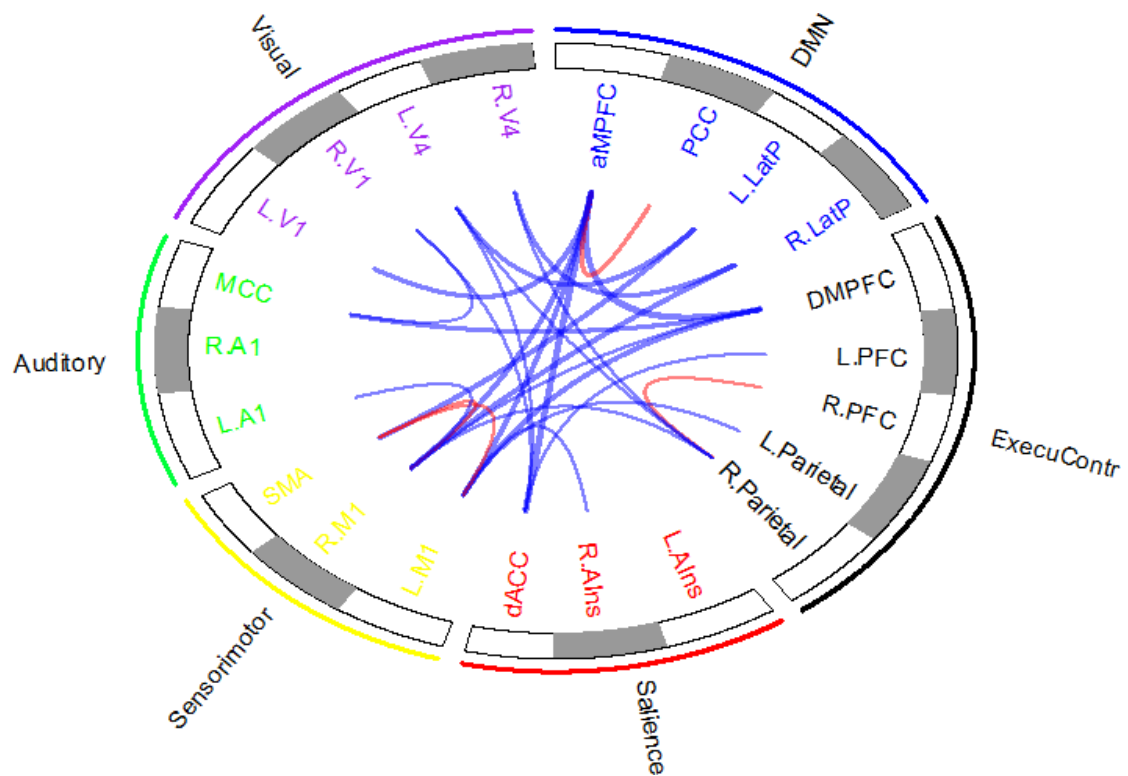
(B). The functional connectivity features and their Pearson's correlations to the CRS-R scores at the T1 time point across the DOC patients in the training dataset "Beijing 750". Specifically, the functional connectivity features are the functional connectivity between any pair of ROIs. Since there were more than 200 functional connectivity, for the space limitations, here just show the functional connectivity features which are significantly correlated to the CRS-R scores at the T1 time point.

** : $p < 0.05$, FDR corrected; * : $p < 0.05$, uncorrected.

	Functional connectivity	Pearson's correlation coefficient and p value
**	DMN.aMPFC - ExecuContr.DMPFC	$r = -0.489$, $p = 0.000$
*	DMN.L.LatP - Visual.L.V4	$r = -0.421$, $p = 0.001$
*	Auditory.MCC - Visual.R.V1	$r = 0.375$, $p = 0.002$
*	ExecuContr.R.PFC - ExecuContr.R.Parietal	$r = 0.361$, $p = 0.004$
*	ExecuContr.DMPFC - Auditory.MCC	$r = -0.351$, $p = 0.005$
*	ExecuContr.L.PFC - Saliency.dACC	$r = -0.335$, $p = 0.007$
*	Sensorimotor.R.M1 - Sensorimotor.SMA	$r = -0.330$, $p = 0.008$
*	Sensorimotor.R.M1 - Auditory.L.A1	$r = 0.319$, $p = 0.011$
*	Saliency.dACC - Visual.R.V1	$r = 0.319$, $p = 0.011$

*	ExecuContr.DMPFC - Sensorimotor.L.M1	$r = -0.310, p = 0.013$
*	DMN.R.LatP - Visual.R.V4	$r = -0.306, p = 0.015$
*	ExecuContr.L.Parietal - Sensorimotor.L.M1	$r = -0.302, p = 0.016$
*	DMN.aMPFC - Salience.dACC	$r = -0.292, p = 0.020$
*	DMN.aMPFC - Sensorimotor.L.M1	$r = -0.286, p = 0.023$
*	DMN.aMPFC - DMN.PCC	$r = 0.275, p = 0.029$
*	ExecuContr.R.Parietal - Visual.R.V4	$r = -0.270, p = 0.033$
*	DMN.aMPFC - Sensorimotor.R.M1	$r = -0.268, p = 0.034$
*	ExecuContr.R.Parietal - Sensorimotor.R.M1	$r = -0.263, p = 0.037$
*	Sensorimotor.L.M1 - Sensorimotor.SMA	$r = -0.261, p = 0.039$
*	DMN.R.LatP - Sensorimotor.R.M1	$r = -0.261, p = 0.039$
*	ExecuContr.R.Parietal - Visual.L.V4	$r = -0.257, p = 0.042$
*	Salience.dACC - Visual.L.V4	$r = 0.256, p = 0.043$
*	ExecuContr.DMPFC - Sensorimotor.R.M1	$r = -0.255, p = 0.043$
*	DMN.aMPFC - Visual.L.V1	$r = 0.251, p = 0.047$
*	Salience.R.AIns - Sensorimotor.L.M1	$r = 0.250, p = 0.049$
*	DMN.L.LatP - Sensorimotor.SMA	$r = 0.248, p = 0.050$



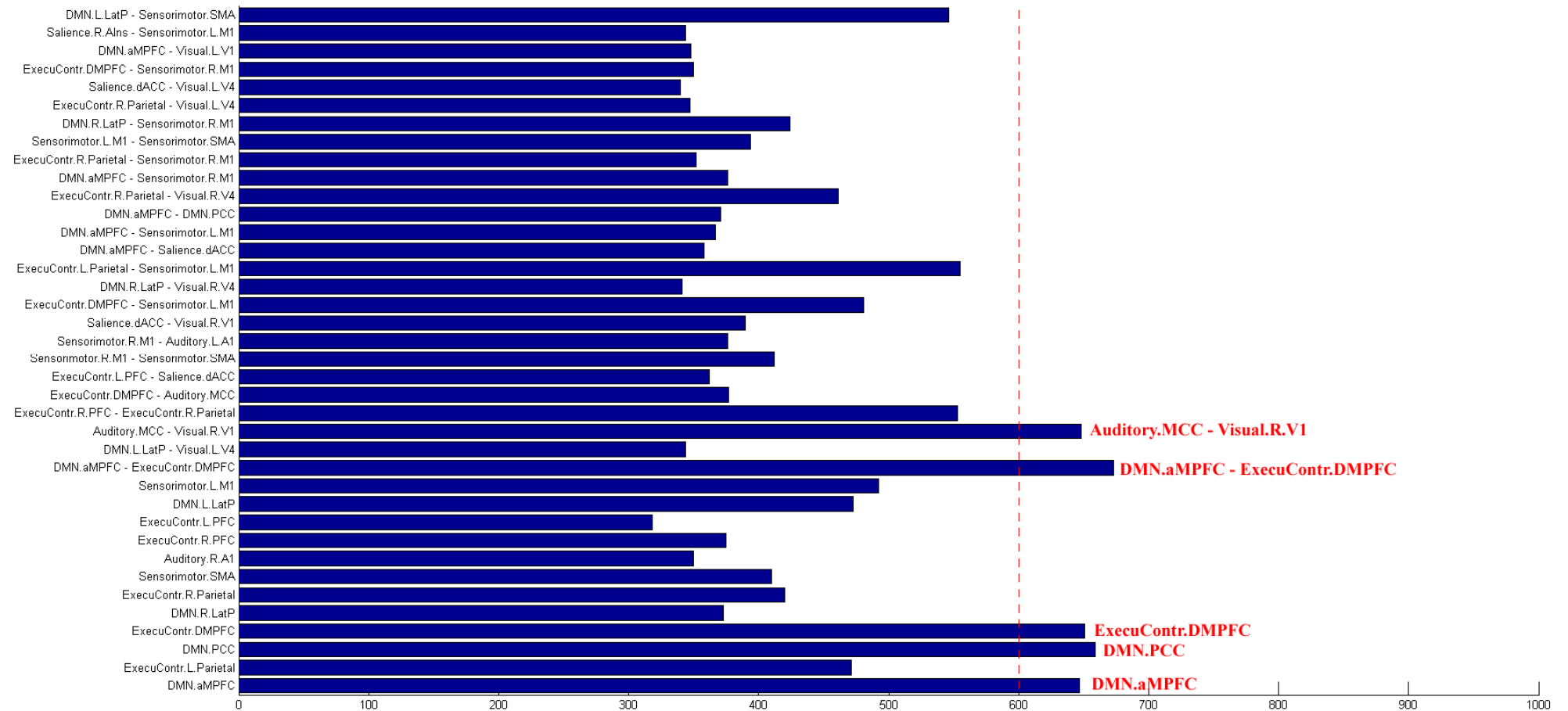


In the above Circos figure, the red links represent the within-network functional connectivity, while the blue links represent the inter-network functional connectivity. The width of link is proportional to the strength of functional connectivity.

Supplementary Material 7: Bootstrap for Imaging Feature Selection

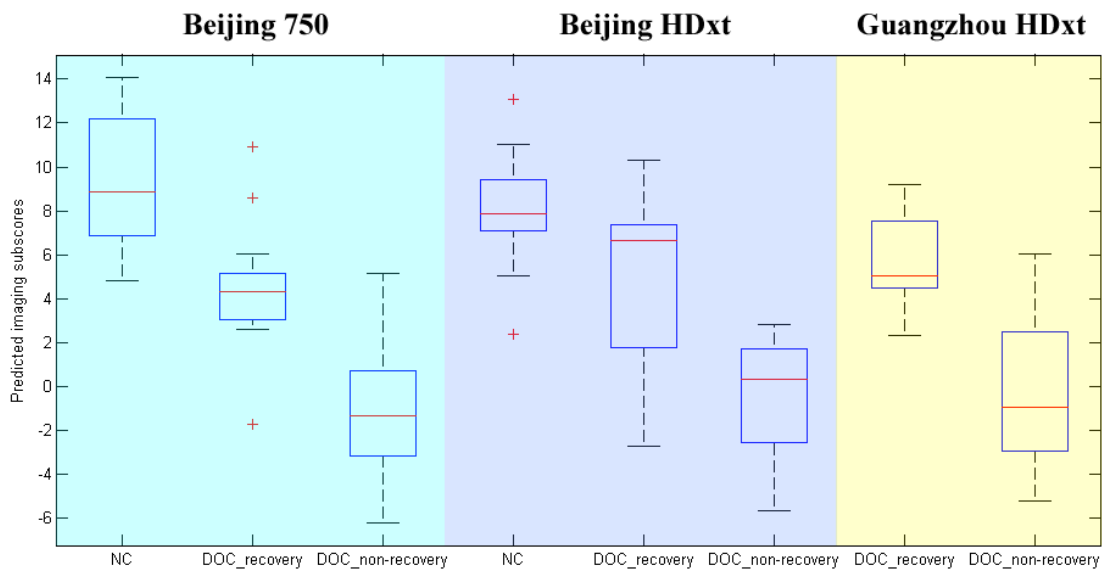
Histogram depicting the imaging features included in prognostic models. The horizontal bar represents the number selected in the 1000 bootstrap

CARS-PLSR models.



Supplementary Material 8: Normal Control Validations

To test robustness, we evaluated whether the prognostic regression model generalized to the normal controls (NC) in the training dataset "Beijing 750" ($n = 30$) and the testing dataset "Beijing HDxt" ($n=10$). No normal control data was available in the Guangzhou centre. Since the NC subjects did not have the clinical characteristics, we calculated the subscores only using the imaging features and then compared the subscores to that of the DOC patients. The following figure showed the imaging subscores for all of the subjects in the three datasets. We would like to emphasize that the normal controls in the training dataset were only used to establish the brain network templates, and not used for any training.



We found that (1) in the training dataset "Beijing 750", the NC subjects had significantly larger imaging subscores in comparison to both the DOC patients with consciousness recovery and the DOC patients with consciousness non-recovery (one-way ANOVA, $p < 0.05$, multiple comparison corrected), and the DOC patients

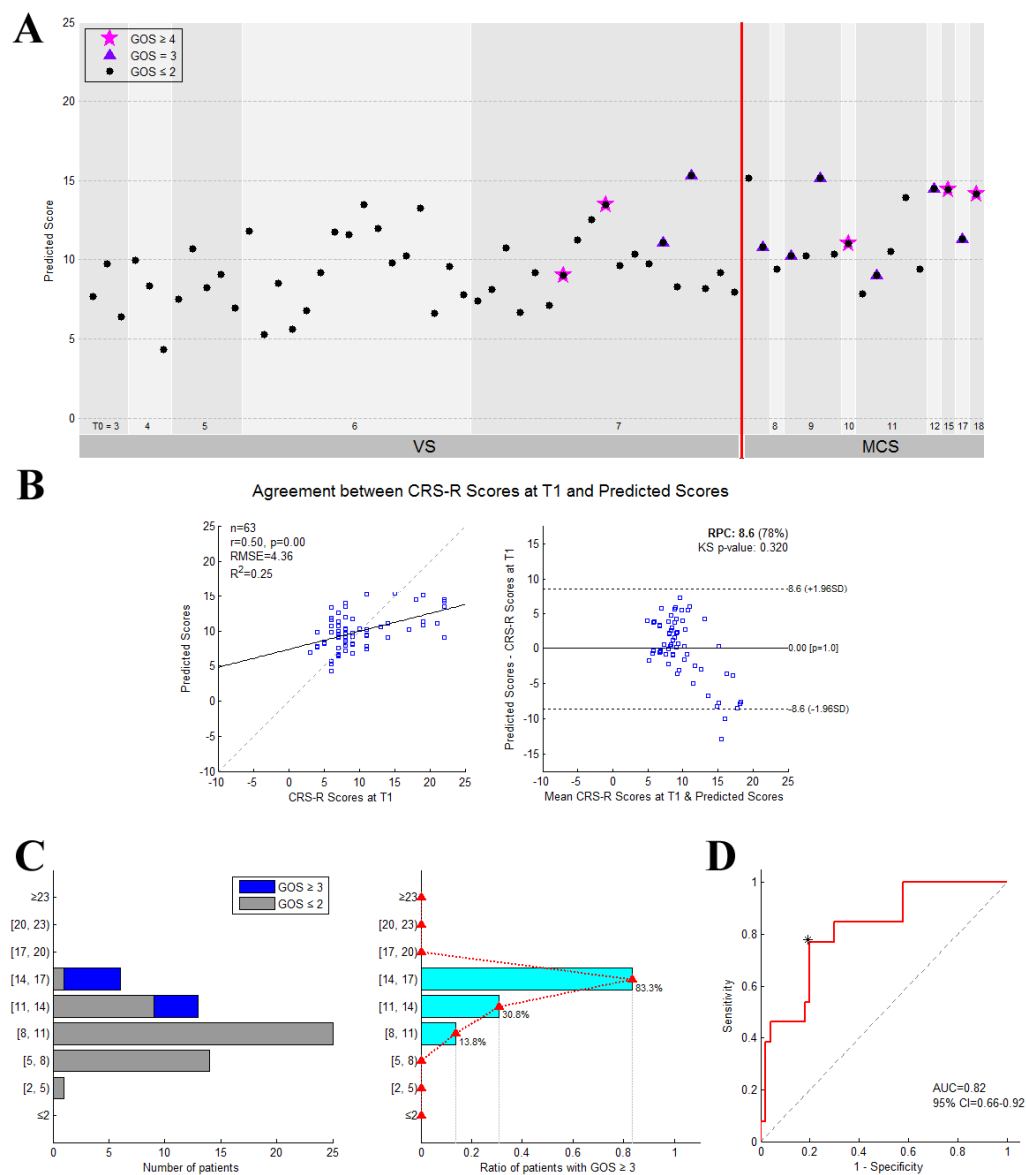
with consciousness recovery had significantly larger imaging subscores in comparison to the DOC patients with consciousness non-recovery (one-way ANOVA, $p < 0.05$, multiple comparison corrected); (2) in the testing dataset "Beijing HDxt", the NC subjects had significantly larger imaging subscores in comparison to the DOC patients with consciousness non-recovery (one-way ANOVA, $p < 0.05$, multiple comparison corrected), and the DOC patients with consciousness recovery had significantly larger imaging subscores in comparison to the DOC patients with consciousness non-recovery (one-way ANOVA, $p < 0.05$, multiple comparison corrected); (3) In the testing dataset "Guangzhou HDxt", the imaging subscores of the DOC patients with consciousness recovery were significantly larger than the one of DOC patients with consciousness non-recovery (two-sample t-tests, $p < 0.05$).

Supplementary Material 9: Single Modality Model

(A). The prognostic regression model using only the clinical features.

$$\text{Predicted Score} = 9.921 - 2.143 \times (\text{Incidence_age}) - 0.189 \times (\text{Duration_of_DOC}) + 0.640 \times (\text{Etiology_traumatic}) - 1.346 \times (\text{Etiology_anoxic})$$

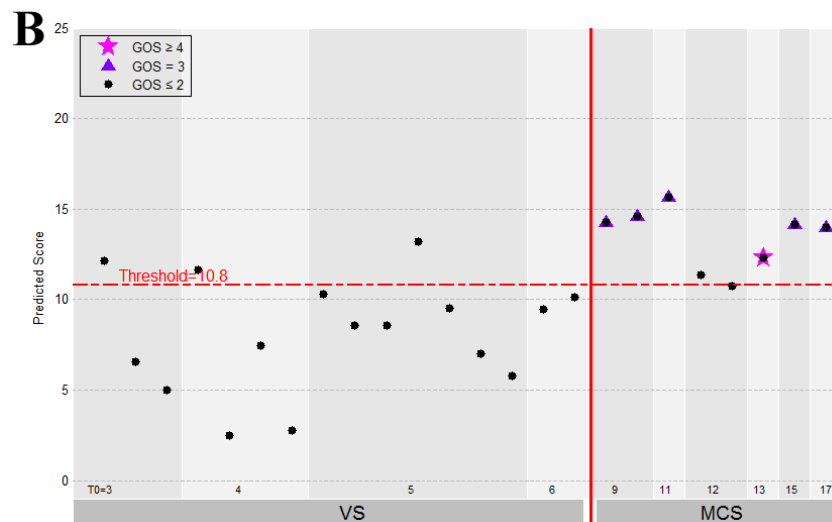
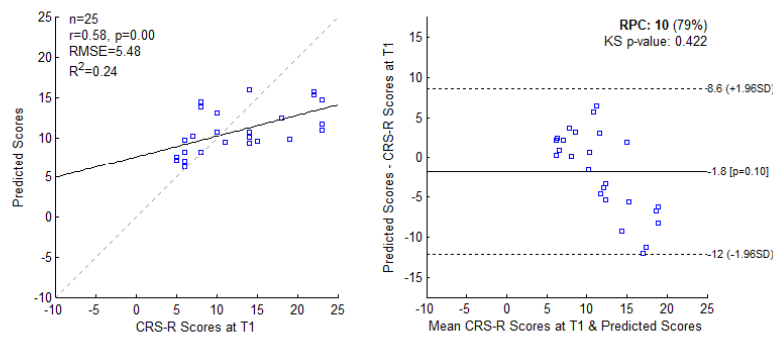
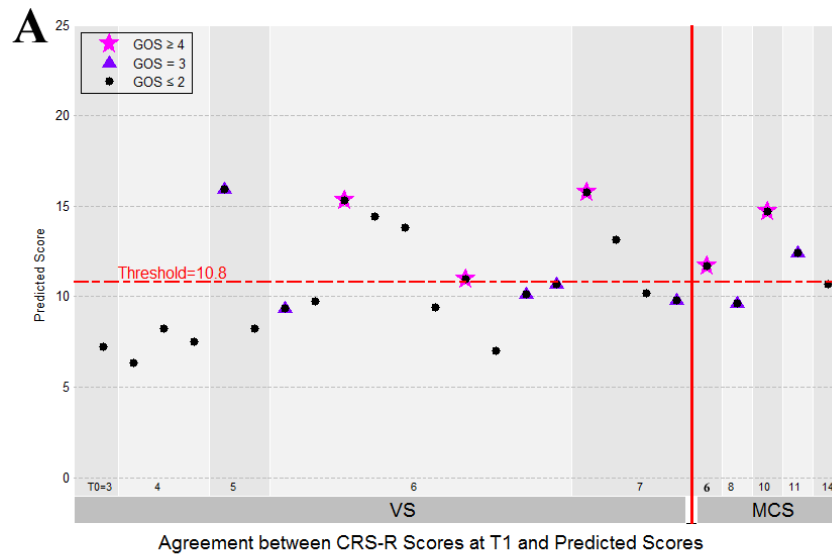
- In the training dataset "Beijing 750", the regression and classification performance were as follows.



The optimum cut-off value was 10.8. Thus, the classification performance in the

training dataset were as follows. $ACC = 0.79$, Sensitivity = 0.78, Specificity = 0.80, PPV = 0.50, NPV = 0.93, F_1 score=0.61.

- In the testing datasets "Beijing HDxt" (subplot A) and the testing dataset "Guangzhou HDxt" (subplot B), the regression and classification performance were as follows.

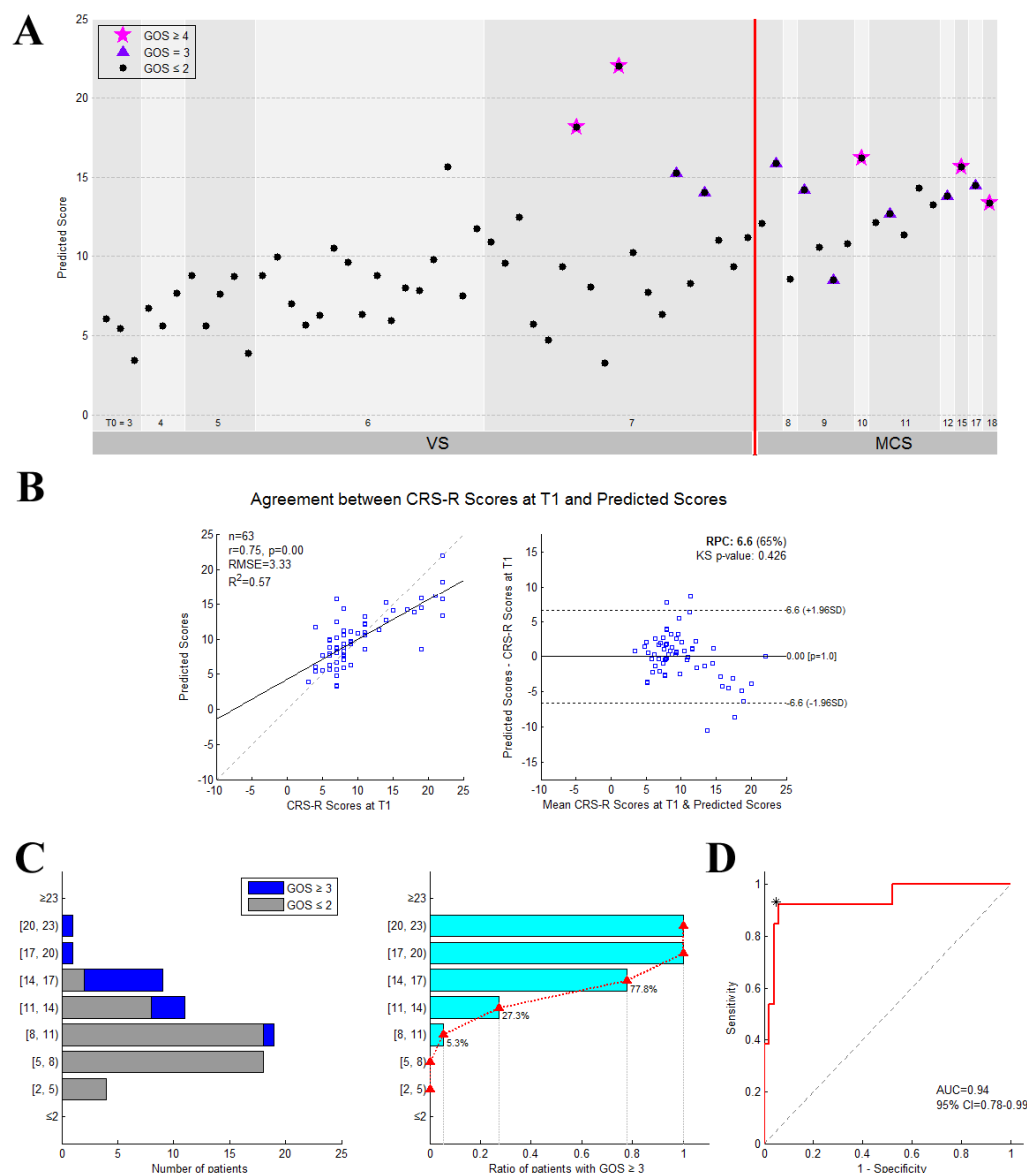


The testing dataset "Beijing HDxt": classification ACC = 0.68, Sensitivity = 0.58, Specificity = 0.77, PPV = 0.70, NPV = 0.67, F_1 score=0.64; The testing dataset "Guangzhou HDxt" classification ACC = 0.83, Sensitivity = 1.00, Specificity = 0.78, PPV = 0.60, NPV = 1.00, F_1 score=0.75.

(B). The prognostic regression model using only the imaging features.

$$\begin{aligned} \text{Predicted Score} = & 9.921 \\ & +1.161 \times (\text{DMN.aMPFC}) + 0.662 \times (\text{DMN.PCC}) + 1.599 \times (\text{ExecuContr.DMPFC}) \\ & -1.915 \times (\text{DMN.aMPFC} - \text{ExecuContr.DMPFC}) \\ & +1.122 \times (\text{Auditory.MCC} - \text{Visual.R.V1}) \end{aligned}$$

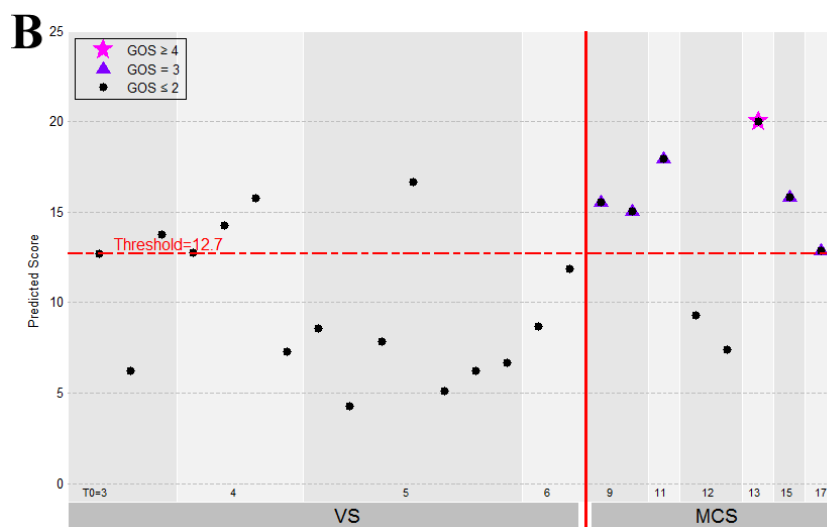
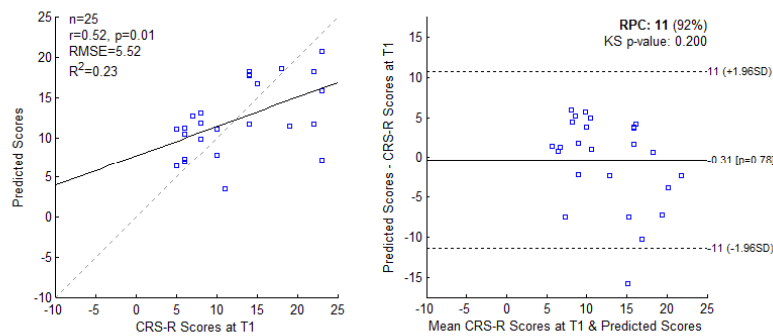
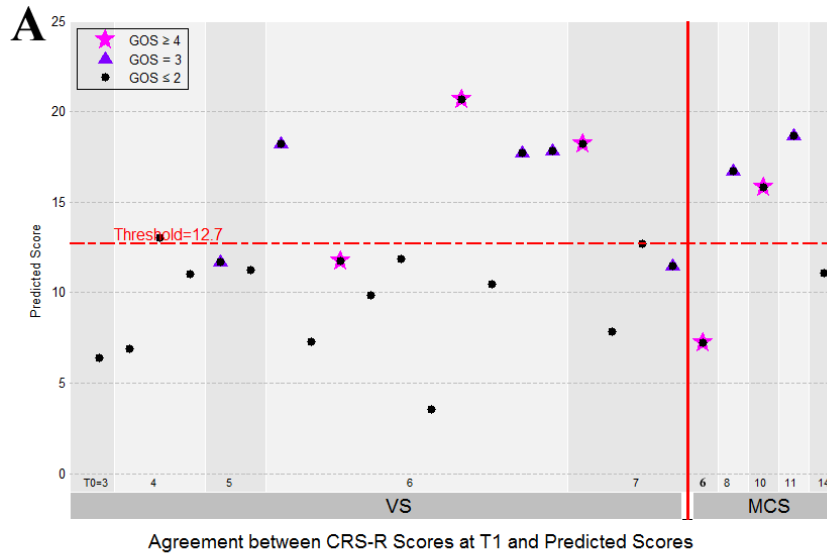
- In the training dataset "Beijing 750", the regression and classification performance were as follows.



The optimum cut-off value was 12.7. Thus, the classification accuracy $ACC = 0.94$,

Sensitivity = 0.92, Specificity = 0.94, PPV = 0.80, NPV = 0.98, F_1 score=0.86.

- In the testing datasets "Beijing HDxt" (subplot A) and the testing dataset "Guangzhou HDxt" (subplot B), the regression and classification performance were as follows.



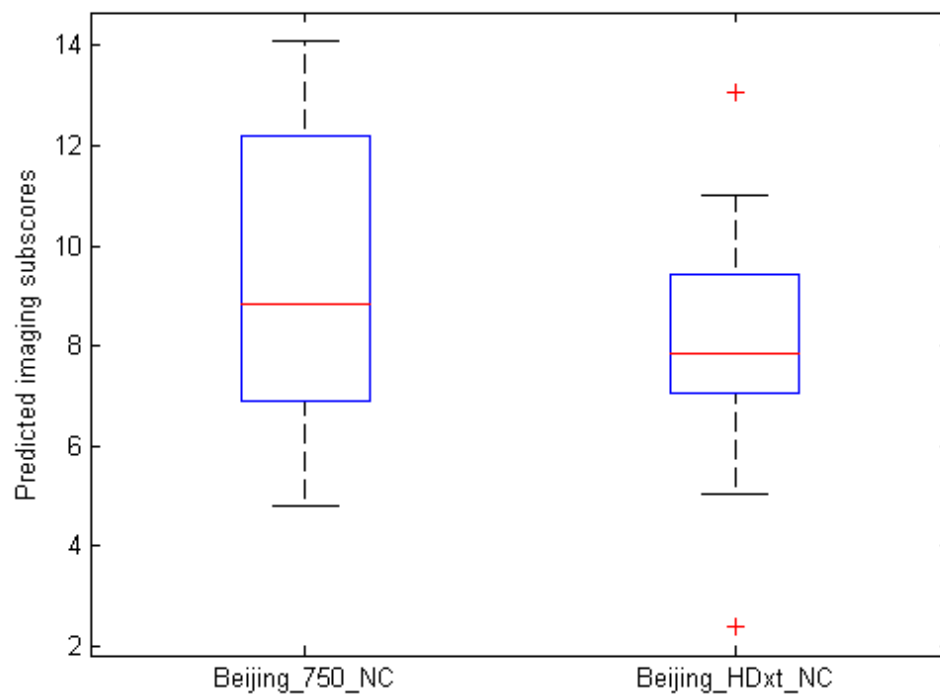
The testing dataset "Beijing HDxt": classification ACC = 0.80, Sensitivity = 0.67, Specificity = 0.92, PPV = 0.89, NPV = 0.75, F_1 score=0.76; The testing dataset

"Guangzhou HDxt" classification ACC = 0.79, Sensitivity = 1.00, Specificity = 0.72,
PPV = 0.55, NPV = 1.00, F_1 score=0.71.

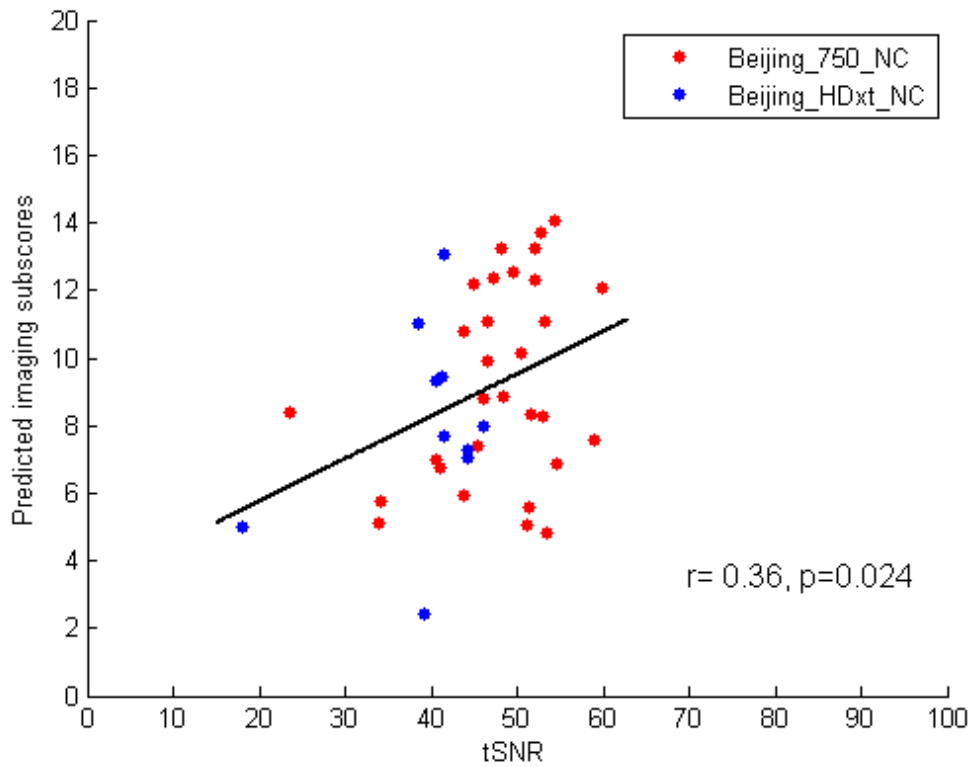
Supplementary Material 10: Variations across different sites

To investigate variations across different sites, we did two experiments using the normal control (NC) subjects in this study.

First, we explored whether the predicted imaging subscores of the NC subjects were significantly different between the training dataset "Beijing 750" ($n = 30$) and the testing dataset "Beijing HDxt" ($n=10$). We found that there was no significant difference between the two groups (two-sample T test, $p=0.24$). The distribution bar is shown as follows.



Second, we investigated the relationships between the fMRI signal-to-noise ratio (SNR) and the predicted imaging subscores. Different MRI acquisition protocols (e.g. scanner hardware, imaging protocols and acquisition sequences) can influence the imaging SNR. But, it is not trivial to estimate the SNR in resting-state fMRI, since the noise is complex and also differs spatially. Here, we calculated the temporal SNR (tSNR) as the ratio between the mean fMRI signal and its temporal standard deviation in each voxel (Welvaert and Rosseel, 2013), and then averaged across all voxels in each region of interest (ROI) (Gardumi *et al.*, 2016; Hay *et al.*, 2017). Since there were 22 ROIs in this study, the median of these 22 ROI tSNR values was used as the measure for evaluating the SNR of the fMRI. We then correlated the median tSNR with the predicted imaging subscores across all of the NC subjects (n=40), and found that there were significant correlations between them (Pearson's correlation $r=0.36$, $p=0.024$) as shown in the following figure.



From the above two experiments, we found that (1) the fMRI tSNR could be one of influencing factors in the application of the presented model; (2) the predicted imaging subscores for the NC subjects could be approximate across different sites when the tSNR was proximity. Therefore, we suggested that our presented model can be applied to different centers, although the calibration might be required.

Further, the tSNR in fMRI is not only associated with instrumental noise but also modulated by subject-related noise, such as physiological fluctuations and motion artifacts (Huettel et al., 2009). Therefore, we suggest that, on the one hand, the quality of imaging acquisition, including MRI scanner and imaging sequence/ parameters, need to be guarantee; on the other hand, scanning protocols is required to be standardized to reduce the subject-related noise during the scanning.

References:

- Gardumi A, Ivanov D, Hausfeld L, Valente G, Formisano E, Uludag K. The effect of spatial resolution on decoding accuracy in fMRI multivariate pattern analysis. *Neuroimage* 2016; 132: 32-42.
- Hay E, Ritter P, Lobaugh NJ, McIntosh AR. Multiregional integration in the brain during resting-state fMRI activity. *Plos Computational Biology* 2017; 13(3).
- Huettel SA, Song AW, McCarthy G. *Functional Magnetic Resonance Imaging*. 2 ed: Sinauer Associates; 2009.
- Welvaert M, Rosseel Y. On the Definition of Signal-To-Noise Ratio and Contrast-To-Noise Ratio for fMRI Data. *Plos One* 2013; 8(11).